

5-2007

# RAMAN SPECTROSCOPIC EVIDENCE FOR ANHARMONIC PHONON LIFETIMES AND BLUESHIFTS IN 1D STRUCTURES

Rahul Rao

Clemson University, rrao@clemson.edu

Follow this and additional works at: [https://tigerprints.clemson.edu/all\\_dissertations](https://tigerprints.clemson.edu/all_dissertations)

 Part of the [Condensed Matter Physics Commons](#)

---

## Recommended Citation

Rao, Rahul, "RAMAN SPECTROSCOPIC EVIDENCE FOR ANHARMONIC PHONON LIFETIMES AND BLUESHIFTS IN 1D STRUCTURES" (2007). *All Dissertations*. 73.

[https://tigerprints.clemson.edu/all\\_dissertations/73](https://tigerprints.clemson.edu/all_dissertations/73)

This Dissertation is brought to you for free and open access by the Dissertations at TigerPrints. It has been accepted for inclusion in All Dissertations by an authorized administrator of TigerPrints. For more information, please contact [kokeefe@clemson.edu](mailto:kokeefe@clemson.edu).

RAMAN SPECTROSCOPIC EVIDENCE FOR ANHARMONIC PHONON  
LIFETIMES AND BLUESHIFTS IN 1D STRUCTURES

---

A Dissertation  
Presented to  
the Graduate School of  
Clemson University

---

In Partial Fulfillment  
of the Requirements for the Degree  
Doctor of Philosophy  
Physics

---

by  
Rahul Rao  
May 2007

---

Accepted by:  
Dr. Apparao M. Rao, Committee Chair  
Dr. Terry M. Tritt  
Dr. Joseph Manson  
Dr. Dieter Hartmann

## ABSTRACT

Anharmonic effects in two different quasi-1D systems were probed via micro-Raman spectroscopy. In the first system, we observed *upshifts* of peaks in the Raman spectra for  $\beta$ -Ga<sub>2</sub>O<sub>3</sub> nanowires grown along the [110] growth direction compared those present in bulk  $\beta$ -Ga<sub>2</sub>O<sub>3</sub>. Contrary to our Raman studies on  $\beta$ -Ga<sub>2</sub>O<sub>3</sub> nanowires, *downshifts* in the Raman spectrum for  $\beta$ -Ga<sub>2</sub>O<sub>3</sub> nanowires grown along  $[40\bar{1}]$  direction has also been reported by other research groups. We attribute these Raman shifts to the growth direction-induced lattice strains (compressive and tensile) present in the nanowires, and present a model based on the quasi-harmonic density functional theory to support our hypothesis.

In the second study, the anharmonic phonon lifetime in suspended single-walled carbon nanotubes was measured using high-resolution micro-Raman spectroscopy. Previous studies on suspended nanotubes performed with scanning tunneling microscopy (STM) reported phonon lifetimes of the order of nanoseconds for the radial breathing mode (RBM). However, the longest phonon lifetimes measured from Raman spectroscopy is of the order of picoseconds. Our study also showed the RBM lifetime to be in the picosecond regime, and we sought to explain this discrepancy with the STM study by invoking an anharmonic model for phonon decay in carbon nanotubes.



## DEDICATION

To my wife, Laura, whose continuous love and support over the past few years has helped me immensely in reaching this important milestone.



## ACKNOWLEDGMENTS

I would like to thank my advisor, Dr. Apparao M. Rao for his endless support and guidance over the last couple of years. His confidence in me helped me get through a tough phase in my life and come out on top. I have learnt a lot from him and he continues to inspire me to do better in my work. Some of the work done in this thesis would not have been possible without the theoretical insights of Prof. José Menendez at ASU. I enjoyed my time at ASU in the summer of 2005, and exposure to working with another group helped me immensely. I would also like to thank Dr. Jianjun Dong and his students for agreeing to take on the theoretical work that became part of my thesis. Many thanks to my dissertation committee members Dr. Manson, Dr. Hartmann, and especially Dr. Tritt who encouraged me to join the Ph.D. program in physics.

I would like to thank my parents at home for supporting me through these years, and my good friends Aditya, Harish, and Sajay who have accompanied me on the long road to a doctoral degree, and whose friendship will be treasured. And finally, thanks to all the present and past Rao group members.





## TABLE OF CONTENTS

	Page
TITLE PAGE.....	i
ABSTRACT .....	iii
DEDICATION.....	iv
ACKNOWLEDGEMENTS .....	v
LIST OF TABLES.....	viii
LIST OF FIGURES .....	ix
 CHAPTER	
1. ANHARMONICITY IN MATERIALS.....	1
Introduction .....	1
Experimental observations of anharmonicity .....	5
 2. RAMAN SPECTROSCOPY .....	 13
Introduction .....	13
Quantum Theory of Raman Scattering.....	19
Selection Rules .....	25
Raman Instrumentation.....	26
Renishaw 1000 Raman Microscope .....	27
Triax 550 Raman Spectrometer .....	29
 3. BLUESHIFTED RAMAN SCATTERING IN GALLIUM OXIDE NANOWIRES .....	 32
Introduction .....	32
Nanowire Synthesis.....	34
Growth Mechanism.....	35
Electron Microscopy of $\beta$ -Ga <sub>2</sub> O <sub>3</sub> nanowires.....	37
Raman Modes of $\beta$ -Ga <sub>2</sub> O <sub>3</sub> .....	39
FTIR Spectroscopy .....	49
Raman Peak Shifts due to Quantum Confinement.....	51

## Table of Contents (Continued)

	Page
LDA Model of the Peak Frequencies of $\beta$ -Ga <sub>2</sub> O <sub>3</sub> .....	58
4. ANHARMONIC PHONON LIFETIMES IN CARBON NANOTUBES .....	68
Introduction .....	68
Raman Scattering in Carbon Nanotubes .....	71
Phonon Decay and Lifetime .....	75
Nanotube Synthesis.....	82
Electron Microscopy of Suspended SWNTs .....	84
Raman Spectroscopy of Suspended SWNTs .....	85
5. SUMMARY.....	105
Conclusions .....	105
Future Work.....	107
APPENDIX .....	111
REFERENCES .....	113

## LIST OF TABLES

Table	Page
1      Comparison of Calculated Raman Mode Frequencies With Those Measured in Bulk $\beta$ -Ga <sub>2</sub> O <sub>3</sub> .....	66
2      Estimated Internal Strains .....	67
3      Raman mode frequencies and frequency shifts in $\beta$ -Ga <sub>2</sub> O <sub>3</sub> nanowires with the $[40\bar{1}]$ and $[110]$ growth directions. Overall, excellent agreement between the observed and calculated shifts is seen for all mode frequencies except the two marked with an * .....	68



## LIST OF FIGURES

Figure	Page
1.1 Potential Energy versus Displacement Diagram for a Simple Harmonic Oscillator.....	2
1.2 Potential Energy versus Position Diagram for a Harmonic and Anharmonic Oscillator.....	5
1.3 This The calculated contribution of confinement (open circles) and anharmonic (solid circles) effects to the linewidth of the $E_g$ mode ( $143\text{ cm}^{-1}$ ) in $\text{TiO}_2$ nanoparticles at different temperatures.....	6
1.4 Figure 1.4: Experimental (dots) and calculated (lines) data showing the behavior of the Raman modes of $\text{TiO}_2$ with increasing uniaxial stress along the $a$ axis.....	7
1.5 Raman spectra of $\beta\text{-Ga}_2\text{O}_3$ nanorods (top trace) synthesized in a RF-induction furnace and $\beta\text{-Ga}_2\text{O}_3$ powder (bottom trace) .....	8
1.6 Raman spectra of $\beta\text{-Ga}_2\text{O}_3$ nanowires produced by arc-discharge and $\beta\text{-Ga}_2\text{O}_3$ powder .....	9
1.7 (a) Schematic diagram showing the set-up for performing spectroscopy on suspended SWNTs. A voltage is applied to the substrate with respect to the tip, and the current flowing from the substrate through the SWNT to the tip is measured. (b), STM image of a nanotube crossing a trench. Scale bar, 25 nm. The apparent width of the 2-nm-diameter tube is enlarged by tip convolution. (c), High-resolution image of the suspended portion of the SWNT showing atomic resolution. Scale bar, 2 nm.....	10
2.1 Rayleigh and Raman scattered light off a sample excited with the incident monochromatic light. ....	14
2.2 Energy diagram comparing Rayleigh, Stokes and anti-Stokes Raman scattering light. $\Delta E$ and $\Delta E'$ denote the incident and scattered photon energies respectively. ....	15

## List of Figures (Continued)

Figure	Page
2.3 Schematic layout of the Renishaw 1000 Raman microscope.....	27
2.4 Layout of Raman spectroscopy system used for analyzing anharmonic phonon lifetimes in suspended single-walled carbon nanotubes as described in Chapter 4.....	32
3.1 Schematic of the microwave plasma CVD reactor used to synthesize gallium oxide nanowires.....	35
3.2 Schematic for the growth process of gallium oxide nanowires .....	36
3.3 Raman spectrum of a gallium-coated substrate in which the entire gallium pool did not react with oxygen in a non-optimized experiment.....	38
3.4 SEM micrograph of $\beta$ -Ga <sub>2</sub> O <sub>3</sub> nanowires grown from a large molten gallium droplet using a microwave plasma mediated technique.....	39
3.5 High resolution TEM image of an individual 13 nm thick $\beta$ -Ga <sub>2</sub> O <sub>3</sub> nanowire .....	40
3.6 Representation of the tetrahedra and octahedra which form the structure of $\beta$ -Ga <sub>2</sub> O <sub>3</sub> .....	40
3.7 Unit cell of monoclinic $\beta$ -Ga <sub>2</sub> O <sub>3</sub> .....	41
3.8 Micro-Raman spectrum of bulk $\beta$ -Ga <sub>2</sub> O <sub>3</sub> .....	42
3.9 Cartesian displacements involved in the in-plane $A_g$ vibrational mode at 111 cm <sup>-1</sup> in $\beta$ -Ga <sub>2</sub> O <sub>3</sub> The gallium and oxygen atoms are shown by the black and red dots respectively.....	43
3.10 Micro-Raman spectra of $\beta$ -Ga <sub>2</sub> O <sub>3</sub> nanowires (top three traces) dispersed on quartz and silicon substrates collected at three different excitations showing peaks upshifted compared to bulk $\beta$ -Ga <sub>2</sub> O <sub>3</sub> (bottom trace).....	45
3.11 Raman spectrum of $\alpha$ -Ga <sub>2</sub> O <sub>3</sub> .....	46

## List of Figures (Continued)

Figure	Page
3.12 SEM image of the $[40\bar{1}]$ nanowires grown by RF-induction. The inset is a high resolution TEM image from one of the wires showing twinned planes.....	49
3.13 FTIR transmittance spectra of bulk (bottom trace) and $[110]$ $\beta$ -Ga <sub>2</sub> O <sub>3</sub> nanowires (top trace). ....	52
3.14 Raman spectra showing the evolution of the first-order 520 cm <sup>-1</sup> peak of four silicon nanowire samples.....	53
3.15 Phonon dispersion curves for silicon. Both experimental (points) and calculated (solid lines) data are shown.....	56
3.16 Calculated and experimental (inelastic x-ray scattering) phonon dispersion curves for graphite.....	57
3.17 Raman spectra excited using the 514 nm excitation line of an argon ion laser for crystalline graphite with differing number of graphene layers. ....	58
4.1 Calculated electron density of states for three different nanotubes. The van Hove singularity transitions are shown for both semiconducting (labeled S) and metallic nanotubes (labeled M).....	71
4.2 Simulation of the radial breathing mode vibrations of a 0.8 nm diameter single-walled nanotube. The vertical lines over each carbon atom indicate the radial motion of the atoms.....	74
4.3 Raman-active normal eigenvectors and frequencies for the tangential G band of a single-walled carbon nanotubes. The arrows indicate the direction of the carbon atom displacements in a unit cell for a (10,10) SWNT. A typical G band showing the G <sup>+</sup> and G <sup>-</sup> peaks is shown on the right .....	75
4.4 Experimental points and calculated curves showing the temperature dependence of the linewidth of the 167 cm <sup>-1</sup> band for a SWNT bundle. The band is simulated as consisting of four close-lying Lorentzian components with $\Gamma_0 = 0.5, 1.0, \text{ and } 1.5 \text{ cm}^{-1}$ .....	79

## List of Figures (Continued)

Figure	Page
4.5 Linewidth of the RBM ( $\Gamma_{\text{RBM}}$ ) vs nanotube diameter ( $d_t$ ) for 81 metallic (solid symbols) and 89 semiconducting (open symbols) isolated SWNTs .....	79
4.6 Individual single-walled nanotubes grown between pre-fabricated pillars on silicon substrates).....	81
4.7 Stokes and anti-Stokes Raman spectra from an individual suspended SWNT on a silicon substrate with $\omega_{\text{RBM}}$ at $237 \text{ cm}^{-1}$ .....	82
4.8 Schematic of the chemical vapor deposition method used to synthesize suspended SWNTs. ....	84
4.9 SEM image showing several suspended Swnts across the corners of a trench etched into the silicon substrate. The clusters appearing at the bottom of the trench are catalyst particles and do not interfere with the Raman spectra since they do not lie in the focal plane of the focus beam of the exciting laser. ....	85
4.10 Micro-Raman spectra from an individual suspended semiconducting SWNT (left) and a metallic SWNT (right). The peak position (linewidth) are indicated in the graphs. ....	88
4.11 Micro-Raman spectra in the RBM range from a region on a trench containing multiple suspended SWNTs.....	89
4.12 The tangential bands for a semiconducting (top) and a metallic (bottom) suspended SWNT .....	91
4.13 Kataura plot between nanotube diameter and incident laser excitation energy ( $E_L$ ) The vertical lines indicate the diameter distribution of the suspended SWNTs analyzed in the present study.....	92
4.14 Deconvoluted $2\Gamma$ (Lorentzian FWHM) values for several suspended SWNTs plotted versus $\omega_{\text{RBM}}$ . The circled data points represent metallic SWNTs while the rest are..... semiconducting SWNTs. Error bars from the linewidth fit are also plotted. ....	93



## List of Figures (Continued)

Figure	Page
4.15 The calculated phonon dispersion relations of a carbon nanotube (bottom), and the corresponding phonon density of states (top). .....	94
4.16 Raman spectra around the radial breathing mode frequency for two representative suspended SWNTs collected for different incident laser powers. From the lineshape of the tangential band present at $\sim 1590 \text{ cm}^{-1}$ the spectra in panels (a) and (b) are assigned to a metallic and semiconducting nanotubes, respectively. ....	95
4.17 Normalized linewidth versus incident total laser power $P$ (The normalized linewidth is defined as the Lorentzian FWHM at $P$ divided by the FWHM at $P_0 = 1 \text{ mW}$ ). The lines correspond to fits with eq. (4.16), in which the only adjustable parameter is the suspended length $L$ . ....	101
4.18 (a) Solid line: Raman phonon population decay under conditions that create a decay bottleneck ( $p \sim 2$ ); Dotted line: Raman phonon population decay under conditions in which the decay bottleneck is negligible ( $p \gg 1$ ). Dashed-dotted line: Raman phonon population decay when the secondary phonons are also created by the external perturbation like tunneling (b) Predicted Raman spectrum corresponding to the solid line in panel (a).; (c) Solid line: Modeled observed Raman spectrum obtained from convoluting the spectrum in panel (b) with a Gaussian function, Dotted line: Fit of the solid line using a Voigt profile.....	105



## CHAPTER ONE ANHARMONICITY IN MATERIALS

### Introduction

The simplest vibrational model in a crystal considers lattice vibrations as arising from the harmonic motion of atoms at each lattice site [1]. Vibrational interactions between the atoms give rise to waves within the solids, which have allowed wavelengths and amplitudes governed by the lattice structure in the solid. For small vibrations in one dimension about equilibrium, the potential energy  $U(x)$  of the  $\alpha$ 'th atom within the solid can be expanded as a Taylor series as follows:

$$U(x) = U_0 + \sum_{\alpha} U'_{\alpha} x_{\alpha} + \frac{1}{2} \sum_{\alpha} U''_{\alpha} x_{\alpha}^2 + O(x^3) + \dots \quad , \quad (1.1)$$

where the first, second, and the third term represent the zeroeth, first, and second order term respectively. Typically, to a good approximation this potential can be taken to be equal to the harmonic oscillator potential. This is the so called harmonic approximation in which the series for the potential energy is truncated at the second term. Now since each lattice site is occupied by atoms that are vibrating, these lattice sites are equivalent. Also, by symmetry, there is equal probability for motion along opposite directions. Hence the linear term in the potential expansion vanishes. The zeroeth (zero-point) term in the expansion only affects the scaling and can be duly ignored for most calculations. Thus, in the

classical picture, the potential energy of a simple harmonic oscillator contains only a term that is quadratic in displacement and can be stated as

$$U = \frac{1}{2}U_{\alpha}x_{\alpha}^2 = \frac{1}{2}m\omega^2x^2 \quad , \quad (1.2)$$

where  $m$  is the mass of the oscillator,  $\omega$  is the frequency, and  $x$  is the displacement in one direction of the oscillator. In the classical picture, the simple harmonic oscillator can be described physically with a ball and spring model, where  $m$  is the mass of the ball,  $x$  is the displacement of the ball in one direction, and  $k$  is the spring constant of the oscillator. Figure 1 shows potential energy of a harmonic oscillator plotted against position. Since the energy is proportional to the square of the displacement, it is parabolic in nature. The potential energy is symmetric about the origin at  $x = 0$ .

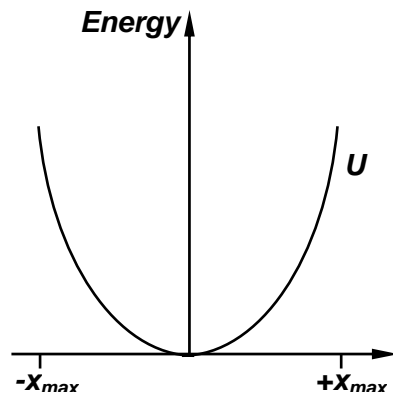


Figure 1.1: Potential energy versus displacement diagram for a simple harmonic oscillator.

While the classical “ball and spring” model can adequately explain harmonic motion between atoms, in order to get a complete description of atomic vibrational motion in a crystal lattice, one has to consider a quantum mechanical model. The energies of the quantum mechanical harmonic oscillator can be determined by the solution of Schrödinger’s equation, which is stated as

$$H|\psi\rangle = E|\psi\rangle \quad (1.3)$$

where  $H$  is the Hamiltonian of the system,  $|\psi\rangle$  is the wavefunction of the atom associated with the oscillator, and  $E$  is the energy of the quantum mechanical oscillator. The solution of the Schrödinger equation reveals that the energy levels of the oscillator are quantized and the energy of the  $n$ ’th level is given by

$$E_n = \left( n + \frac{1}{2} \right) \hbar \omega \quad (1.4)$$

The energy levels of the quantum harmonic oscillator are discrete. The harmonic potential energy can be used to approximately describe many processes in solids. In the case of vibrational motion of atoms within a solid, the harmonic potential can be used to calculate normal mode frequencies for phonons, where a phonon is a quantum of lattice vibration having energy equal to  $\hbar\omega$ . Thus with the harmonic potential, one can get a complete description of the normal vibrational modes of a crystal. However, there are drawbacks with the harmonic approximation. Certain

experimental observations cannot be adequately explained solely on the basis of harmonic potentials as listed below [2]-

1. Within the harmonic approximation, phonons do not interact with each other. This implies that vibrational waves, once created within the solid, would propagate infinitely and never decay.
2. A solid would not show thermal expansion.
3. Vibrational frequencies are independent of strain.

The above features can be explained in part by an anharmonic theory which takes account of the terms in the potential energy which are higher than the quadratic terms. In that case, the Hamiltonian of the oscillator can be split into the harmonic (quadratic) and anharmonic (cubic and higher terms) parts, and a quasi-harmonic treatment could then be applied to the oscillator. Within this framework, phonons within a solid are considered as traveling waves that can interact with each other. The anharmonic component of the oscillator potential causes an interchange of energy between these traveling waves, thus resulting in the decay of phonons, and hence finite phonon lifetimes. The inclusion of a third order term causes the energy of the anharmonic oscillator to deviate from the parabolic shape of the harmonic oscillator and looks like the oscillator energy shown in Fig. 1.2 below.

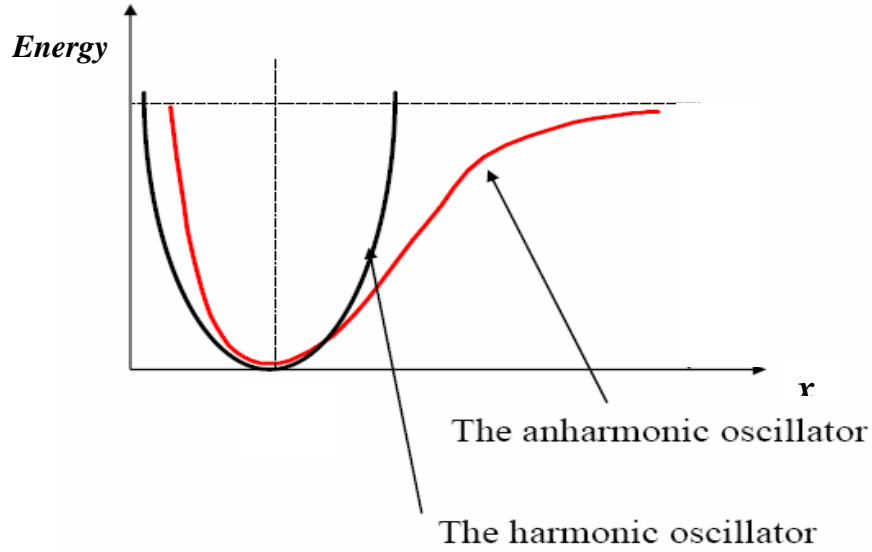


Figure 1.2: Potential energy versus position diagram for a harmonic and anharmonic oscillator.

#### Experimental observations of anharmonicity

Anharmonic effects in materials have been observed by a variety of methods. Shiren [3] described an experiment in which a beam of longitudinal phonons of frequency 9.2 GHz interact in a magnesium oxide crystal with a parallel beam of longitudinal phonons at 9.18 GHz. The interaction of these two beams produced a third beam of longitudinal phonons at  $9.2 + 9.18 = 18.38$  GHz[3]. Also, anharmonic interactions between phonons lead to phonon decay, and hence finite lifetimes. Phonon lifetimes have been observed in several materials through various spectroscopic methods such as inelastic x-ray scattering [4], Raman scattering [5] and neutron scattering [6].

The linewidth of a Raman mode is inversely proportional to its lifetime, and anharmonic linewidths (lifetimes) increase (decrease) with increase in

temperatures. For example, Šćepanović *et al.* [7] observed changes in the linewidth of the  $143\text{ cm}^{-1}$  mode in nanocrystalline  $\text{TiO}_2$  powder. Such changes are normally attributed to phonon confinement effects, but they show that the anharmonic contribution to the change in linewidth (phonon lifetime) with temperature is greater than that of confinement. Fig. 1.3 shows their calculated contributions due to anharmonicity and confinement, and while the confinement contribution does not change significantly with temperature, the anharmonic broadening of the  $143\text{ cm}^{-1}$  mode with increasing temperature is quite large. More details about phonon lifetimes and anharmonic broadening of Raman linewidths due to increasing temperature in carbon nanotubes are addressed in chapter 4.

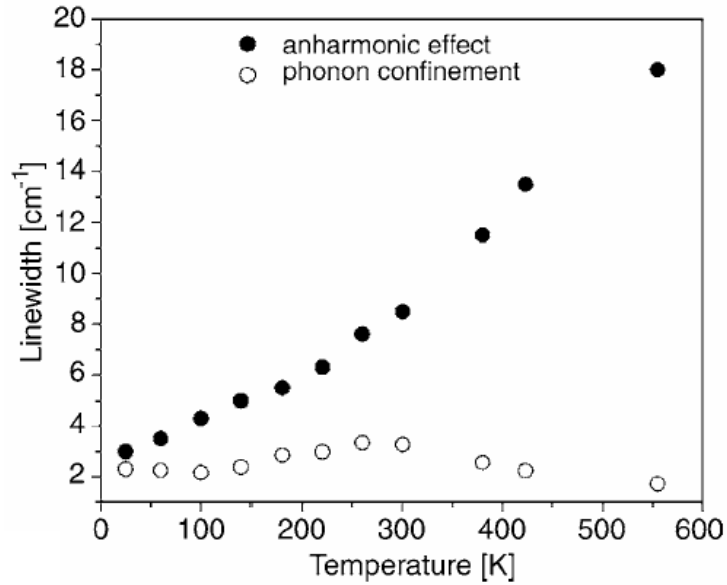


Figure 1.3: The calculated contribution of confinement (open circles) and anharmonic (solid circles) effects to the linewidth of the  $E_g$  mode ( $143\text{ cm}^{-1}$ ) in  $\text{TiO}_2$  nanoparticles at different temperatures [7].



As mentioned above, the harmonic approximation does not explain thermal lattice expansion or contraction. Similarly, changes in a lattice due to inherent strains induced during growth cannot be explained within the harmonic potential picture, and an anharmonic potential must be taken into account to fully explain the experimentally observed data. In such cases, Raman spectroscopy is a powerful tool since strains cause Raman peaks to move and broaden. The Raman spectra of samples under strain can be then modeled using anharmonic potentials. Peercy *et al.* [8] studied the uniaxial stress dependence in the Raman-active phonons in  $\text{TiO}_2$  using experiment as well as anharmonic theory. Fig. 1.4 shows the room temperature frequency shifts of 3 different Raman modes in  $\text{TiO}_2$  as a function of uniaxial pressure. A uniaxial stress along the  $a$  axis of  $\text{TiO}_2$  causes the  $A_{1g}$  and  $E_g$  mode to upshift due to compressive strain, while the  $B_{1g}$  mode downshifts due to tensile strain.

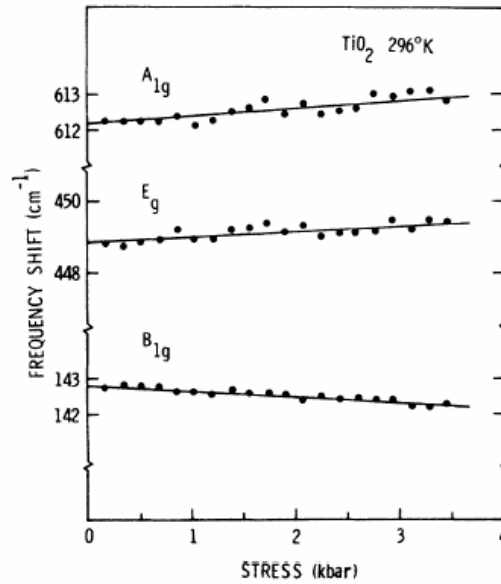


Figure 1.4: Experimental (dots) and calculated (lines) data showing the behavior of the Raman modes of  $\text{TiO}_2$  with increasing uniaxial stress along the  $a$  axis [8].

In this dissertation, we analyze the effect of compressive strains in gallium oxide nanowires via micro-Raman scattering. Gao *et al.* [9] synthesized  $\beta$ -Ga<sub>2</sub>O<sub>3</sub> nanowires having a  $[40\bar{1}]$  growth direction and the Raman mode frequencies of the  $[40\bar{1}]$  nanowires are red-shifted (shifted lower in energy) relative to corresponding frequencies in bulk  $\beta$ -Ga<sub>2</sub>O<sub>3</sub> by 4-23 cm<sup>-1</sup> (Fig. 1.5). On the other hand, Choi *et al.* [10] grew  $\beta$ -Ga<sub>2</sub>O<sub>3</sub> nanowires having a  $[001]$  direction and they saw no changes between the Raman spectra of their nanowires compared to that of bulk  $\beta$ -Ga<sub>2</sub>O<sub>3</sub> (Fig. 1.6).

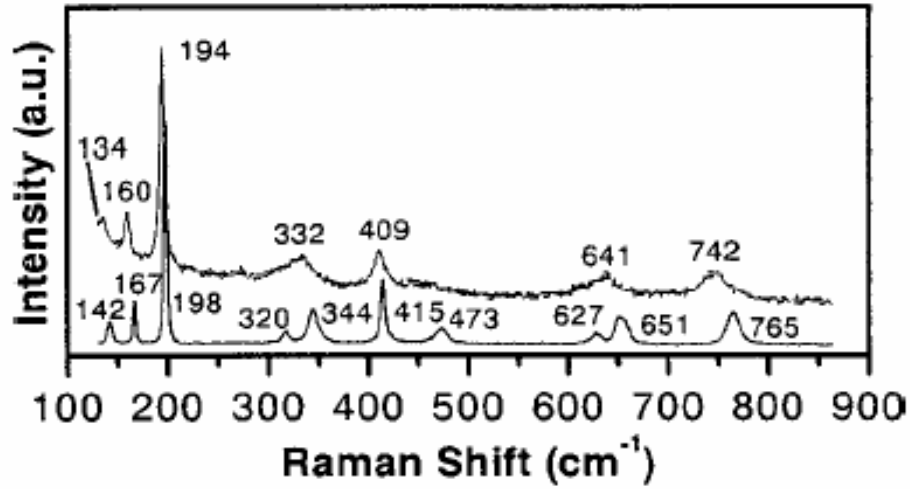


Figure 1.5: Raman spectra of  $\beta$ -Ga<sub>2</sub>O<sub>3</sub> nanorods (top trace) synthesized in a RF-induction furnace and  $\beta$ -Ga<sub>2</sub>O<sub>3</sub> powder (bottom trace) [9].

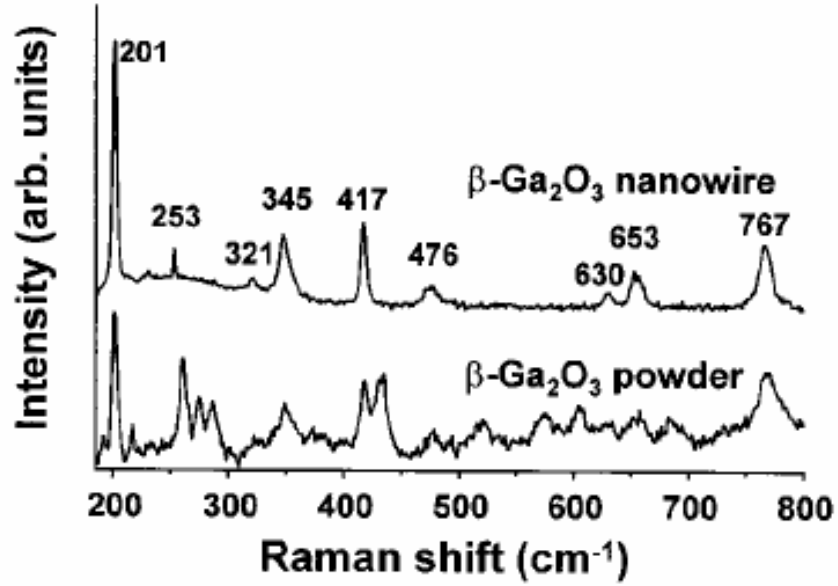


Figure 1.6: Raman spectra of  $\beta$ -Ga<sub>2</sub>O<sub>3</sub> nanowires produced by arc-discharge and  $\beta$ -Ga<sub>2</sub>O<sub>3</sub> powder [10].

Chapter 2 outlines the quantum mechanical description of the Raman effect and the experimental setup used in our lab to probe the vibrational properties nanomaterials described in this dissertation. Chapter 3 introduces the experimentally observed blueshift in the Raman mode frequencies of our strained gallium oxide nanowires. Both theory and experiment are used to evaluate the Raman peak upshifts and the theoretical framework is described which provides insight into the origin for this blueshift.

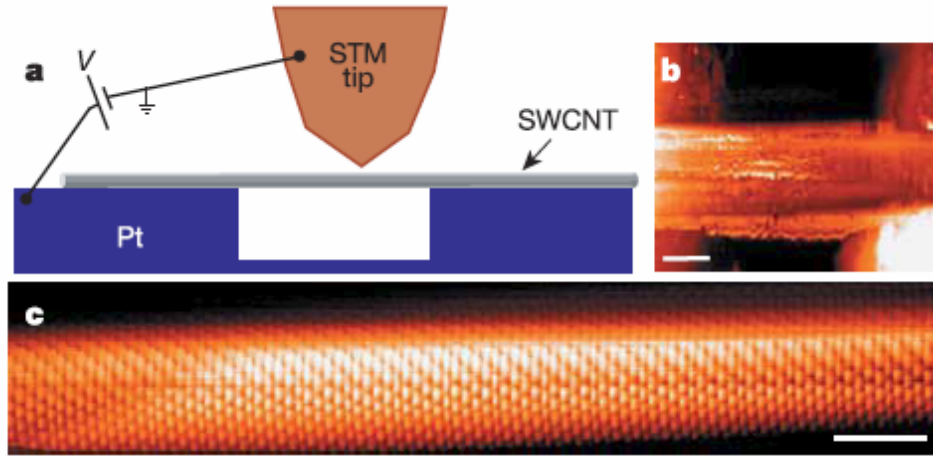


Figure 1.7: (a) Schematic diagram showing the set-up for performing spectroscopy on suspended SWNTs. A voltage is applied to the substrate with respect to the tip, and the current flowing from the substrate through the SWNT to the tip is measured. (b), STM image of a nanotube crossing a trench. Scale bar, 25 nm. The apparent width of the 2-nm-diameter tube is enlarged by tip convolution. (c), High-resolution image of the suspended portion of the SWNT showing atomic resolution. Scale bar, 2 nm [11].

In chapter 4, the analysis of anharmonic phonon lifetimes in suspended single-walled carbon nanotubes is presented. Recent scanning tunneling microscopy (STM) experiments show that electrons tunneling into a metallic single-walled carbon nanotube (SWNT) lead to a non-equilibrium phonon population for the radial breathing mode (RBM). LeRoy *et al.* [11] injected electrons into a suspended single-walled carbon nanotube through an STM tip (at 5K) that was brought into close contact with the nanotube (Fig. 1.7). They found that the injection of a large number of electrons into the nanotube causes a build-up of non-equilibrium phonons. By measuring the differential conductance of the injected electrons with varying sample voltage, they found that small peaks

appear at  $\sim 25$  meV, which are caused due to phonon-assisted tunneling. Interestingly, the energy of 25 meV is similar to the energy of the radial breathing mode phonon. Thus they were able to excite the RBM by injecting electrons into a SWNT. Furthermore, they analyzed various semiconducting and metallic nanotubes, and found an inverse relationship between the energy of the phonon-assisted tunneling peak and the nanotube diameter. By measuring the rate of electrons tunneling into the nanotube, they were able to estimate the anharmonic lifetime of the RBM to be  $\tau \approx 10$  ns. This corresponds to a Raman linewidth of  $5 \times 10^{-4} \text{ cm}^{-1}$ . To the best of our knowledge, the smallest Raman linewidth that has been experimentally measured (at a *low* temperature  $\sim 20$  K) for the RBM of the inner tube in a double-walled carbon nanotube is  $0.4 \text{ cm}^{-1}$  [12]. In this dissertation, a study on the linewidth measurements in suspended SWNTs is presented in chapter 4. In our study the Raman linewidths are lower than previously measured in isolated SWNTs, and a model is discussed to explain the discrepancy in the linewidth values measured through optical and tunneling experiments. Finally, at the end of this dissertation, a glossary of abbreviated terms used throughout the manuscript has been compiled in the appendix.



## CHAPTER TWO RAMAN SPECTROSCOPY

### Introduction

Raman spectroscopy is based upon the Raman effect, which may be described as the inelastic scattering of light from a gas, liquid or solid. Typically, the sample is excited with a monochromatic light source (for, e.g., a laser) and the Raman spectrum is detected as the scattered light intensity found at energies below and above the excitation energy. Discovered by the Indian physicist C. V. Raman in 1928 [13], it has also been called the Smekal-Raman effect [14], the former investigator having made some earlier theoretical predictions about it.

Raman spectroscopy is based on the interaction of light with molecules in some medium. When light hits a molecule it scatters off the molecule as Rayleigh scattering or as Raman scattering (Fig. 2.1). The radiation excites the molecule, distorting the shape of the molecule's electron cloud. When the electron cloud returns to its original shape, the energy in the molecule may have increased or decreased slightly, changing the energy of the scattered Raman radiation. Viewed in terms of energy levels, the electrons reside in the ground vibrational and electronic states before excitation. The monochromatic laser source excites the electrons to a virtual state, equal to the energy of the laser. When the electrons relax back to the ground electronic state, most go back to the ground vibrational state, giving back the same energy. This is Rayleigh (elastic) scattering. The small portion that relaxes back to an upper or lower vibrational state is the

Raman scattered light and is about 5 - 7 orders of magnitude less intense than Rayleigh scattered light [15].

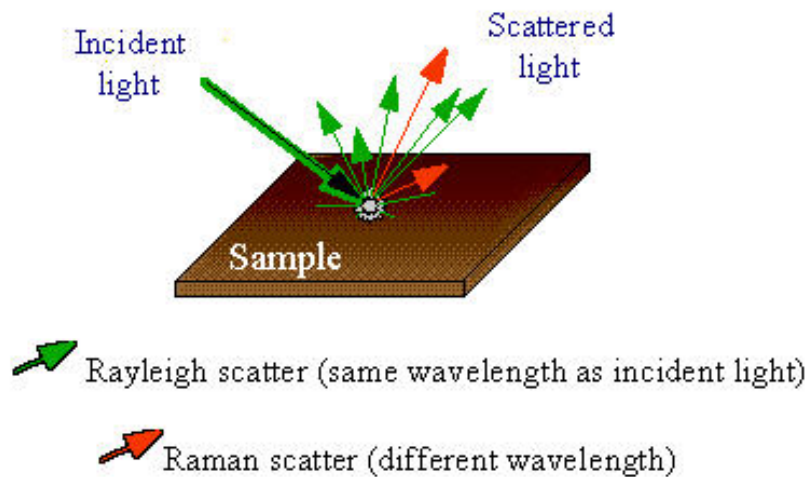


Figure 2.1 – Rayleigh and Raman scattered light off a sample excited with the incident monochromatic light.

The Raman scattered light that is adjusted up in wavelength is called the Stokes Raman scattering and that light which is adjusted down in wavelength is called the anti-Stokes Raman scattering (Fig. 2.2). Stokes Raman scattering occurs when some energy is absorbed from the photon of incident light into the molecule's rotational and vibrational energy and consequently a new photon of light with less energy is released. Anti-Stokes scattering occurs when the new photon formed gains energy compared to the incident photon via the absorption of energy from a previously excited molecule. Since the probability for an electron to be in an excited state before the scattering process is not high, the cross-section



for anti-Stokes scattering is much less than that of Stokes scattering and, consequently, the intensity of anti-Stokes scattered light is also much lower.

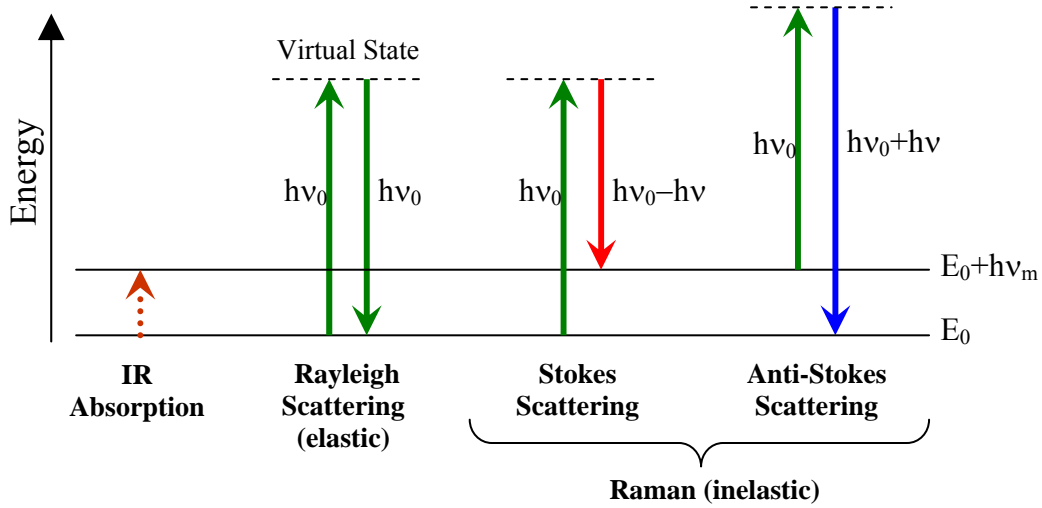


Figure 2.2 - Energy diagram comparing Rayleigh, Stokes and anti-Stokes Raman scattering light.  $\Delta E$  and  $\Delta E'$  denote the incident and scattered photon energies respectively.

A theoretical treatment of Raman scattering is essential for the understanding, interpretation and appreciation of the experimental Raman spectra from nanotube samples which will be presented later. In this section a general theory of Raman scattering is presented without any reference to the specific properties of the sample. By considering the general theory we gain insight into what information the Raman spectrum carries about the sample. The relevant properties of gallium oxide and carbon nanotubes are presented in chapters 3 and 4 respectively.

Raman scattering can be described theoretically using classical as well as quantum mechanical physics. In the classical description, when light strikes a molecule, it causes an induced electric dipole in the molecule. The electric dipole moment is related to the electric field of the incoming radiation through the polarizability of the molecule. The polarizability is a tensor which in general is a function of the interatomic distances, and will therefore change if the molecule is vibrating. If we expand the polarizability as a Taylor series, we can see that the light scattering causes the vibrating molecule to emit light having frequencies above and below the frequency of the incoming light. The polarizability,  $\alpha_{ij}$  can be expressed as

$$\alpha_{ij} = (\alpha_{ij})_0 + \sum_k \left( \frac{\partial \alpha_{ij}}{\partial q_k} \right)_0 q_k + \frac{1}{2} \sum_{k,l} \left( \frac{\partial^2 \alpha_{ij}}{\partial q_k \partial q_l} \right)_0 q_k q_l + \dots, \quad (2.1)$$

where the position-dependent polarizability  $\alpha_{ij}$  has been expanded as a function of the generalized coordinates  $q_k$  and  $q_l$ . The first two terms in the above equation can be grouped together and written as

$$\alpha_k = \alpha_0 + \alpha'_k q_k \quad (2.2)$$

Assuming that the molecules are undergoing simple harmonic motion, the generalized position coordinate of the  $k$ 'th molecule can be written as

$$q_k = q_{k0} \cos(\omega_k t + \delta_k) \quad (2.3)$$

Combining eqs. (2.3) and (2.2), we get

$$\alpha_k = \alpha_0 + \alpha'_k q_{k0} \cos(\omega_k t + \delta_k) \quad (2.4)$$

The polarizability is related to the molecules electric dipole moment and the electric field intensity of the incident radiation as

$$P^{(1)} = \alpha_k \cdot E, \text{ with } E = E_0 \cos \omega_0 t, \quad (2.5)$$

where the  $\omega_0$  is the frequency of the incident radiation. Thus the dipole moment can be written as

$$P^{(1)} = \alpha_k \cdot E_0 \cos \omega_0 t \quad (2.6)$$

From eqs. (2.6) and (2.4), we get

$$P^{(1)} = \alpha_0 \cdot E_0 \cos \omega_0 t + \alpha'_k \cdot E_0 q_{k0} \cos \omega_0 t \cos(\omega_k t + \delta_k) \quad (2.7)$$

Eq. (2.7) can be simplified by making use of the trigonometric identity

$$\cos A \cos B = \frac{1}{2} \{ \cos(A+B) + \cos(A-B) \} \quad (2.8)$$

This results in the following expression for the polarizability:

$$P^{(1)} = P^{(1)}(\omega_0) + P^{(1)}(\omega_0 - \omega_k) + P^{(1)}(\omega_0 + \omega_k), \quad (2.9)$$

where

$$\begin{aligned} P^{(1)}(\omega_0) &= \alpha_0 \cdot E_0 \cos \omega_0 t \\ P^{(1)}(\omega_0 - \omega_k) &= \frac{1}{2} q_{k0} \alpha'_k \cdot E_0 \{ \cos(\omega_0 - \omega_k)t - \delta_k \} \\ P^{(1)}(\omega_0 + \omega_k) &= \frac{1}{2} q_{k0} \alpha'_k \cdot E_0 \{ \cos(\omega_0 + \omega_k)t + \delta_k \} \end{aligned}$$

The first term in the above expression corresponds to the electric dipole of the moment after elastic light scattering of the incident radiation from the  $k$ 'th molecule of the sample, i.e., the first term corresponds to the Rayleigh scattered light. The second and third terms in eq. (2.9) correspond to Stokes and anti-Stokes scattered light respectively, as shown in Fig. 2.2. The classical description of Raman scattering, while giving insights into the nature of light scattering by a molecule, does not provide information about the coupling mechanisms between the light and the vibrations. To gain further insight, we need to consider a quantum mechanical treatment of Raman scattering, which is described in the next section.

## Quantum Theory of Raman Scattering

As mentioned above, the scattering of radiation causes a change in the polarizability of the molecule. According to quantum theory, radiation is emitted or absorbed as a result of a system making a downward or upward transition between two discrete energy levels. This concept can be extended towards both Rayleigh and Raman scattering from molecules by considering the radiation classically and regarding it as a source of perturbation of a molecular system which is treated quantum mechanically. Hence transitions between energy levels of the molecule take place with the emission or absorption of radiation, provided the transition moment associated with the initial and final states is non-zero. Consider that a system interacts with radiation of frequency  $\omega_0$  causing a transition from an initial state  $i$  to a final state  $f$ . The Hamiltonian for such a perturbation can be approximated by an electric dipole term. A much more detailed analysis, which is not presented here, can be performed by including the magnetic dipole and electric quadrupole terms with the perturbation Hamiltonian [15].

For the unperturbed system in the state  $i$  the time-dependent wavefunction  $\psi_i^0$  is given by

$$\psi_i^{(0)} = \psi_i \exp(-i\omega_i t), \quad (2.10)$$

where  $\psi_i$  is the corresponding time-independent wavefunction and  $\hbar\omega_i$  is the energy of the state  $i$ . When the system is perturbed, the time-dependent wavefunction  $\psi'_i$  is expressed as

$$\psi'_i = \psi_i^{(0)} + \psi_i^{(1)} + \psi_i^{(2)} + \dots, \quad (2.11)$$

where the second and third term in the above expression represent the first-order and second-order perturbation term. The electric dipole transition moment for the transition from state  $i$  to  $f$  can be written down using the Dirac notation as

$$[P]_{fi} = \langle \psi'_f | P | \psi'_i \rangle \quad (2.12)$$

$P$  is the electric dipole moment operator for the system defined by

$$P = \sum_j e_j r_j. \quad (2.13)$$

Just like the expansion for the wavefunction above, the dipole transition moments can be expanded as

$$[P]_{fi} = [P^{(0)}]_{fi} + [P^{(1)}]_{fi} + [P^{(2)}]_{fi} + \dots \quad (2.14)$$

where

$$\begin{aligned} [P^{(0)}]_{fi} &= \langle \psi^{(0)}_f | P | \psi^{(0)}_i \rangle \\ [P^{(1)}]_{fi} &= \langle \psi^{(1)}_f | P | \psi^{(0)}_i \rangle + \langle \psi^{(0)}_f | P | \psi^{(1)}_i \rangle \\ [P^{(2)}]_{fi} &= \langle \psi^{(1)}_f | P | \psi^{(1)}_i \rangle + \langle \psi^{(2)}_f | P | \psi^{(0)}_i \rangle + \langle \psi^{(0)}_f | P | \psi^{(2)}_i \rangle \end{aligned} \quad (2.15)$$

The transition moment  $[P^{(0)}]_{fi}$  relates to a direct transition between the unperturbed states  $f$  and  $i$ . The first-order term includes terms that are related to

normal Rayleigh and Raman scattering, while the second-order term contains terms that are relating to hyper Rayleigh and Raman scattering, and so on.

According to time-dependent perturbation theory

$$\psi_i^{(1)} = \sum_r a_{ir} \psi_r^{(0)} \quad \text{and} \quad \psi_f^{(1)} = \sum_r a_{fr} \psi_r^{(0)}, \quad (2.16)$$

where the summation is over all states  $r$  of the system except for  $i$  or  $f$ . If the system is initially in the state  $\psi_i^{(0)}$  then the coefficients  $a_{ir}$  are obtained by integrating

$$\frac{d}{dt} a_{ir} = \dot{a}_{ir} = -\frac{i}{\hbar} \langle \psi^{(0)}_r | H' | \psi^{(0)}_i \rangle, \quad (2.17)$$

where  $H'$  is the perturbation Hamiltonian. The time dependence of the electric field intensity in a non-polarized general form can be written as

$$E = \tilde{E}_0 \exp(-i\omega_0 t) + \tilde{E}_0^* \exp(i\omega_0 t). \quad (2.18)$$

Assuming that the electric field of the incoming radiation does not vary across the surface of the molecule, the perturbation Hamiltonian  $H'$  can be considered to contain only an electric dipole term and can be written as

$$H' = -P \cdot E. \quad (2.19)$$

Thus the coefficients from eq. (2.8) can be written as

$$a_{ir} = \frac{1}{\hbar} [P]_{ri} \cdot \left[ \frac{\tilde{E}_0^* \exp\{i(\omega_{ri} + \omega_0)t\}}{\omega_{ri} + \omega_0} + \frac{\tilde{E}_0 \exp\{i(\omega_{ri} - \omega_0)t\}}{\omega_{ri} - \omega_0} \right] \quad (2.20)$$

and

$$a_{fr}^* = \frac{1}{\hbar} [P]_{fr} \cdot \left[ \frac{\tilde{E}_0 \exp\{-i(\omega_{rf} + \omega_0)t\}}{\omega_{rf} + \omega_0} + \frac{\tilde{E}_0^* \exp\{-i(\omega_{rf} - \omega_0)t\}}{\omega_{rf} - \omega_0} \right] \quad (2.21)$$

where

$$\begin{aligned} \omega_{ri} &= \omega_r - \omega_i & etc. \\ [P]_{ri} &= \langle \psi_r | P | \psi_i \rangle & etc. \end{aligned} \quad (2.22)$$

The first-order transition moment can now be evaluated by introducing eq. (11),

(15), and (16) into eq. (10). It is given by

$$\begin{aligned} [P^{(1)}]_{fi} &= \frac{1}{\hbar} \sum_r \left[ \frac{([P]_{fr} \cdot \tilde{E}_0)[P]_{ri}}{\omega_{rf} + \omega_0} + \frac{[P]_{fr}([P]_{ri} \cdot \tilde{E}_0)}{\omega_{rf} - \omega_0} \right] \exp\{-i(\omega_0 - \omega_{fi})t\} \\ &\quad \oplus \frac{1}{\hbar} \sum_r \left[ \frac{([P]_{fr} \cdot \tilde{E}_0^*)[P]_{ri}}{\omega_{rf} - \omega_0} + \frac{[P]_{fr}([P]_{ri} \cdot \tilde{E}_0^*)}{\omega_{rf} + \omega_0} \right] \exp\{-i(\omega_0 + \omega_{fi})t\} \end{aligned} \quad (2.23)$$



The two time-dependent transition moments in the equation above are complex. However, the radiation associated with a complex transition moment of the form  $P_{ml}\exp(-i\omega_{lm}t)$  corresponds to that from the real transition moment

$$P_{ml} \exp\{-i\omega_{lm}t\} + P_{ml}^* \exp\{i\omega_{lm}t\}, \quad (2.24)$$

provided this condition,  $\omega_{lm} > 0$  is satisfied. Thus the first term in eq. (18) will have a corresponding real transition moment if

$$\omega_0 - \omega_{fi} > 0 \quad (2.25)$$

If  $\omega_{fi}$  is negative, i.e., the final state is lower in energy than the initial state, this condition is always satisfied, and this transition is associated with Stokes scattering. Similarly, the condition is also satisfied if  $\omega_{fi}$  is zero, which means that the initial and final states have the same energy, and this corresponds to elastically scattered, or Rayleigh scattered radiation. If  $\omega_{fi}$  is positive, i.e., the final state is higher in energy than the initial state, then it is necessary for the energy of the incident quantum to be enough so that it reaches the final state. In the case of visible and ultraviolet electromagnetic radiation, this condition is always satisfied and this case corresponds to anti-Stokes scattering. The second term in eq. (18) will have a corresponding transition moment if

$$-\omega_0 - \omega_{fi} > 0 \quad (2.26)$$

i.e. if

$$\omega_i - \omega_f > \omega_0 \quad (2.27)$$

This condition implies that the energy of the initial state must exceed the energy of the final state by an amount that is greater than  $\omega_0$ . Thus, if  $\omega_0$  lies in the visible region of the spectrum, the initial state must be in an excited electronic state. The discussion of this term will not be presented here.

The transition moment amplitude presented in eq. 18 can be simplified by considering its real part and after some rearrangement and mathematical expansions, the  $x$  components of the transition moment amplitudes can be related to the complex electric field amplitudes as follows

$$[P^{(1)}_{x0}]_{fi} = \sum_y [\alpha^{(1)}_{xy}]_{fi} E_{y0} \quad \text{and} \quad [P^{(1)*}_{x0}]_{fi} = \sum_y [\alpha^{(1)*}_{xy}]_{fi} E^*_{y0} \quad (2.28)$$

where

$$[\alpha_{xy}]_{fi} = \frac{1}{\hbar} \sum_r \left[ \frac{[P_y]_{fr} [P_x]_{ri}}{\omega_{rf} + \omega_0} + \frac{[P_x]_{fr} [P_y]_{ri}}{\omega_{rf} - \omega_0} \right] \quad (2.29)$$

and

$$[\alpha^*_{xy}]_{fi} = \frac{1}{\hbar} \sum_r \left[ \frac{[P_x]_{fr} [P_y]_{ri}}{\omega_{rf} + \omega_0} + \frac{[P_y]_{fr} [P_x]_{ri}}{\omega_{rf} - \omega_0} \right] \quad (2.30)$$

Similar equations could be written for Rayleigh scattered light. The above expressions display the tensor relationship between the electric field and the transition moment. Evaluation of the transition polarizability tensor is of great importance in Raman scattering.

### Selection Rules

In the classical picture, the incoming radiation interacts with a molecule and induces a dipole moment. This induced dipole moment associated with a particular molecular frequency  $\omega_k$  will be zero unless at least one of the components of the derived polarizability tensor,  $(\alpha'_{ij})_k$  is non-zero. The derived polarizability tensor can be written as

$$(\alpha'_{ij}) = \left( \frac{\partial \alpha'_{ij}}{\partial Q_k} \right)_o \quad (2.31)$$

where the derivative is taken with respect to a generalized coordinate of vibration  $Q_k$  at the equilibrium position. Thus the condition for Raman scattering is that, for at least one component of the polarizability tensor, a plot of that component must have a non-zero gradient at the equilibrium position. In principle, this is enough to determine the selection rule for simple molecules. However, as molecular complexity increases, the classical picture becomes quite cumbersome to apply.

A much easier way to determine selection rules is to apply quantum mechanics to the system. In that case one needs to consider the properties of the vibrational transition polarizability components, rather than the derivative of the

polarizability tensor. For a particular transition to be Raman active, at least one of the six tensor components of the type  $[\alpha_{xy}]_{fi}$  ( $f$  and  $i$  are the final and initial quantum numbers, respectively) must be non-zero.

### Raman Instrumentation

Ever since the advent of the laser in the earlier part of the 20th century, analytical spectroscopy methods have become widespread tool for materials characterization tools. In particular, Raman spectroscopy has become one of the more popular characterization methods due to its relative ease of use and lack of complicated instrumentation. In addition, Raman spectroscopy is not affected by the biggest challenge that faces (Fourier transform infrared) FTIR spectroscopy – the need to eliminate water vapor. Raman spectra can be collected from liquid samples with ease. With the advent of nanotechnology over the past two decades, Raman spectroscopy has emerged as the “characterization tool” of choice to probe the confinement properties of nanostructured materials. The traditional Raman spectrometer is now being replaced by micro-Raman spectroscopy (Raman spectroscopy with an attached microscope) for finer spatial resolution of samples under study. The next section describes the micro-Raman spectroscopy setup used in our lab. Two different spectrometers were used for gathering the Raman data presented in this dissertation. The instrument used for the Raman analysis described in Chapter 3 was a Renishaw 1000 Raman microscope, while the Raman analysis of suspended single-walled carbon nanotubes described in

Chapter 4 was performed using a Triax 550 Spectrometer equipped with a Leica DM/LM light microscope.

### Renishaw 1000 Raman microscope

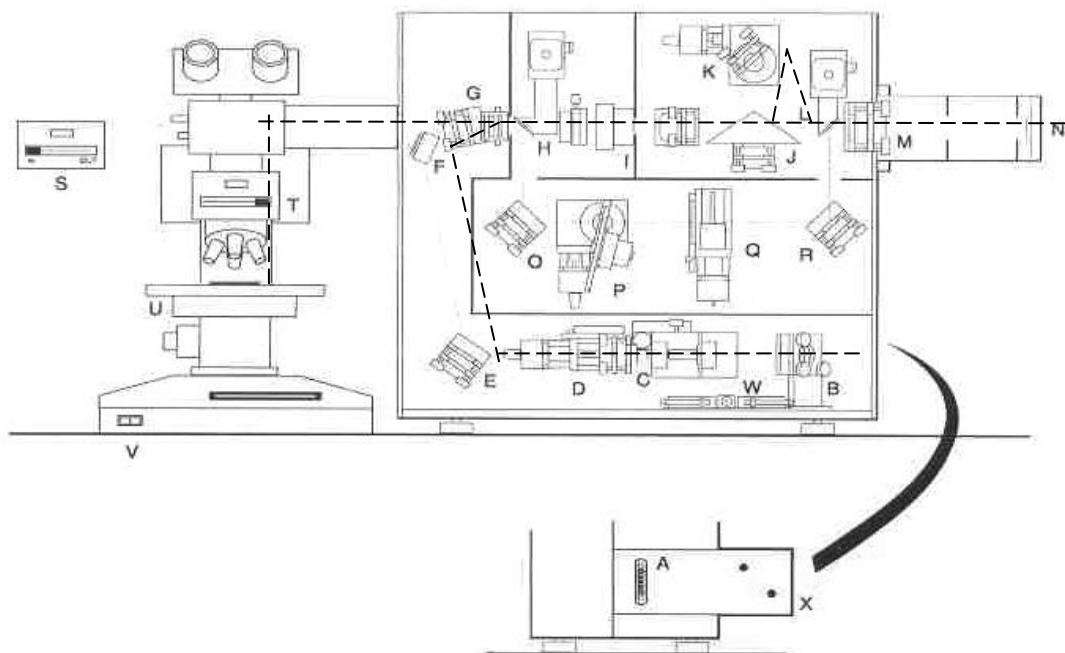


Figure 2.3: Schematic layout of the Renishaw 1000 Raman microscope.

Figure 2.3 shows a schematic of the Renishaw 1000 Raman microscope. To describe the whole setup briefly, monochromatic radiation from a 26 mW solid state laser (not shown in figure 2.3) with excitation wavelength 785 nm is made to pass through a series of optical elements (labeled B, W, C, D, E, F in Fig. 2.3) to the a holographic notch filter/beam splitter (G) which is used to redirect the beam into the microscope and on the sample, and which also collects

the scattered radiation and passes it on through a slit (I) to the diffraction grating (J, K) and finally on to the CCD (M, N). The light path is indicated by the dashed line in figure 3 above. A more detailed explanation is given below.

A 785 nm diode laser with a maximum power output of 26 mW is used as the excitation source. Between the laser and the spectrometer, a combination of lenses and a beam expander (W, C, D) are placed to refine the monochromatic laser light. This light hits a 45° (E) mirror which redirects the beam to the holographic notch filter (G). Polarizers can be placed along the light path to polarize the laser light in a specific direction. The Raman microscope has a polarizer that can be placed in the beam path

One of the most important parts of the excitation optics is a holographic notch filter. Since the Rayleigh scattered light comprises the maximum part of the scattered light off the sample, this has to be eliminated in order to efficiently detect the Raman scattered light. One or more holographic notch filters made of special polymer films are placed between the sample and the spectrometer to block out the Rayleigh scattered light. The efficiency of a notch filter determines the ability of the spectrometer to resolve peaks close to  $0\text{ cm}^{-1}$ , or in other words, the ability to measure vibrational modes that are close in energy to the laser excitation energy. The notch filter assembly in the Raman microscope also includes a polarizer/waveplate. This allows for the collected scattered radiation to be polarized. Thus in the case of fibers, the laser light can be polarized either perpendicular or parallel to the fiber axis during excitation and collection, giving 3 possible polarization configurations. If the perpendicular and parallel directions

to the fiber axis are chosen arbitrarily as X and Z, then the three configurations are XX, XZ (=ZX) and ZZ.

Scattered light from the sample is collected through the notch filter and passed through a slit to a prismatic diffraction grating (J). The grating basically takes the light coming through the slit and breaks it up into its respective wavelength components. This light is then passed on to a CCD (charge couple device) detector, which is basically a two dimensional panel array, like a video detector. The CCD converts the spectral information into pixel form for viewing on a computer or a TV screen. CCDs used with Raman systems typically have 256 x 1024 pixels, and are generally more preferred over the older photo-multiplier tubes due to their balance of quick collection time and good resolution.

In addition to the above mentioned components, accompanying the spectrometer is a fully functional Leica DM/LM metallurgical reflected light microscope with 5x, 20x, 50x, and 100x magnification capabilities.

#### Triax 550 spectrometer system

The layout of the Raman system used for the second set of Raman experiments described in Chapter 4 is shown in Fig. 2.4. The excitation sources consist of two lasers – a krypton ion laser with a output wavelength of 647.1 nm, and a argon ion laser with an output that can be tuned to either 514.5 nm or 488 nm. Both lasers are water-cooled continuous wave lasers that operate in TEM<sub>00</sub> mode. Typically, the output of a laser is a Gaussian distribution of wavelengths with a peak at one particular value. For efficient data collection, in addition to the

notch filter described above, the incoming laser beam can also be tuned as described below. Similar to the Renishaw Raman spectrometer, the laser beam passes through beam steering optics to the sample, where the backscattered Raman light is collected and sent to the spectrometer. The first component of the beam steering optics is a plasma filter, as shown in the upper left corner of Fig. 2.4. The plasma filter disperses the laser light vertically, and only wavelengths close to the center wavelength can be chosen by eliminating higher and lower wavelengths. This can be achieved through irises and band-pass filters. The laser beam that exits the plasma filter is diverted into a microscope using mirrors and a beamsplitter. The microscope used in this setup is the same as the one described above, with 5x, 20x and 50x magnification objective lenses. The backscattered light from the microscope is collected by the Raman spectrometer and after passing through a holographic notch filter, it can be focused at the entrance slit of the spectrometer. Between the focusing lens and the notch filter, one could make use of irises for stray-light rejection.

In addition to the Raman microscope, our Raman system also has a macro-sample measuring capability, as indicated by the dashed and dotted beam path in Fig. 2.4. For macro-Raman, the beam is incident on the sample at an angle of  $45^\circ$  and focused into a stripe ( $\sim 2\text{mm}$  tall and  $0.1\text{ mm}$  in width). The stripe focus allows us to maximize the Raman scattered signal from the large samples since the stripe fills the vertical entrance slit of the TRIAX uniformly. All spectra measured in the present study were, however, collected using the microscope.



The TRIAX 550 spectrometer is a single grating spectrometer that contains 3 gratings on a rotating turret. Each grating has a holographically ruled surface and groove density of 600, 1200, 2400 grooves/mm. Higher groove density gratings provide higher resolution due to more efficient light dispersion. However, the higher resolution comes at a cost of reduced intensity. For the Raman study on suspended carbon nanotubes, the 2400 groove/mm grating was used, and the samples were excited with the 647.1 nm wavelength krypton ion laser.

Inside the spectrometer, the Raman scattered light is directed to the grating by a mirror. The grating rotates through the chosen wavelength range and disperses the light, which is collected by a large focusing mirror and sent to the detector. The detector is a liquid nitrogen-cooled CCD, which offers increased sensitivity compared to the air-cooled CCD described in the previous section.

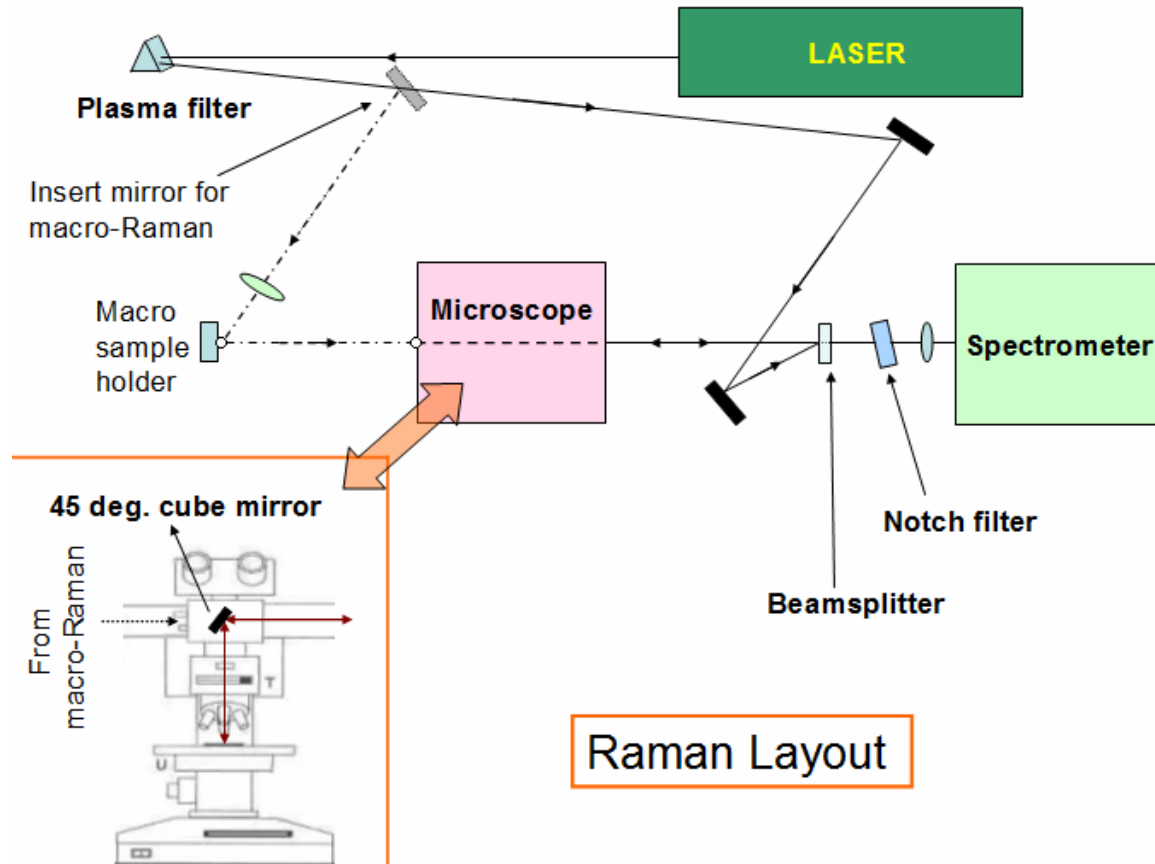


Figure 2.4: Layout of Raman spectroscopy system used for analyzing anharmonic phonon lifetimes in suspended single-walled carbon nanotubes as described in Chapter 4.

## CHAPTER THREE

### BLUESHIFTED RAMAN SCATTERING IN GALLIUM OXIDE NANOWIRES

#### Introduction

Bulk gallium oxide is a wide band-gap ( $E_g \sim 4.8$  eV) material that is of interest for its gas sensing [16, 17], catalytic [18] and optoelectronic device [19] applications. One-dimensional nanostructured forms of gallium oxide such as nanotubes, nanobelts and nanowires, have attracted recent interest due to enhanced optical properties [20, 21]. Gallium oxide nanowires have been synthesized by several methods such as physical evaporation [22, 23], arc discharge [10], RF induction [9], and catalyst assisted methods [24]. Recently, Sharma *et al.* [25] developed a novel technique for the synthesis of  $\beta$ -gallium oxide ( $\beta$ -Ga<sub>2</sub>O<sub>3</sub>) nanowires, nanotubes, and nanopaintbrushes based on the low miscibility of gallium oxide in molten gallium. In their method, gallium droplets and thin films serve as the solvent for nucleation and growth of the  $\beta$ -Ga<sub>2</sub>O<sub>3</sub> nanostructures. Their nanowires grow along the [110] direction. In comparison with the literature on  $\beta$ -Ga<sub>2</sub>O<sub>3</sub> nanowires, one finds that other growth methods yield  $\beta$ -Ga<sub>2</sub>O<sub>3</sub> nanowires with different growth directions. Using the gallium-droplet method,  $\beta$ -Ga<sub>2</sub>O<sub>3</sub> nanowires having a [321] growth direction have been synthesized using a thermal chemical vapor deposition (CVD) method [26]. Choi *et al.* [10] synthesized  $\beta$ -Ga<sub>2</sub>O<sub>3</sub> nanowires (diameter range of  $\sim 15$ -45 nm) with a [001] growth direction using the arc-discharge method. Gao *et al.* synthesized

[ $40\bar{1}$ ]  $\beta$ -Ga<sub>2</sub>O<sub>3</sub> nanowires with diameters ranging from ~10-100 nm in a vertical radio-frequency furnace [9]. Interestingly, the Raman mode frequencies of the [001]  $\beta$ -Ga<sub>2</sub>O<sub>3</sub> nanowires coincide with the corresponding frequencies in bulk  $\beta$ -Ga<sub>2</sub>O<sub>3</sub> as can be seen in Fig. 1.5 (chapter 1). On the other hand, the Raman mode frequencies of the [ $40\bar{1}$ ]  $\beta$ -Ga<sub>2</sub>O<sub>3</sub> nanowires are redshifted (shifted lower in energy) relative to corresponding frequencies in bulk  $\beta$ -Ga<sub>2</sub>O<sub>3</sub> by 4-23 cm<sup>-1</sup> (see Chapter 1, Fig. 1.5). Using plasma enhanced chemical vapor deposition, we have synthesized  $\beta$ -Ga<sub>2</sub>O<sub>3</sub> nanowires whose growth is along [110] direction and whose vibrational spectra are blueshifted (shifted to higher energies) as will be described below. This study focuses on the micro-Raman and FTIR characterization of [110]  $\beta$ -Ga<sub>2</sub>O<sub>3</sub> nanowires grown by plasma-CVD, and first principle calculations of the Raman mode frequencies under growth induced internal strains. Our calculated Raman frequency shifts suggest that the observed shifts in the nanowires with the [ $40\bar{1}$ ] and [110] growth directions can be explained in terms of different internal strains, in contrast to the previously suggested quantum confinement effects and defect induced effects [27]. The chapter outline is as follows: First the synthesis and growth mechanism of the [110]  $\beta$ -Ga<sub>2</sub>O<sub>3</sub> nanowires is described, followed by the electron microscopy characterization. Then the Raman modes of bulk  $\beta$ -Ga<sub>2</sub>O<sub>3</sub> and the nanowires are compared followed with a similar comparison for infrared modes. Discrepancies between the Raman spectra from nanomaterials and the corresponding bulk material could be related to quantum confinement effects. Phonon confinement in nanomaterials is reviewed in the next section, followed by a theoretical model which seeks to

explain the nature of the difference in the experimentally observed Raman spectra between bulk  $\beta\text{-Ga}_2\text{O}_3$  and the nanowires.

### Nanowire synthesis

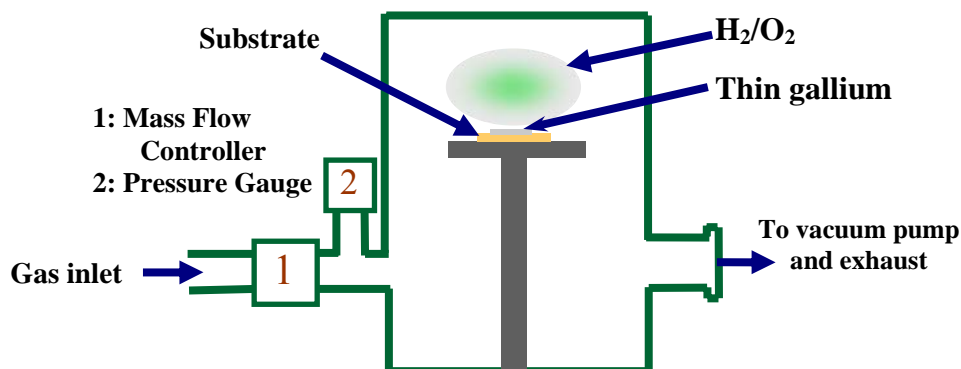


Figure 3.1: Schematic of the microwave plasma CVD reactor used to synthesize gallium oxide nanowires [25].

Synthesis of the  $\beta\text{-Ga}_2\text{O}_3$  nanowires was carried out in a microwave plasma reactor (ASTEX 5010) with  $\text{H}_2/\text{CH}_4/\text{O}_2$  gas mixtures as shown in Fig. 3.1 above. Quartz substrates were covered with a thin film of molten gallium and were exposed to a microwave plasma containing a range of gas phase species. During the plasma exposure, molten gallium flowed on all the substrates, forming a thin film, which was followed by growth of nanowires. The substrate temperature was measured by an infrared pyrometer to be approximately 550 °C for 700 W microwave power, 40 Torr total pressure, and 8.0 sccm of  $\text{O}_2$  in 100 sccm of hydrogen in the inlet stream. The experiments were performed at the following range of growth conditions: microwave power of 600-1200 W, pressure

of 30-60 Torr, growth duration of 1-12 h, 0.6-10 sccm of O<sub>2</sub> and 0-2 sccm of CH<sub>4</sub> in 100 sccm of hydrogen in the feed gas [25].

### Growth Mechanism

The nanowires synthesized by plasma-CVD grow according to a method reported by Sharma *et al* [25]. This technique is based on the unique wetting characteristics of liquid gallium. The requirement for this growth mechanism is that the material of interest should have low solubility and low wetting characteristics with respect to liquid gallium. A schematic of the growth model is presented in Fig. 3.4.

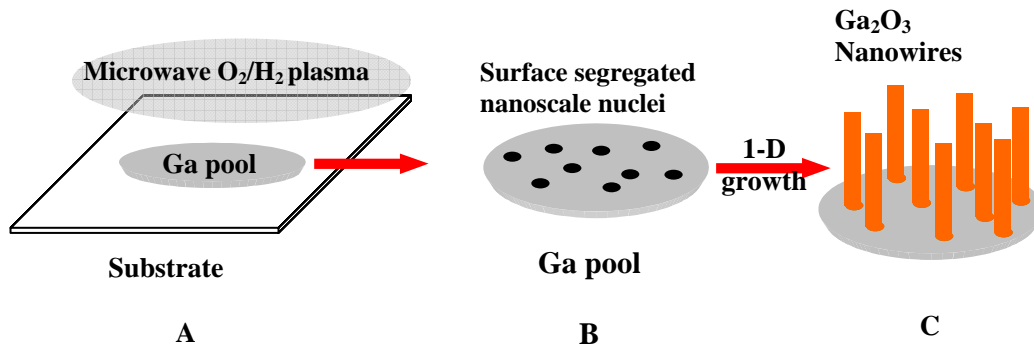


Figure 3.2: Schematic for the growth process of gallium oxide nanowires [25].

The steps in this gallium-based growth process are as follows [25]: Substrates coated with gallium metal are loaded into the reaction chamber, which is then ramped up to the reaction temperature. The melting point of gallium is 30 °C and by the time the reactor reaches its desired working temperature, a thin film

of molten gallium is produced on the surface of the substrate. At this point, a microwave plasma containing oxygen and hydrogen is introduced into the chamber (Fig. 3.2, A). Oxygen readily reacts with gallium to form nanometer-sized nuclei within the gallium pool (Fig. 3.2, B). Gallium oxide has poor solubility within gallium and thus as more of the oxide is formed and the gallium is exhausted, the oxide pushes off the substrates and forms nanowires (Fig. 3.2, C). At the end of the reaction, the molten gallium pool gets converted to gallium oxide nanowires [25]. In contrast to the more common vapor-liquid-solid growth process [26, 28], this method does not make use of any metal catalyst to seed the growth of the nanowire and is similar to the vapor-solid process in that respect. In similar experiments, gallium metal has been used as the growth medium for the synthesis of both carbon and silicon nanowires [29].

The conversion of gallium to gallium oxide during the plasma CVD reaction can be confirmed via Raman spectroscopy. Metallic gallium in solid form exhibits a Raman peak at  $246\text{ cm}^{-1}$  [30] due to Ga-Ga stretching vibrations, and a Raman peak for gallium was observed in non-optimized experiments in which the reactor was shut down a few minutes after the plasma was introduced, thus suggesting that all the gallium on the substrate did not convert to gallium oxide. Some of the gallium did react with the limited amount of oxygen and formed the oxide in certain regions of the substrate (Fig. 3.3). In all the gallium oxide nanowire samples discussed in this chapter we ensured that the  $246\text{ cm}^{-1}$  peak for gallium was absent.

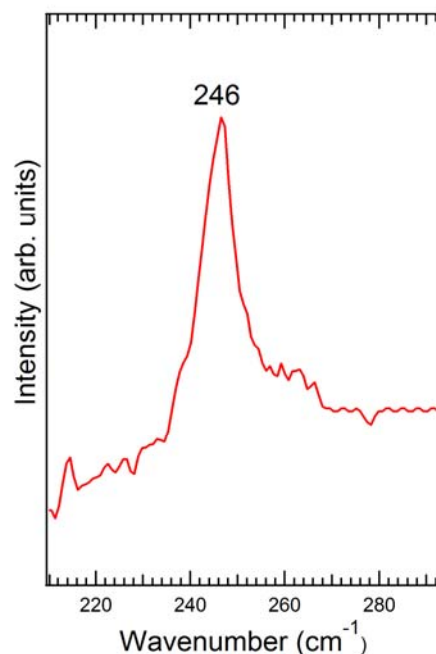


Figure 3.3: Raman spectrum of a gallium-coated substrate in which the entire gallium pool did not react with oxygen in a non-optimized experiment.

#### Electron microscopy of $\beta$ -Ga<sub>2</sub>O<sub>3</sub> nanowires

The morphology of the as-prepared nanomaterials was analyzed via scanning electron microscopy (SEM model Hitachi S-4700), high-resolution transmission electron microscopy (HRTEM model – JEOL 3010) and electron diffraction. The analysis of the selected area diffraction patterns (SAD) was performed with the help of simulations using a software package (Desktop Microscopist from the NCEM-LBL). The nanowires were dispersed in acetone using ultrasonication for ~30 s or until a uniform dispersion was obtained. A few drops of the dispersion were then used on a 200 mesh holey carbon TEM Cu grid (EMS - Electron Microscopy Sciences).



Figure 3.4 shows a scanning electron micrograph of  $\beta$ -Ga<sub>2</sub>O<sub>3</sub> nanowires grown from a large molten gallium droplet. Nanowires were seen to be dispersed uniformly over the substrates. Figure 3.5 shows a high resolution transmission electron micrograph (TEM) of an individual 13 nm thick single-crystalline Ga<sub>2</sub>O<sub>3</sub> nanowire (nanowire 1). Electron diffraction from the nanowire confirmed its growth direction to be along [110] crystallographic direction. A second nanowire (nanowire 2) is also visible in the vicinity of nanowire 1 on the TEM grid, lying in a different plane tilted with respect to that of nanowire 1. Also, analysis of the x-ray diffraction patterns (not shown here) yielded  $a_0 = 12.23 \text{ \AA}$ ,  $b_0 = 3.04 \text{ \AA}$ ,  $c_0 = 5.8 \text{ \AA}$ ,  $\beta = 103.7^\circ$ , confirming the presence of a monoclinic  $\beta$ -Ga<sub>2</sub>O<sub>3</sub> phase in these nanowires.

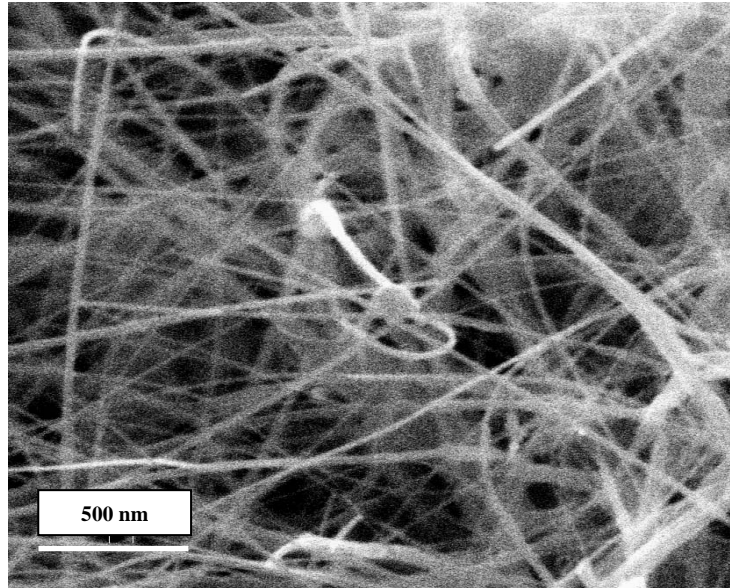


Figure 3.4: SEM micrograph of  $\beta$ -Ga<sub>2</sub>O<sub>3</sub> nanowires grown from a large molten gallium droplet using a microwave plasma mediated technique [25].

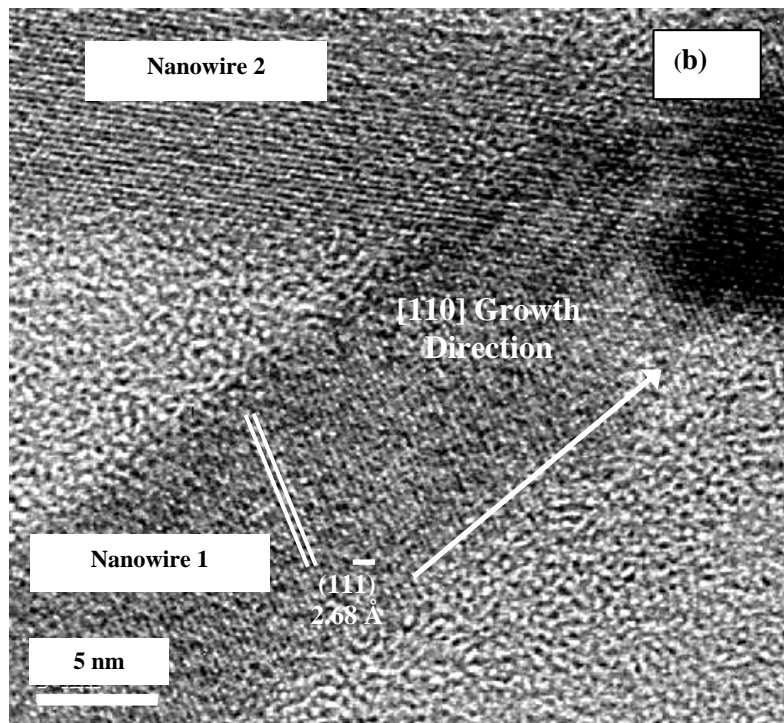


Figure 3.5: A high resolution TEM image of an individual 13 nm thick  $\beta$ -Ga<sub>2</sub>O<sub>3</sub> nanowire [25].

#### Raman modes of $\beta$ -Ga<sub>2</sub>O<sub>3</sub>

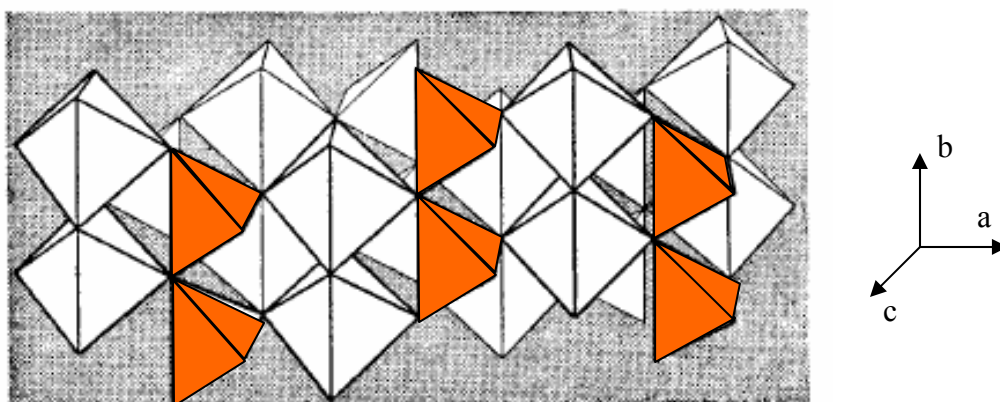


Figure 3.6: Representation of the tetrahedra and octahedra which form the structure of  $\beta$ -Ga<sub>2</sub>O<sub>3</sub> [31].

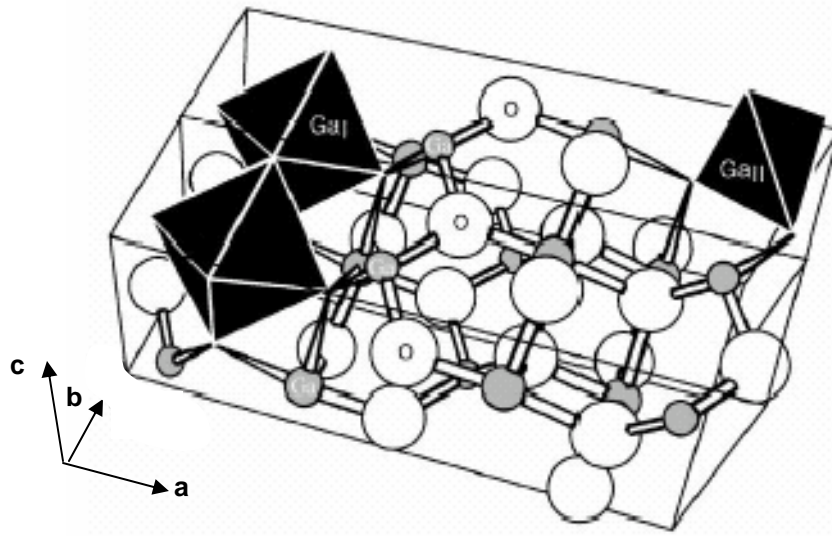


Figure 3.7: Unit cell of monoclinic  $\beta$ -Ga<sub>2</sub>O<sub>3</sub> [32].

$\beta$ -Ga<sub>2</sub>O<sub>3</sub> has a monoclinic structure and belongs to the  $C_{2h}^3$  space group [33]. Its unit cell contains two formula units- GaO<sub>6</sub> (edge sharing) octahedra containing Ga<sub>I</sub> ions and GaO<sub>4</sub> (corner sharing) tetrahedra containing Ga<sub>II</sub> ions as shown in Figs. 3.6 and 3.7. A tetrahedron shares only corners with other tetrahedra in the  $b$  axis direction and with octahedra in the other direction. In other words, the  $b$ -direction of the gallium oxide unit cell contains chains of GaO<sub>6</sub> octahedra that are arranged parallel to the axis. These chains are connected by GaO<sub>4</sub> tetrahedra to one another (Fig. 3.6) [32].

Under the  $C_{2h}^3$  group, group theory predicts 15 Raman and 12 infrared active vibrational modes [31]. The Raman-active modes of  $\beta$ -Ga<sub>2</sub>O<sub>3</sub> can be classified into three groups: high frequency stretching and bending of GaO<sub>4</sub> tetrahedra ( $\sim 770 - 500 \text{ cm}^{-1}$ ), mid-frequency deformation of Ga<sub>2</sub>O<sub>6</sub> octahedra ( $\sim$

480–310  $\text{cm}^{-1}$ ), and low-frequency libration (frustrated rotation) and translation (below 200  $\text{cm}^{-1}$ ) of tetrahedra-octahedra chains. Figure 3.8 below shows a micro-Raman spectrum obtained from bulk  $\beta\text{-Ga}_2\text{O}_3$ . The micro-Raman spectrum was collected from bulk gallium oxide films grown via thermal CVD on quartz substrates and correspond with the reported Raman peak frequencies for bulk  $\beta\text{-Ga}_2\text{O}_3$  reported by Dohy *et al.* [31].

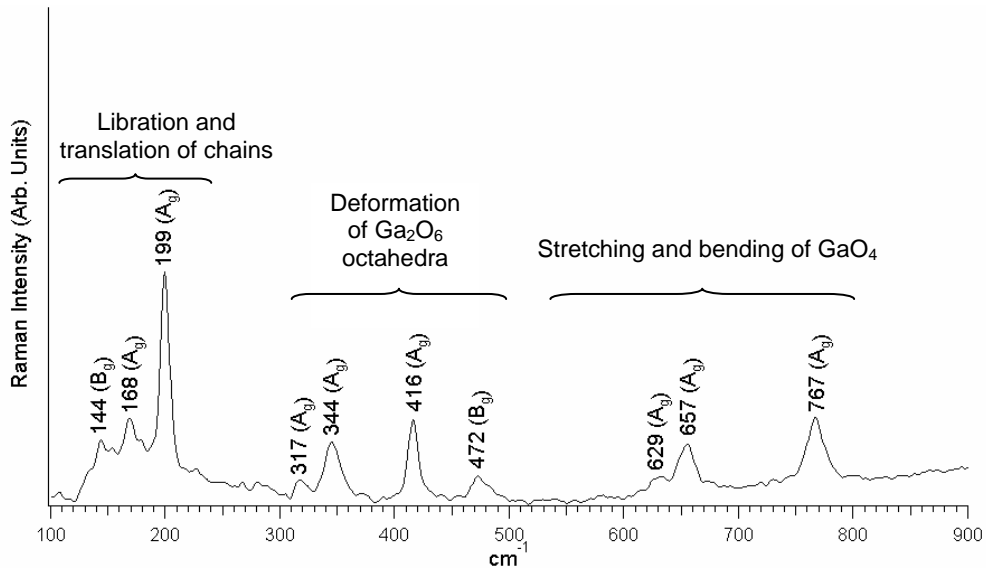


Figure 3.8: Micro-Raman spectrum of bulk  $\beta\text{-Ga}_2\text{O}_3$

In their experimental and theoretical study, Dohy *et al.* assigned symmetries to all the observed experimental modes. It turns out that due to the complexity of the gallium oxide crystal structure, the various types of bond vibrations, viz., bending and stretching of octahedra and tetrahedra,  $\text{Ga}_{\text{I}}\text{-O}_2$  and  $\text{Ga}_{\text{II}}\text{-O}_2$  bonds are heavily coupled. For example, the eigenmodes of the 111  $\text{cm}^{-1}$

$A_g$  mode are composed of various  $\text{GaO}_2$  bending modes as can be seen below in Fig. 3.9. The vibrations of other modes, such as the  $657\text{ cm}^{-1}$  (Fig. 3.8) are more complex, including tetrahedra and octahedra stretching, as well as bending of  $\text{GaO}_2$  bonds. Moreover, due to larger force constants, the shorter bonds in the tetrahedra contribute largely to the high frequency vibrational modes in  $\beta\text{-Ga}_2\text{O}_3$ ; in particular, oxygen atom displacements are high in the high frequency tetrahedral bending and stretching modes. On the other hand, gallium atom displacements contribute largely to the low frequency librational and translational modes (Fig. 3.9).

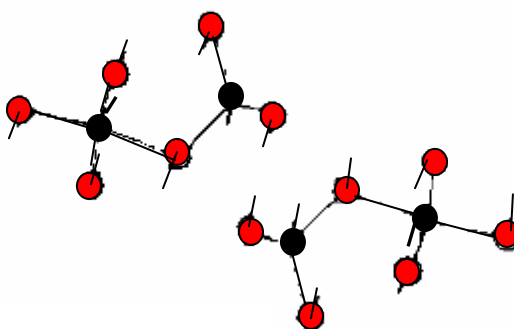


Figure 3.9: Cartesian displacements involved in the in-plane  $A_g$  vibrational mode at  $111\text{ cm}^{-1}$  in  $\beta\text{-Ga}_2\text{O}_3$ . The gallium and oxygen atoms are shown by the black and red dots respectively [31].

The Raman mode frequencies for bulk  $\beta\text{-Ga}_2\text{O}_3$  measured in this study (Fig. 3.8) correspond well to those reported in the literature. A noteworthy point is that no experimental analysis on the mode symmetry of  $\beta\text{-Ga}_2\text{O}_3$  Raman peaks has been reported. Our current mode symmetry assignment is purely based on the

comparison between the observed and calculated Raman frequencies. We find an unambiguous matching pattern for mode symmetry assignment for all the observed Raman modes, except for the two Raman peaks around  $472\text{ cm}^{-1}$  and  $628\text{ cm}^{-1}$ . The former peak can be assigned with either the calculated  $A_g$  mode of  $469\text{ cm}^{-1}$  or the  $B_g$  mode of  $474\text{ cm}^{-1}$ , while the latter one can be assigned with either the  $A_g$  mode of  $601\text{ cm}^{-1}$  or the  $B_g$  mode of  $624\text{ cm}^{-1}$ . The spectra of the nanowires were obtained by dispersing nanowires on quartz substrates. All spectra were collected from individual nanowires and nanowire-rich regions present on the quartz substrates with a Renishaw 1000 Raman microscope using a 50x objective. The samples were excited with the 785 nm, 514 nm, or 442 nm excitations from a solid state laser and the backscattered Raman spectra were collected with an air-cooled CCD (Fig. 3.10)

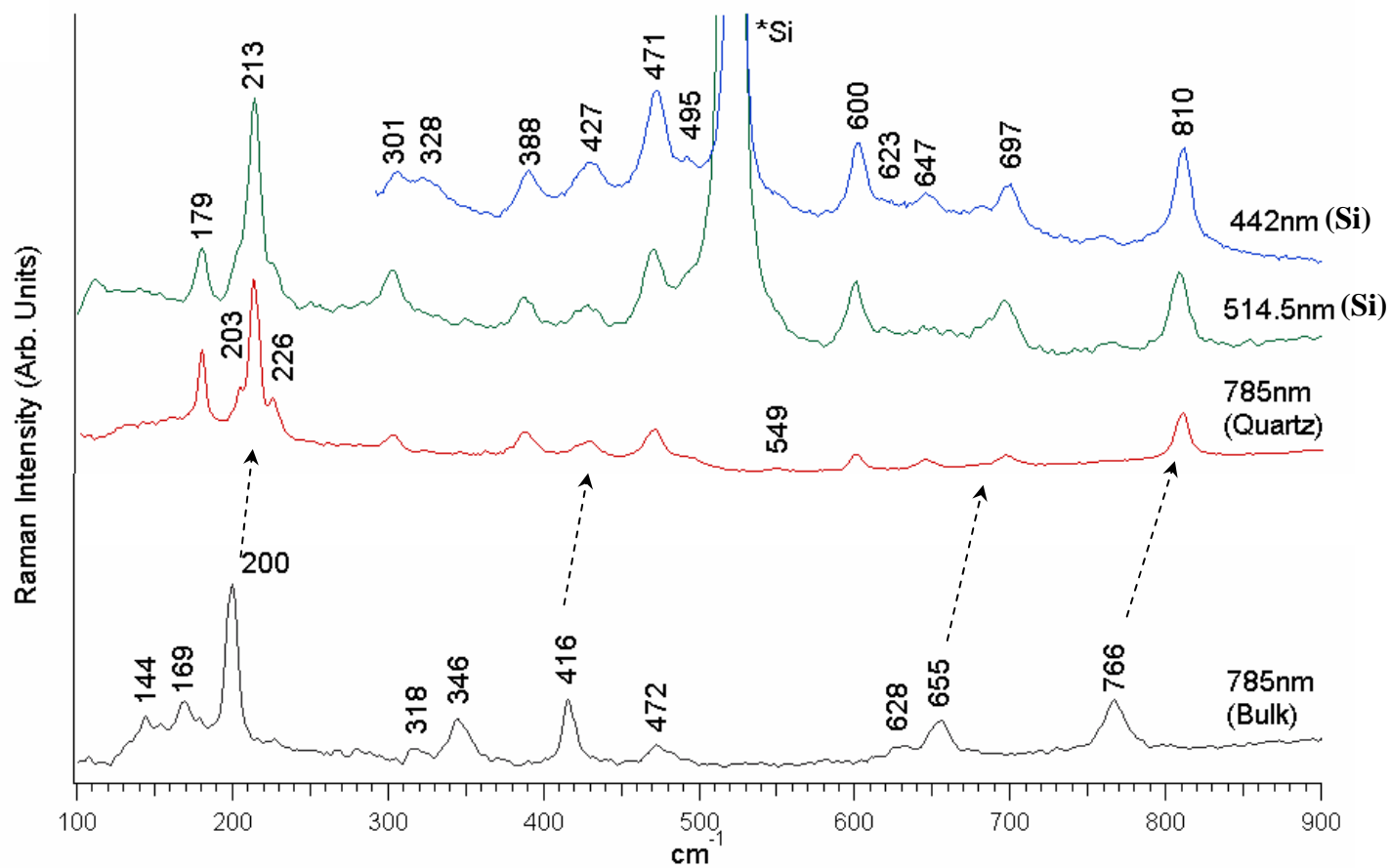


Figure 3.10: Micro-Raman spectra of  $\beta\text{-Ga}_2\text{O}_3$  nanowires (top three traces) dispersed on quartz and silicon substrates collected at three different excitations showing peaks upshifted compared to bulk  $\beta\text{-Ga}_2\text{O}_3$  [31] (bottom trace).

In contrast to the Raman spectrum from bulk  $\beta$ -Ga<sub>2</sub>O<sub>3</sub>, the Raman spectrum of the [110] nanowires, is relatively richer and is significantly *blueshifted* in frequency (Fig. 3.10). Correlating the Raman peaks present in the spectrum for [110] nanowires and those in the bulk is simple for the modes located at either end of the Raman spectra. For the low frequency libration/translation modes, we can identify the strongest Raman peak of 200 cm<sup>-1</sup> in the bulk being shifted to 213 cm<sup>-1</sup> in the spectrum for the nanowires. Accordingly, we attribute the nearby 180 cm<sup>-1</sup> mode as shifted from the 169 cm<sup>-1</sup> mode in the bulk. The relatively weaker 144 cm<sup>-1</sup> bulk Raman peak is invisible in the spectra of the nanowires, likely due to reduction of peak intensity. Meanwhile, a minor peak appears in the low frequency region of the nanowires spectra, which cannot be related to any calculated bulk Raman active modes. Overall, the librational/translational modes are blueshifted by ~10 cm<sup>-1</sup>. On the other end of the Raman spectra, two highest frequency stretching/bending modes of tetrahedra are found to be blueshifted by nearly ~40 cm<sup>-1</sup>, i.e. 766cm<sup>-1</sup>  $\rightarrow$  810 cm<sup>-1</sup> and 655 cm<sup>-1</sup>  $\rightarrow$  697 cm<sup>-1</sup>. The third highest frequency Raman peak observed in the nanowires at 645 cm<sup>-1</sup> is assigned as the blueshifted 628 cm<sup>-1</sup> mode in the bulk. There is a fourth peak in the high frequency region (around 600 cm<sup>-1</sup>). The only possible match for this peak is with the unobserved bulk Raman mode (either the A<sub>g</sub> mode of 601 cm<sup>-1</sup> or the B<sub>g</sub> mode of 624 cm<sup>-1</sup>) predicted by our calculation described below. While the overall shifting pattern of the Raman peaks in the intermediate frequency ranges is clearly blueshifted, the exact peak-to-peak correspondences are less clear, partially because several additional weak peaks



are also observed (for example at  $225\text{ cm}^{-1}$ ,  $302\text{ cm}^{-1}$ ) of which neither correspond to the infrared peaks expected in  $\beta\text{-Ga}_2\text{O}_3$  [31]. Tentatively, we assume that the bulk modes at  $416\text{ cm}^{-1}$  and  $472\text{ cm}^{-1}$  are shifted to  $428\text{ cm}^{-1}$  and  $492\text{ cm}^{-1}$  respectively. As discussed in the following section of theoretical results, this assumption is consistent with our calculations.

The nanowires were excited at three different laser frequencies in order to determine if the Raman peaks of nanocrystalline  $\beta\text{-Ga}_2\text{O}_3$  are dependent on the excitation wavelengths. Raman spectra of various 1D materials such as carbon nanotubes [34], silicon nanowires [35], and quantum dots [36] have exhibited excitation wavelength dependence with respect to nanomaterial dimension. The  $\beta\text{-Ga}_2\text{O}_3$  nanowires examined in this study did not show any dependence on the excitation wavelength as seen in Fig. 3.10 above and the Raman peaks of the nanowires are consistently up-shifted compared to the corresponding peaks in bulk  $\beta\text{-Ga}_2\text{O}_3$ .

Shifts in Raman peak frequencies could be caused due to stoichiometric changes within the material, as well as the presence of different phases. Gallium oxide is known to grow in four different phases –  $\alpha$ -,  $\beta$ -,  $\gamma$ -, and  $\delta\text{-Ga}_2\text{O}_3$ . Of these four phases, the alpha and beta phase of gallium oxide are stable. A comparison of the Raman spectrum obtained from the  $[110]\beta\text{-Ga}_2\text{O}_3$  nanowires with the Raman spectrum of  $\alpha\text{-Ga}_2\text{O}_3$  (Fig. 3.11), however, proves that our nanowires do not correspond to the alpha phase. As discussed earlier in this chapter, based on the Raman spectrum of unreacted gallium, we rule out the

features observed in Fig. 3.10 to residual metallic gallium. Finally, the gallium oxide nanowires were checked for oxygen deficiencies by annealing the wires at high temperatures in an oxygen environment. The Raman spectra of the  $\beta$ -Ga<sub>2</sub>O<sub>3</sub> nanowires was found to be unchanged after annealing and still showed the same upshift in peak frequencies with respect to bulk  $\beta$ -Ga<sub>2</sub>O<sub>3</sub>. McGuire *et al.* [37] performed a systematic study of SnO<sub>2</sub> and ZnO nanobelts and found changes in the Raman spectra due to the formation of off-stoichiometric phases (Sn<sub>x</sub>O<sub>y</sub>) of tin oxide that changed with annealing of the nanobelts in an oxygen-rich environment. However, no such effect was observed in the present study thus confirming the presence of  $\beta$ -Ga<sub>2</sub>O<sub>3</sub> nanowires. Furthermore, as explained below, these nanowires were also characterized with FTIR spectroscopy and exhibited similar peak upshifts with respect to bulk  $\beta$ -Ga<sub>2</sub>O<sub>3</sub> in the FTIR transmittance spectra.

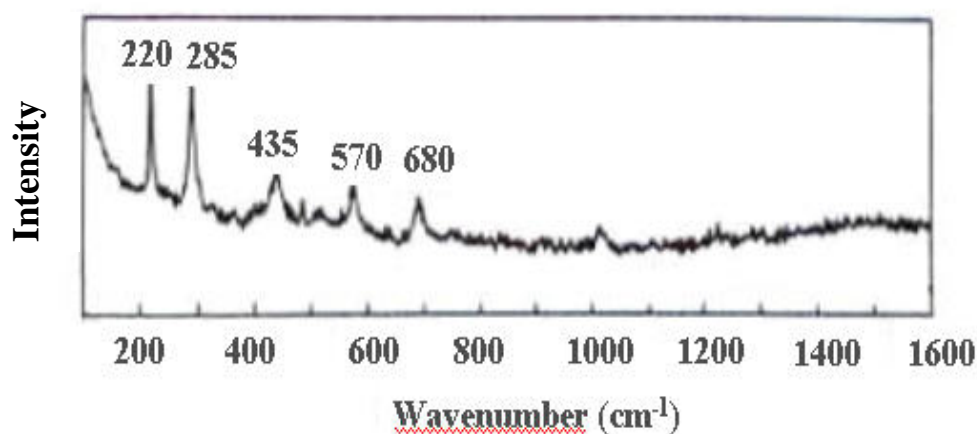


Figure 3.11: Raman spectrum of  $\alpha$ -Ga<sub>2</sub>O<sub>3</sub> [38].

Interestingly, the red-shift in the phonon frequencies (c.f. Fig. 1.5) has also been attributed by Gao *et al.* [9] to the presence of impurities and defects, such as point defects, twins, and stacking faults [39]. These defects are also likely to be responsible for additional vibrational modes observed in the Raman spectra (and to a small extent in the FTIR spectrum) of nanowires. From a detailed high resolution transmission electron microscopy study, Gao *et al.* confirmed the presence of twins and edge dislocations in their nanowires as shown below in Fig. 3.12 [9]. Dai *et al.* [40] also proposed that the O vacancies and the stacking faults caused an abnormality in the Ga-O bond vibration and led to red-shift in the Raman frequencies.

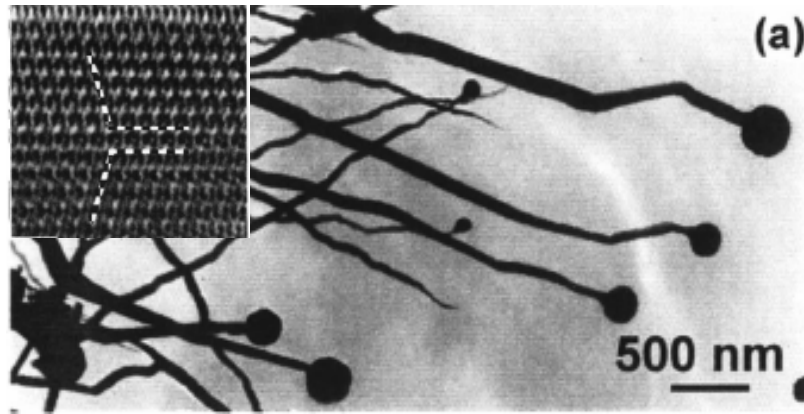


Figure 3.12: SEM image of the  $[40\bar{1}]$  nanowires grown by RF-induction. The inset is a high resolution TEM image from one of the wires showing twinned planes [9].

Although this simple hypothesis is plausible, there is one obvious weakness, i.e. lack of close correlation between defect types and the growth directions. Presumably, similar defects might exist in the nanowires with

different growth directions. It is also not clear which types of defects will lead to a blueshift in vibrational frequencies. Moreover, different regions in the nanowires contain different defects which would imply that different shifts in the Raman and/or IR spectra should be observed when different regions of the *same* nanowire are probed. However, this doesn't seem to be the case and instead overall distinct blueshifts or redshifts have been observed for a given nanowire. Furthermore, extensive electron microscopy study of our [110] nanowires revealed that the wires are largely defect-free, which fails to account for the consistent upshift seen in the Raman spectra from various [110] nanowire samples. Therefore, alternative models that are capable of describing these diverse Raman peak-shift patterns in a consistent fashion are needed.

### FTIR Spectroscopy

Fourier-transform infrared spectroscopy (FTIR) is a vibrational spectroscopy technique that is complementary to Raman spectroscopy. The technique deals with the absorption (or transmission) of infrared light by a sample. Analogous to Raman spectroscopy, the incoming infrared radiation when absorbed by a material induces a dipole moment within it. At certain molecular vibrational frequencies, the interaction of the molecule with the incoming radiation causes a change in the dipole moment of the molecule. Thus the molecule absorbs (or transmits) infrared radiation at that particular vibrational frequency. Since polar bonds have strong dipole moments, such molecules (for example, H<sub>2</sub>O) are highly infrared active [41].

Figure 3.13 shows the corresponding FTIR transmittance spectra for the same samples whose micro-Raman spectra appear in Fig. 3.10. FTIR transmittance spectra in the mid-infrared region were obtained using a Bruker IFS 66 v/s spectrometer from pressed potassium bromide pellets containing 3 wt. % dispersions of either powder or nanowire forms of  $\beta$ -Ga<sub>2</sub>O<sub>3</sub>. Polycrystalline gallium oxide powder was obtained by scraping off the deposit from substrate that was collected from the reactor during a non-optimized experiment. A KBr beamsplitter was used in the interferometer and the transmitted light was collected with a deuterated triglycine sulfate (DTGS) detector. The sample chamber was kept evacuated in order to eliminate the interfering infrared absorption by the water vapor present in the ambient atmosphere. As mentioned earlier in the chapter, group theory predicts that  $\beta$ -Ga<sub>2</sub>O<sub>3</sub> has 12 infrared modes. The bottom trace in Fig. 3.13 corresponds to bulk  $\beta$ -Ga<sub>2</sub>O<sub>3</sub>. Among the 12 IR modes, 6 modes lie below 400 cm<sup>-1</sup>; however due to the limited range of the instrument, only modes above 400 cm<sup>-1</sup> were measured. The spectrum from the  $\beta$ -Ga<sub>2</sub>O<sub>3</sub> powder corresponds well with the infrared spectrum for bulk  $\beta$ -Ga<sub>2</sub>O<sub>3</sub> [31]. On the other hand, consistent with the Raman spectrum (Fig. 3.10), the IR modes in the nanowire spectrum are also blueshifted in frequency relative to corresponding bulk frequencies. The upshift of the IR modes of the nanowires also follows a similar trend like the Raman peaks. Lower frequency peaks shift by around 16 cm<sup>-1</sup> while the frequencies above 600 cm<sup>-1</sup> in  $\beta$ -Ga<sub>2</sub>O<sub>3</sub> nanowires are upshifted in frequency by as much as 50 cm<sup>-1</sup>.

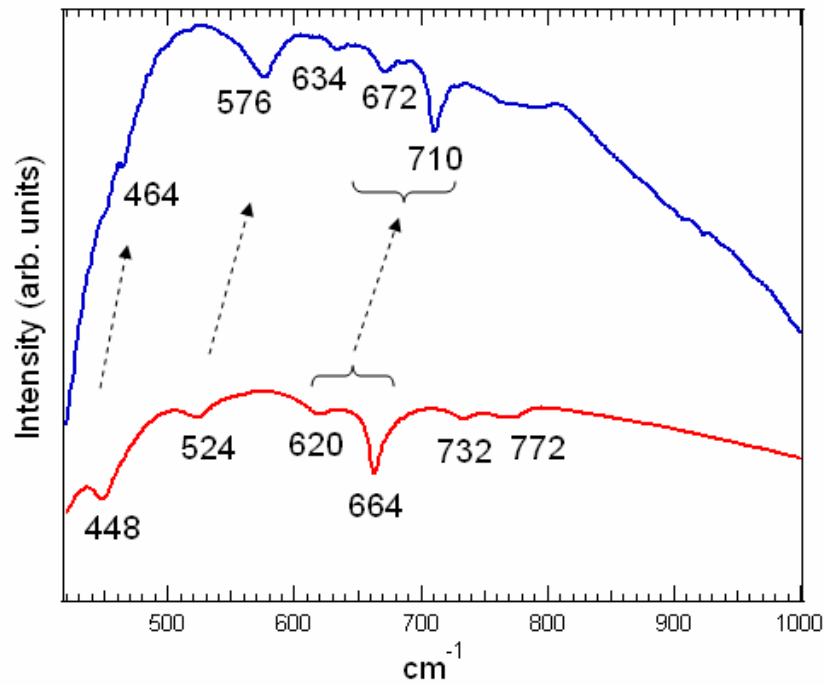


Fig. 3.13: FTIR transmittance spectra of bulk (bottom trace) and [110]  $\beta$ -Ga<sub>2</sub>O<sub>3</sub> nanowires (top trace).

#### Raman peak shifts due to quantum confinement

In recent years, much attention has been drawn to quantum confinement effects in nanomaterials. Decrease in dimensionality of a material leads to confinement of electrons and phonons, thus leading to changes in properties that are not observed in the corresponding bulk counterpart. In the case of Raman spectroscopy, phonon confinement is known to cause peak broadening and shifts. For example, Fig. 3.14 below shows Raman spectra collected from silicon nanowires of various average diameters [35]. The 520 cm<sup>-1</sup> mode of bulk silicon,

which is shown in the bottom trace, can be seen to downshift and broaden with a decrease in average wire diameter down to 4.5 nm.

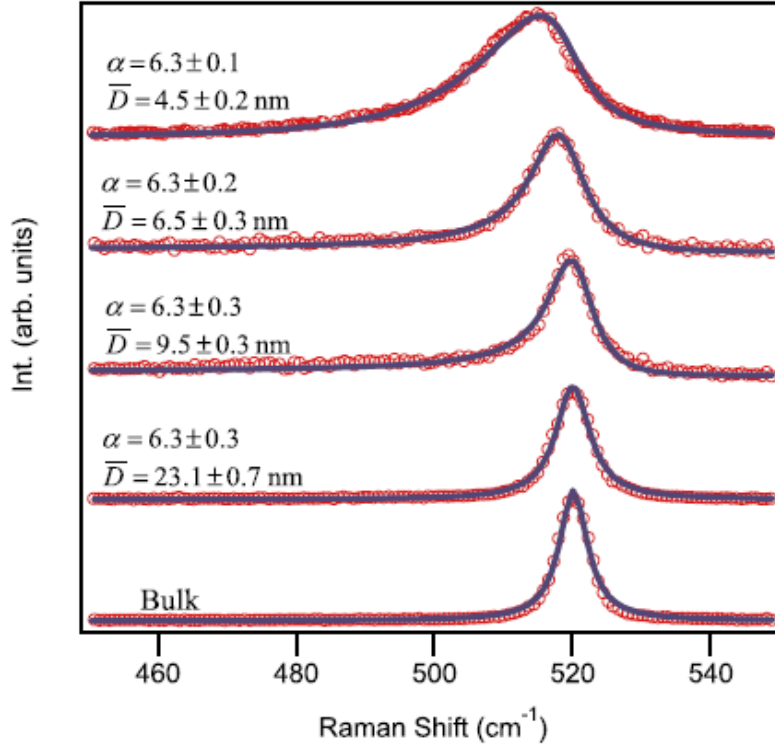


Figure 3.14: Raman spectra showing the evolution of the first-order  $520 \text{ cm}^{-1}$  peak of four silicon nanowire samples [35].

With respect to phonon dispersion in the Brillouin zone, the conservation of crystal momentum demands that only zone-center ( $q = 0$ ) Raman-active optical phonons get excited in a given Raman experiment. However, in samples with reduced dimensionality, the conservation of crystal momentum is relaxed and off zone-center phonons become Raman-active. Depending on the phonon density of

states (DOS) of the material, these phonons are manifested as upshifted or downshifted or broadened Raman peaks in the spectrum. Richter *et al.* [42] developed a heuristic model to explain phonon confinement in silicon microcrystals. Later, Campbell and Fauchet [43] refined Richter's model to include 1D and 2D morphologies. These models have been successfully applied to many nanoscale materials and explain the change in the Raman spectrum of low-dimensional materials. The key aspect of the confinement model is the use of a localization function for the phonons in the crystal. In an infinite crystal, the wavefunction of a phonon with wavevector  $q_0$  can be written as

$$\phi(\vec{q}_0, \vec{r}) = U(\vec{q}_0, \vec{r}) \exp(-i\vec{q}_0 \cdot \vec{r}) \quad (3.1)$$

where  $U(q_0, r)$  has the periodicity of the lattice. In a crystallite assumed to be spherical with a diameter  $L$  the phonon is restricted to the volume of the crystallite. A simple method to localize the phonon is to introduce a Gaussian function such that the phonon wavefunction now becomes

$$\psi(\vec{q}_0, \vec{r}) = A \exp\left\{-\frac{r^2}{2} \middle/ \left(\frac{L}{2}\right)^2\right\} \phi(\vec{q}_0, \vec{r}) \quad (3.2)$$

$$= \psi'(\vec{q}_0, \vec{r}) \cdot U(\vec{q}_0, \vec{r})$$

with



$$|\psi|^2 = A^2 \exp \left\{ -r^2 / \left( \frac{L}{2} \right)^2 \right\}$$

Thus according to the above expression, the phonon wavefunction  $\psi$  is localized to  $|r| \leq L$  in the form of a Gaussian distribution.  $\psi'$  can be expanded in a Fourier series:

$$\psi'(\vec{q}_0, \vec{r}) = \int d^3 q C(\vec{q}_0, \vec{q}) \exp(i\vec{q} \cdot \vec{r}) \quad (3.3)$$

where the Fourier coefficients  $C(q_0, q)$  are given by

$$C(\vec{q}_0, \vec{q}) = \frac{1}{(2\pi)^3} \int d^3 r \psi'(\vec{q}_0, \vec{r}) \exp(-i\vec{q} \cdot \vec{r}) \quad (3.4)$$

Inserting  $\psi'$  from eq. (3.3) into eq. the above expression yields

$$C(\vec{q}_0, \vec{q}) = \frac{AL}{(2\pi)^{3/2}} \exp \left\{ -\frac{1}{2} \left( \frac{L}{2} \right)^2 (q - q_0)^2 \right\} \quad (3.5)$$

This shows that the  $\psi'$  and therefore the  $\psi$  are no longer eigenfunctions of the phonon wavevector  $q_0$  but rather a superposition of eigenfunctions with wavevectors in an interval  $|q - q_0| \leq 1/2L$  centered at  $q_0$ . Also, the phonon transition matrix elements have non-vanishing values for  $q \neq q_0$ . This implies that the activations of off-zone center phonons, which leads to contributions from phonon energies away from  $q = 0$ . Figure 3.15 shows the phonon dispersion curves for silicon. From the figure, it can be seen that for the  $q = 0$  phonon the

dispersion is negative. In other words, for the  $F_{2g}$   $520\text{ cm}^{-1}$  peak (indicated by the dashed circle at  $\sim 15\text{ THz}$ ) the off-zone center phonons have frequencies less than  $520\text{ cm}^{-1}$ . Hence as crystal dimension decreases, more phonons away from the zone center contribute and lead to downshifts (redshifts) and broadening of the  $520\text{ cm}^{-1}$  peak.

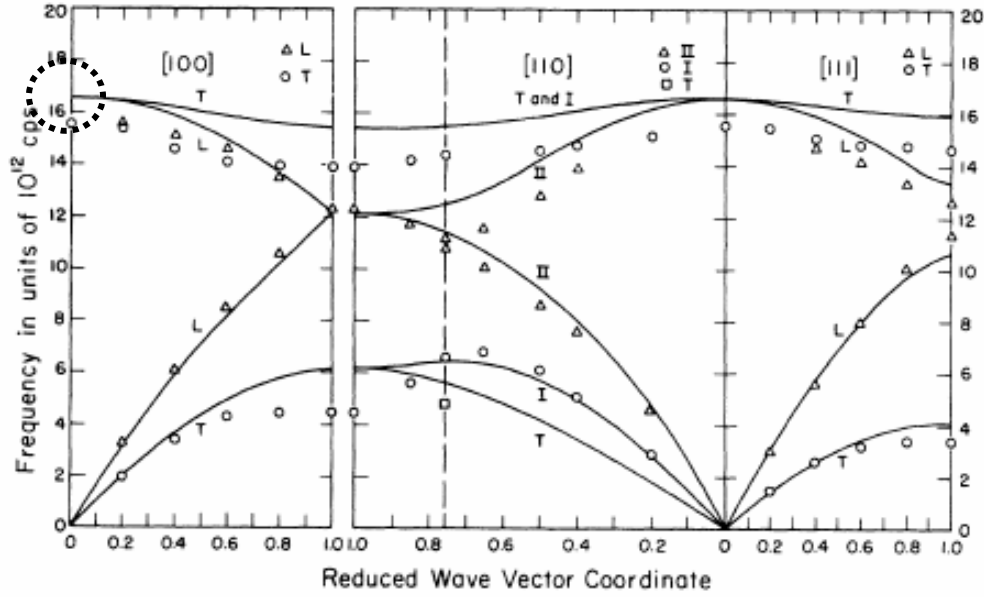


Figure 3.15: Phonon dispersion curves for silicon. Both neutron diffraction (points) and calculated (solid lines) data are shown [44].

On the other hand, in other materials like graphite the  $E_{2g}$  vibrational mode at  $\sim 1580\text{ cm}^{-1}$  upshifts with decreasing dimension as can be seen by the positive slope of the  $E_{2g}$  mode at the  $\Gamma$  point in Fig. 3.16 [45]. Since graphite is a layered structure, such a confinement effect is seen by decreasing the number of

layers. A single layer of graphite is called graphene, and Raman spectra collected on single and multiple layer graphene samples exhibit upshifts of the  $1580\text{ cm}^{-1}$  mode compared to bulk graphite as shown by an upshift of  $\sim 5\text{ cm}^{-1}$  in Fig. 3.17 for single-layered graphene compared to bulk graphite [46]. In other words, as the crystal dimension is decreased along the c-direction in a graphite crystal, quantum confinement causes the  $E_{2g}$  mode to upshift in frequency.

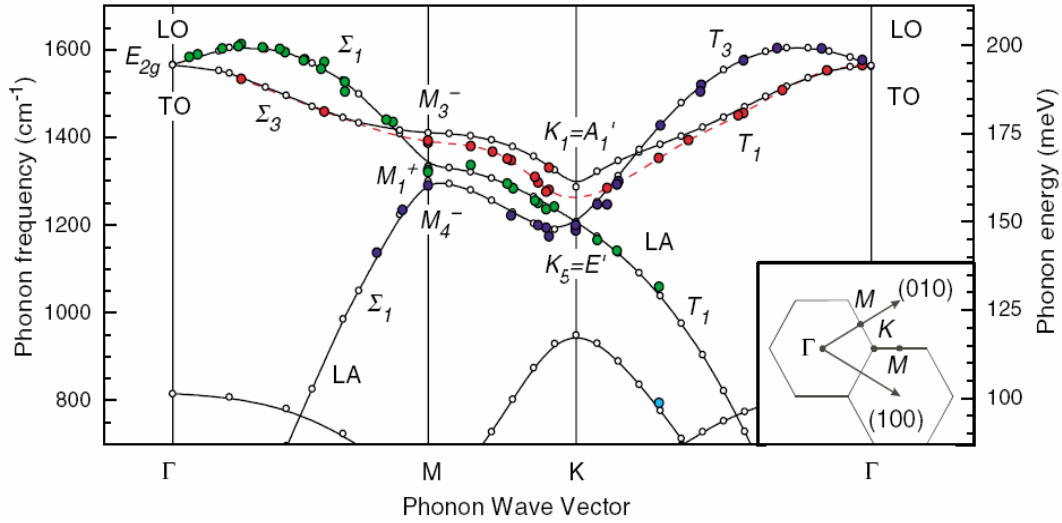


Figure 3.16: Calculated and experimental (inelastic x-ray scattering) phonon dispersion curves for graphite [45].

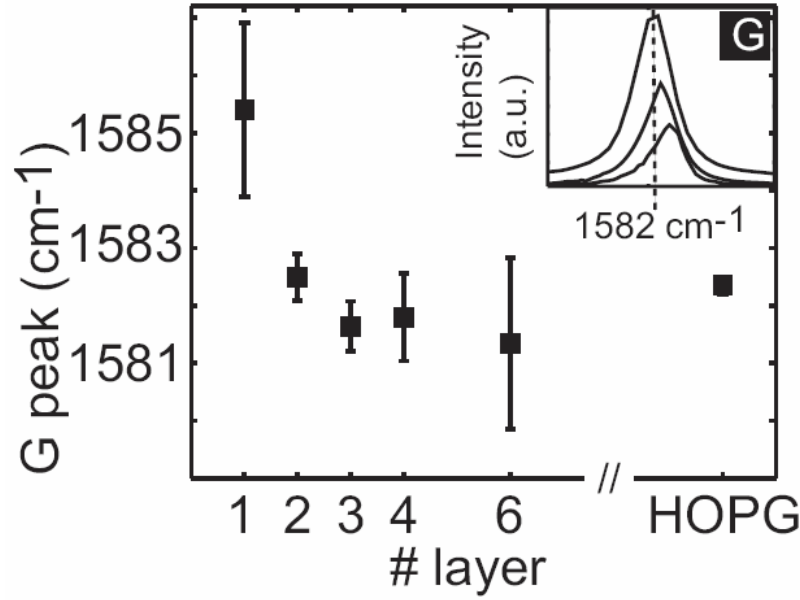


Figure 3.17: G peak frequency versus number of stacked layers (average value and standard deviation). Inset: G peak for highly oriented pyrolytic graphite (HOPG) (upper peak), double- (middle peak) and single-layer (lower peak) graphene. The vertical dashed line indicates the reference value for bulk graphite [47].

Returning to Fig. 3.10 for our gallium oxide nanowires, the average diameter of our  $\beta$ -Ga<sub>2</sub>O<sub>3</sub> nanowires (as well as that for the [001] and the [40 $\bar{1}$ ] nanowires) is around 30 nm. It is unlikely that the quantum size confinement at this length scale is significant enough to cause the phonon shifts as large as 50 cm<sup>-1</sup> seen in Fig. 3.10. Furthermore, three distinctly different shift patterns have been experimentally observed for the  $\beta$ -Ga<sub>2</sub>O<sub>3</sub> nanowires depending on their growth directions. In contrast to the blueshift in the Raman and FTIR spectra observed in Figs. 3.10 and 3.13, Choi *et al.* reported their Fourier transform Raman spectrum of [001]  $\beta$ -Ga<sub>2</sub>O<sub>3</sub> nanowires to be identical to that of bulk  $\beta$ -Ga<sub>2</sub>O<sub>3</sub> (c.f., Fig. 1.6), while Gao *et al.* exhibited a *red-shift* of 4-23 cm<sup>-1</sup> in

frequency of their  $[40\bar{1}]$   $\beta$ -Ga<sub>2</sub>O<sub>3</sub> nanowires relative to the corresponding Raman frequencies in bulk  $\beta$ -Ga<sub>2</sub>O<sub>3</sub> (c.f. Fig. 1.5). The size confinement effect is clearly insufficient to explain observed the Raman shifts by Gao *et al.*, Choi *et al.*, and us and therefore other mechanisms have to be examined in detail as described in the next section.

### LDA model of the peak frequencies of $\beta$ -Ga<sub>2</sub>O<sub>3</sub>

A plausible reason for the observed Raman shifts could be due to inherent strain in the nanowires. Typically, compressive strains cause Raman peaks to upshift and tensile strains cause peaks to downshift. In our model, we hypothesize that the strains in the nanowires occur during their growth, and their magnitude is dependent on the nanowire growth direction. We have confirmed the hypothesis through a theoretical model using density functional theory (DFT) and are able to explain all Raman shifts for the gallium oxide nanowires reported in the literature.

The basic assumption of our model is the presence of non-negligible internal strains in the nanowires due to their large surface/volume ratio. Different growth directions will cause different surface reconstruction, and consequently lead to internal strains of different magnitudes and directions. As will be shown below, the calculated Raman frequency shifts suggests that the observed shifts in the nanowires with the  $[40\bar{1}]$  and  $[110]$  growth directions can be explained in term of different internal strains, in contrast to the previously suggested quantum confinement effects and defect induced effects.

The implementation of DFT adopted in this study is VASP (Vienna ab-initio simulation package). DFT techniques have been used for years to model various properties of materials such as the binding energy of molecules and the band structure of solids [48]. Modeling the electronic properties of a material (the so-called many body problem) is a very complicated computational process due to the fact that one needs to consider an infinitely large set of wavefunctions and the associated Schrödinger equations for a complete system. Density functional theory replaces this by the much easier to handle electron density. While DFT in principle gives a good description of ground state properties, practical applications of DFT are based on approximations for the so-called exchange-correlation potential. This potential accounts for the exchange interaction between electrons (due to the Pauli exclusion principle) and the electrostatic screening of each electron by the correlated motion of all the other electrons. One of the most common approximation methods is the local density approximation (LDA) which locally substitutes the exchange-correlation energy density of an inhomogeneous system by that of an electron gas evaluated at the local density. LDA is the method of choice for many computations such as the evaluation of lattice constants and bulk moduli. However, since the method is an approximation, other methods such as GGA (generalized gradient approximation) can be used. The LDA method fails in cases where the local electron density undergoes rapid changes. In such cases, the gradient of the electron density (GGA) can be applied.

However, for this study, local density approximation (LDA) was chosen for the many-electron exchange-correlation interaction and proved to be

sufficient, as shown by the calculated phonon frequencies in Table 1. Such calculations have been used extensively for describing the structural and vibrational properties of ceramic oxides, nitrides, and carbides [49]. The valence electrons (i.e.  $3d^{10}4s^24p^1$  electrons in Ga and  $2s^22p^4$  electrons in O) are treated explicitly in the electron eigenfunction calculations, while the core electrons are approximated with the Vanderbilt-type ultrasoft pseudopotentials (USPP) [50]. In DFT calculations, pseudopotentials replace the complicated effects of the motion of the core electrons of an atom or ion and its nucleus with an effective potential, or pseudopotential, so that the Schrödinger equation contains a modified potential term instead of the Coulombic potential term normally found in the Schrödinger equation. By construction of this pseudopotential, the valence wavefunction generated is also guaranteed to be orthogonal to all the core states.

The first step is to optimize the structures in order to achieve minimal energy (zero force) configuration. Then the zone-center phonon modes are derived from a direct force constant matrix calculation, which displaces atoms, one at each time, and determines the resultant force on each atom in the unit cell. All Raman frequency calculations of  $\beta$ -Ga<sub>2</sub>O<sub>3</sub> were carried out with a 10-atom base-centered monoclinic unit-cell model without the correction for the macroscopic interaction. Hence, both frequencies and eigenmodes are calculated with first-principle methods. The first principles calculation involves the integration of the electron wavefunction over the Brillouin zone of  $\beta$ -Ga<sub>2</sub>O<sub>3</sub>. In our model, the Brillouin zone was defined using a Monkhorst-Pack k-point grid. This method was developed by Monkhorst and Pack as a means of optimizing the

integration of periodic functions of a Bloch wavevector over a Brillouin zone [51]. Their derivation is based on the use of special points in  $k$ -space which generates an expansion of the periodic wavefunction with the proper symmetries. Hence one can effectively interpolate the wavefunction over the entire (or specific parts of) a Brillouin zone by integration over the wavefunctions at the special points. For our computation, we chose a  $6 \times 6 \times 6$  Monkhorst-Pack  $k$ -point grid. A plane wave energy cutoff of 397.5 eV was used in order to reduce the basis set to a finite size and make computations involving the Hamiltonian easier. Using the parameters mentioned above, our calculations predict equilibrium lattice parameters for bulk  $\beta$ -Ga<sub>2</sub>O<sub>3</sub> as  $a_0 = 12.11$  Å,  $b_0 = 3.005$  Å,  $c_0 = 5.731$  Å,  $\beta = 103.72^\circ$ , which are in close agreement with experimental data of  $a_0 = 12.23$  Å,  $b_0 = 3.04$  Å,  $c_0 = 5.8$  Å,  $\beta = 103.7^\circ$  [33].

The experimental Raman mode frequencies for bulk  $\beta$ -Ga<sub>2</sub>O<sub>3</sub> films whose Raman spectra are shown in Fig. 3.8 correspond well to those reported in the literature, as well as our LDA calculation. Also listed in the table are experimental and calculated Raman frequencies from Dohy *et al.* [31], who used a valence force field calculation to compute the vibrational modes of  $\beta$ -Ga<sub>2</sub>O<sub>3</sub>. In their calculation, the force constant matrix was set up using Cartesian coordinates, which were deduced from the X-ray data reported by Geller [33]. 50 atoms were taken into account in the calculation- those of the unit cell and their closest neighbors. In all, they used 29 distinct force constants (to account for various stretching, bending, and torsional modes) and calculated Cartesian displacements and potential energy distributions for every mode corresponding to the



experimental data. Our current mode symmetry assignment is purely based on the comparison between the observed and calculated Raman frequencies. As shown in Table 1 below, the theoretical data for bulk  $\beta$ -Ga<sub>2</sub>O<sub>3</sub> from our calculation matches well with 13 out of the 15 Raman active ( $10A_g + 5B_g$ ) modes observed in present study, as well as those of the previous study of Dohy *et al.* [31] In both cases of the unobserved Raman modes, there is another Raman-active mode in the close proximity. For example, our LDA calculations predicted two Raman modes at 469 and 474 cm<sup>-1</sup>, and two additional Raman modes at 601 and 624 cm<sup>-1</sup>. This suggests that it is possible that the two “missing” Raman modes in our LDA calculation are masked by the stronger adjacent Raman modes.

Direct first-principles calculations of phonon frequencies of strained 25 nm-diameter nanowires is a computationally challenging task as large super cell models (of at least tens of thousands of atoms) are needed. Instead, our study focused on providing a quantitative estimation of the internal strains which can account for the observed blue- and red-shifts in the Raman frequencies for [110] and  $[40\bar{1}]$   $\beta$ -Ga<sub>2</sub>O<sub>3</sub> nanowires, respectively. The internal strains of the nanowires were estimated based on the least squares fitting of the experimentally observed Raman frequency shifts with theoretically predicted linear strain coefficients  $d\omega/d\varepsilon_{ij}$ , where  $\omega$  and  $\varepsilon_{ij}$  are Raman frequencies and components of strain tensors, respectively. Furthermore, a quasi-harmonic approximation for the potential was used.

As mentioned in chapter 1, the harmonic approximation for the potential does not account for lattice expansion, and hence strains in a material. An

anharmonic potential including the cubic and/or higher terms in the potential series expansion must be included. However, computations involving anharmonic potentials are time consuming. Instead, the approach adopted in the present study was to perform calculations for different volumes which, in turn, correspond to different pressures. For each volume, a harmonic potential was used to calculate the phonon frequencies; however different volume gave us different phonon frequencies thus implying that phonon frequencies are dependent on volume.

The strain tensor of this monoclinic crystal has six independent elements,  $\epsilon_{11}$ ,  $\epsilon_{22}$ ,  $\epsilon_{33}$ ,  $\epsilon_{23}$ ,  $\epsilon_{13}$ , and  $\epsilon_{12}$ . For simplicity, the computation was restricted to linear effects, i.e.  $\omega(\epsilon) \approx \omega_0 + \sum (d\omega/d\epsilon_{ij} \times \epsilon_{ij})$ . This approximation is valid for small strains. Furthermore, the strain of  $\epsilon_{23}$  or  $\epsilon_{12}$  was neglected because their  $d\omega/d\epsilon_{ij}$  coefficients are zero due to the monoclinic lattice symmetry. For each of four remaining types of strains ( $\epsilon_{11}$ ,  $\epsilon_{22}$ ,  $\epsilon_{33}$ , and  $\epsilon_{13}$ ), the Raman frequencies were calculated for five finite strain values between -0.02 to +0.02. The calculated frequencies were then fitted with a polynomial function to obtain the linear strain coefficients. The results of the  $[40\bar{1}]$  and  $[110]$  nanowires are listed in Table 2, and the LDA model predicts the strain tensor for the  $[001]$  nanowires contain non-negligible  $\epsilon_{11}$ ,  $\epsilon_{22}$ ,  $\epsilon_{33}$ , and  $\epsilon_{13}$  components. As shown in Table 3, excellent fits were obtained overall for both the redshifted and blueshifted Raman spectra, with exceptions of the  $348 \text{ cm}^{-1} A_g$  mode in the  $[110]$  nanowire (our study) and the  $150 \text{ cm}^{-1} B_g$  mode in the  $[40\bar{1}]$  nanowire (Gao *et al.*). Our calculation shows that the  $[110]$  nanowire is compressed along its  $a$ - and  $c$ -axis, and stretched along its  $b$ -axis. The strain in the  $[40\bar{1}]$  nanowire exhibits a contrasting pattern and its strain

magnitude is only about 1/3 of that evaluated for the [110] nanowire. In both cases, the  $a$ -axis has the smallest change (Table 2). The strain induced volume changes are predicted to be -2% and 0.7% for the [110] and  $[40\bar{1}]$  nanowires respectively. Seo *et al.*[52] studied the internal strains of GaN nanowires using x-ray diffraction measurements and they reported the strains of  $\epsilon_{xx}= 2.3\%$ ,  $\epsilon_{yy}= -0.734\%$ , and  $\epsilon_{zz}= -0.4\%$  based on their experimental measurements. The magnitudes of predicted strains of  $\beta$ -Ga<sub>2</sub>O<sub>3</sub> in the present study are comparable to those of GaN nanowires.

Table 1: Comparison of calculated Raman mode frequencies with those measured in bulk  $\beta$ -Ga<sub>2</sub>O<sub>3</sub>.

Mode Symmetry	Dohy <i>et al.</i> [31]		This work	
	Force field Calculation (cm <sup>-1</sup> )	Expt. Data (cm <sup>-1</sup> )	LDA Calculated Frequency: (cm <sup>-1</sup> )	Expt. Data (cm <sup>-1</sup> )
A <sub>g</sub>	113	111	104	-
B <sub>g</sub>	114	114	113	-
B <sub>g</sub>	152	147	150	144
A <sub>g</sub>	166	169	166	169
A <sub>g</sub>	195	199	207	200
A <sub>g</sub>	308	318	317	317
A <sub>g</sub>	353	346	348	344
B <sub>g</sub>	360	353	356	-
A <sub>g</sub>	406	415	414	416
A <sub>g</sub>	468	475	469	472
B <sub>g</sub>	474		474	-
A <sub>g</sub>	628	628	601	628
B <sub>g</sub>	644	651	624	-
A <sub>g</sub>	654	657	635	654
A <sub>g</sub>	760	763	732	767

Table 2: Estimated internal strains.

Strain	[110] nanowire	$[40\bar{1}]$ nanowire
$\epsilon_{11}$	-0.0077	0.0029
$\epsilon_{22}$	0.0180	-0.0064
$\epsilon_{33}$	-0.0311	0.0106
$\epsilon_{13}$	0.0233	-0.0256
$\Delta V/V$	-0.0208	0.0071

## Conclusions

In summary, based on a comparison of the experimental Raman mode frequencies with our calculations, we find compelling evidence for growth direction- induced internal strains in  $\beta$ -Ga<sub>2</sub>O<sub>3</sub> nanowires which significantly influence the vibrational mode frequencies. Within the linear model approximation, the observed blue and red-shifts of peak frequencies in the micro-Raman spectra of the  $\beta$ -Ga<sub>2</sub>O<sub>3</sub> nanowires with different growth directions can be attributed to two small anisotropic internal strains: one compressive strain of 2% volume change, and the other tensile strain of 0.7% volume change. The overall high quality of the fitted models to available experimental data suggests a strong correlation between the shifts in Raman mode frequencies and the growth direction-induced internal strains in the  $\beta$ -Ga<sub>2</sub>O<sub>3</sub> nanowires.

Table 3: Raman mode frequencies and frequency shifts in  $\beta$ -Ga<sub>2</sub>O<sub>3</sub> nanowires with the  $[40\bar{1}]$  and  $[110]$  growth directions. Overall, excellent agreement between the observed and calculated shifts is seen for all mode frequencies except the two marked with an \*.

Gao <i>et al.</i> [9] [40 $\bar{1}$ ] growth direction				This work [110] growth direction			
Bulk (cm <sup>-1</sup> )	Nano-wire (cm <sup>-1</sup> )	Shifts $\Delta\omega$ (cm <sup>-1</sup> )	Calc. Shifts* (cm <sup>-1</sup> )	Bulk (cm <sup>-1</sup> )	Nanowire (cm <sup>-1</sup> )	Shifts $\Delta\omega$ (cm <sup>-1</sup> )	Calculated Shifts* (cm <sup>-1</sup> )
			-4.8				12.0
			1.7				-3.1
142	134	-8*	-1.0	144			3.8
167	160	-7	-7.2	169	180	+11	10.6
198	194	-4	-6.5	200	213	+13	13.5
320			-3.9	317			9.5
344	332	-12	-6.7	344			16.8
			-1.7				0.7
415	409	-6	-5.3	416	428	+12	12.3
473			-4.4	472	492	+20	21.1
			-6.2				18.5
627			-5.7	628	645	+16	17.8
			-0.3				3.6
651	641	-10	-14.8	654	697	+43	36.4
765	742	-23	-20.6	767	810	+43	47.0

\*These shifts were calculated using our LDA model [27]

## CHAPTER FOUR

### ANHARMONIC PHONON LIFETIMES IN CARBON NANOTUBES

#### Introduction

The study of elementary excitations in reduced-dimensionality systems has been one of the hallmarks of condensed matter physics for the past thirty years. Confinement to two, one, or zero dimensions induces profound changes in the electronic and vibrational structure of materials. Research on low-dimensional systems has also addressed the effect of dimensionality on the *interactions* between elementary excitations. Until now, these studies have focused on the electron-electron and electron-phonon interactions, but the anharmonic interaction between vibrational quanta (phonons) has received much less attention. The relative lack of work on anharmonic phonon-phonon interactions is understandable if one considers that the first accurate calculation of the anharmonic Raman scattering linewidth in simple bulk materials was published only a decade ago [53]. Moreover, anharmonic interactions often involve acoustic phonons (explained below), which are not as easy to confine as electrons and optical phonons. This state of affairs has changed dramatically with the development of spectroscopic techniques that probe individual semiconductor nanowires or carbon nanotubes.

Carbon nanotubes have proven to be a unique system for the study of Raman spectra in one-dimensional systems, and at the same time Raman spectroscopy has provided an exceedingly powerful tool for the characterization of single-walled carbon nanotubes (SWNTs). The unique optical and spectroscopic properties observed in single-wall carbon nanotubes are largely due to the one-dimensional (1D) confinement of electronic and phonon states, resulting in the so-called van Hove singularities in the nanotubes density of states (Fig. 4.1) [34, 54]. These singularities in the density of states, which are a result of the one-dimensional nature of the material, are of great relevance for a variety of optical phenomena. Whenever the energy of incident photons matches a van Hove singularity in the DOS of the valence and conduction bands (subject to selection rules for optical transitions), one expects to find resonant enhancement of the corresponding optical process. Owing to the diverging character of van Hove singularities in these 1D systems, such an enhancement can be extremely confined in energy (meV), appearing almost like transitions in a molecular system. In combination with the unique 1D electronic structure, the resonantly enhanced Raman scattering intensity allows one to obtain detailed information about the vibrational properties of nanotubes, even at the isolated individual SWNT level [55].



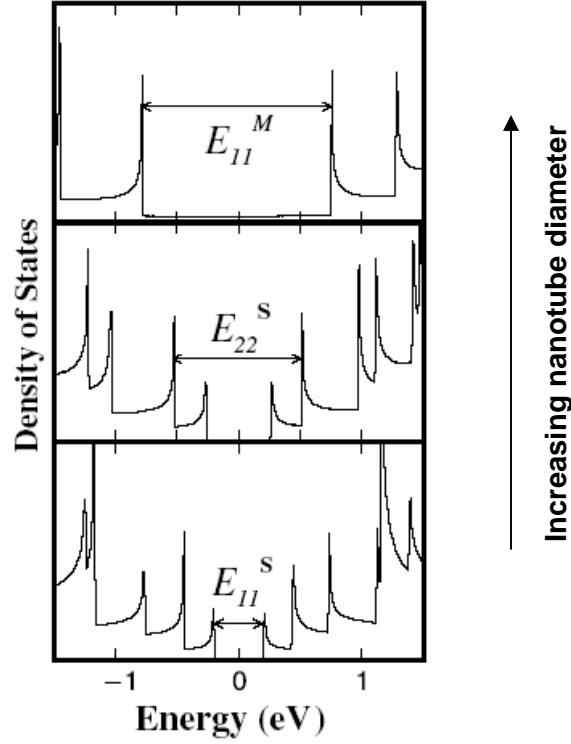


Figure 4.1: Calculated electron density of states for three different nanotubes. The van Hove singularity transitions are shown for both semiconducting (labeled S) and metallic nanotubes (labeled M) [56].

The outline for this chapter is as follows: The Raman modes of SWNTs will first be described along with the unique resonant Raman conditions satisfied by SWNTs. This is followed by a discussion on the Raman peak linewidths, and how it applies to carbon nanotubes, leading up to the motivation for the study described in this chapter. The rest of the chapter deals with nanotube synthesis and characterization, as well as room temperature, high-resolution micro-Raman measurements of suspended SWNTs which exhibit extremely low peak linewidths compared to what has been described in the literature. Finally, a model is

proposed to explain the unique anharmonic decay phenomenon that occurs in SWNTs.

### Raman scattering in carbon nanotubes

Individual single-walled carbon nanotubes are good candidates for Raman spectroscopy analysis because they follow a resonant scattering process, which occurs when the optical absorption (or emission) is to (or from) a real electronic state in the electron density of states (DOS). This is a general resonance phenomenon that occurs in the presence of an oscillating external field. In general, there are two resonance conditions for optical transition in the presence of an oscillating external field: (1) resonance with the incident laser photon (incidence resonance) and (2) resonance with the scattered photon (scattered resonance). When the resonance occurs with the incident photon, the incident laser light has the same energy ( $E_L$ ) as the energy separation between the two electronic states in resonance ( $\Delta E$ ), while the scattered photon has an additional energy of the phonon  $\hbar\omega$ . Therefore,  $E_L = \Delta E$  (incident resonance in the former case) ,  $E_L = \Delta E + \hbar\omega$  (scattered resonance in the latter case). The resonance Raman process increases the signal by a factor of approximately  $10^3$  in comparison to the intensity for a non-resonance Raman process. In the case of SWNTs, not only resonant enhancement but also a singularity in the DOS contributes to the Raman intensity (Fig. 4.1). When the laser energy of either the incident or the scattered light has the same energy as a vHS energy in the DOS (for example, see  $E_{11}$ ,  $E_{22}$ , and  $E_{33}$  in Fig. 4.1), the Raman intensity becomes

extremely strong for any SWNT that satisfies the resonance condition. This is the reason why we can get a measurable signal from a single isolated SWNT in the presence of many non-resonant SWNTs [57].

The Raman spectrum of a single-walled nanotube contains two main features: the radial breathing mode, and the G-band. The radial breathing mode (RBM) corresponds to the coherent vibration of the carbon atoms in the radial direction, as if the tube were “breathing” (Fig. 4.2). The symmetry label for the breathing mode is  $A_{1g}$ . These modes are unique to carbon nanotubes and occur with frequencies  $\omega_{\text{RBM}}$  between 120 and 350  $\text{cm}^{-1}$  for SWNTs for diameters in the range  $0.7\text{nm} < d_t < 2 \text{ nm}$ . The RBM is also unique in the sense that it follows an inverse relationship with the nanotube diameter. For isolated SWNTs, the relation between the RBM peak frequency and the tube diameter is given by [55]

$$\omega_{\text{RBM}} \cong \frac{248}{d_t} \quad (4.1)$$

The above formula is empirical, and can be applied to determine the approximate diameter of a single-walled nanotube. In their STM study, LeRoy *et al.* [11] analyzed various semiconducting and metallic nanotubes, and found an inverse relationship between the energy of the phonon-assisted tunneling peak and the nanotube diameter. In terms of energy, eq. 4.1 can be written as  $E_{\text{RBM}} = 27.8/d_t$  meV, [58] where  $E_{\text{RBM}}$  is the energy of the RBM phonon. The experimental value of  $28.1/d_t$  from their study agrees very well with theoretical predictions, and

provides further proof for the excitation of RBM phonons via electrons in the tunneling study.

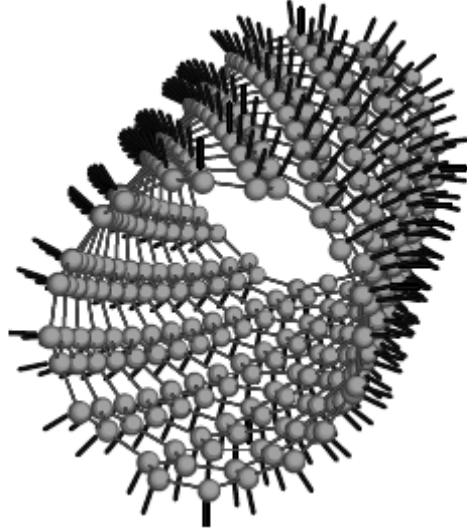


Figure 4.2: Simulation of the radial breathing mode vibrations of a 0.8 nm diameter single-walled nanotube. The vertical lines over each carbon atom indicate the radial motion of the atoms [59].

Bulk graphite has a single Raman active mode at  $1582\text{ cm}^{-1}$ . The scattering phonon is of  $E_{2g}$  symmetry with an in-plane optical eigenvector, i.e., the two carbon atoms in the hexagonal unit cell move out of phase within the graphite planes. Similar vibrations also give rise to the high-energy spectra in nanotubes, but additionally the confinement around the circumference and the curvature of the graphene (single layer of graphite) sheet must be taken into account. Due to curvature effects, the SWNT *G*-band is composed of several peaks arising from phonon wavevector confinement along the SWNT circumferential direction and due to symmetry-breaking effects associated with SWNT curvature. Fig. 4.3 shows some of the eigenvectors for vibrational modes along the tangential direction for a SWNT. The *G*-band frequency can be used for (1) to distinguish

between metallic and semiconducting SWNTs, through strong differences in their Raman lineshapes [60]; (2) to probe the charge transfer arising from doping a SWNT; and (3) to study the selection rules in the various Raman scattering processes and scattering geometries.

The *G*-band feature for SWNTs consists of two main components, one peaked at  $\sim 1590\text{ cm}^{-1}$  (*G*<sup>+</sup>) and the other peaked at  $\sim 1570\text{ cm}^{-1}$  (*G*<sup>−</sup>). The *G*<sup>+</sup> feature is associated with carbon atom vibrations along the nanotube axis (LO phonon mode) and its frequency is sensitive to charge transfer from dopant additions to SWNTs [61]. The *G*<sup>−</sup> feature, in contrast, is associated with vibrations of carbon atoms along the circumferential direction of the SWNT (TO phonon), and its lineshape is highly sensitive to whether the SWNT is metallic (Breit–Wigner–Fano lineshape) or semiconducting (Lorentzian lineshape) [62]. Charge transfer to SWNTs can lead to an intensity increase or decrease of the BWF feature [63]. The *G* band is also dependent on the nanotube diameter, although being a more complicated high frequency vibration, this dependence is not as strong as the RBM.

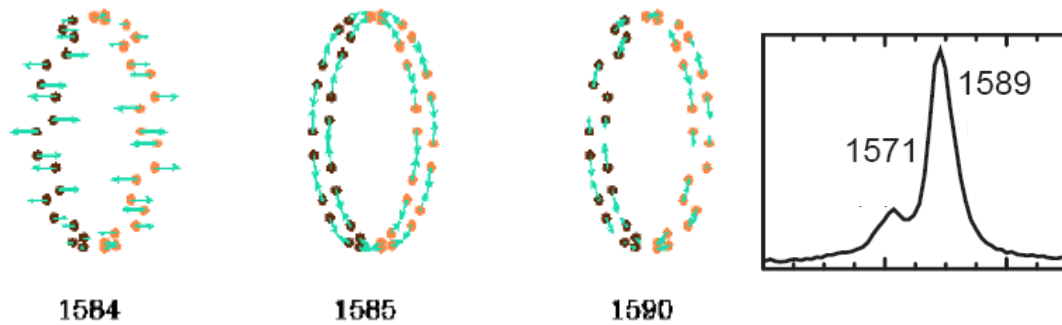


Figure 4.3: Raman-active normal eigenvectors and frequencies for the tangential  $G$  band of a single-walled carbon nanotubes. The arrows indicate the direction of the carbon atom displacements in a unit cell for a (10,10) SWNT. A typical  $G$  band showing the  $G^+$  and  $G^-$  peaks is shown on the right.

### Phonon decay and lifetime

Chapter 1 outlined some of the reasons for the failure of the harmonic approximation for describing the crystal potential. In a real crystal, phonons do not propagate infinitely but interact with each other and decay into other phonons with lower energies. In a Raman scattering process, optical phonons are created as a result of scattering of light by the sample. Due to anharmonicity of lattice forces, these phonons have finite lifetimes and decay into other phonons thereby attaining thermal equilibrium. The reason to study phonon lifetimes in materials is because finite phonon lifetimes play an important role in the thermal conductance of a material. Hence the knowledge of phonon lifetimes within a material could be useful in tailoring the thermal properties of materials, and this is especially applicable in the field of nanotechnology, and carbon nanotubes in particular [64].

One of the first models applied to phonon decay in a Raman process was put forward by Klemens [5]. According to his model, the principal anharmonic

interaction is due to the cubic term in the phonon potential (see eq. 1.1), resulting in a splitting of an optical phonon into two acoustic phonons having equal energy but opposite momentum. Klemens' method has been used to explain thermal conductivity in a variety of materials [65]. Based on perturbation theory, Klemens formulated a simple mechanism which involves the linewidth of a Raman peak. The Raman peak width, or the *linewidth*, is directly related to the phonon lifetime. Since the Raman peak is plotted as intensity versus wavenumber (or energy) the width of a peak is related to the lifetime through the energy-time uncertainty principle:

$$\Delta E \Delta t \geq \frac{\hbar}{2} \quad (4.2)$$

In the above expression,  $\Delta E$ , the uncertainty in energy corresponds to the linewidth of the Raman peak, and the uncertainty in time,  $\Delta t$  is taken as the lifetime  $\tau$  of the phonon. In other words, the formula can be re-written as

$$\Gamma \tau \geq \frac{\hbar}{2} \quad (4.3)$$

Thus according to the above formula,  $1 \text{ cm}^{-1} = 5.3 \text{ ps}$ . Using time-dependent perturbation theory, Klemens derived an expression for the temperature dependent anharmonic linewidth of a Raman peak. His theory predicts the linewidth of a Raman mode at frequency  $\omega_0$  to be

$$\Gamma(T) = \Gamma_0 (1 + n_1 + n_2) \quad \text{and} \quad n_1 = n_2 = \frac{1}{\exp\left(\frac{\hbar\omega}{k_b T}\right) - 1} \quad (4.4)$$

where  $\Gamma(T)$  is the temperature-dependent linewidth of the Raman mode,  $\Gamma_0$  is related to the square of the anharmonic interaction matrix elements,  $n_1$  and  $n_2$  are the Bose-Einstein phonon occupation numbers, and  $\omega = \omega_0/2$ . Another aspect of the Klemens decay mechanism is that the final decay products, namely the acoustic phonons belong to the same branch in the phonon dispersion of the material, i.e., an optical phonon decays into either two transverse acoustic (TA) or two longitudinal acoustic (LA) phonons. Of course, the Klemens model is the most basic model that can be applied to phonon decay and not all phonon modes follow this mechanism. Other researchers have modeled phonon decay according to multiple phonon processes, who found out that the Klemens decay mechanism is not applicable for materials such as GaP, GaAs, Ge and Si [53, 66]. In these systems, an optical phonon decays into acoustic phonons belonging to different branches.

Very few studies have focused on the linewidth of Raman features in carbon nanotubes. The earliest Raman study was on SWNT bundles by Iliev *et al.* [67], in which they found the lowest room temperature linewidth in the RBM to be above  $6 \text{ cm}^{-1}$ . They did perform a study on the temperature dependence of the RBM linewidth and found that the width is indeed a function of temperature as can be seen in Fig. 4.4 below. In the figure, the RBM band centered at  $167 \text{ cm}^{-1}$  was fitted with 4 Lorentzian functions and plotted separately as a function of



temperature. Jorio *et al.* [68] analyzed the RBM of several isolated SWNTs on silicon substrates and found lower linewidths than what had been reported for bundled SWNTs. The lowest linewidth found in their study was  $\sim 3 \text{ cm}^{-1}$  (Fig. 4.5), which is still higher than the linewidth expected for individual single-walled carbon nanotubes.

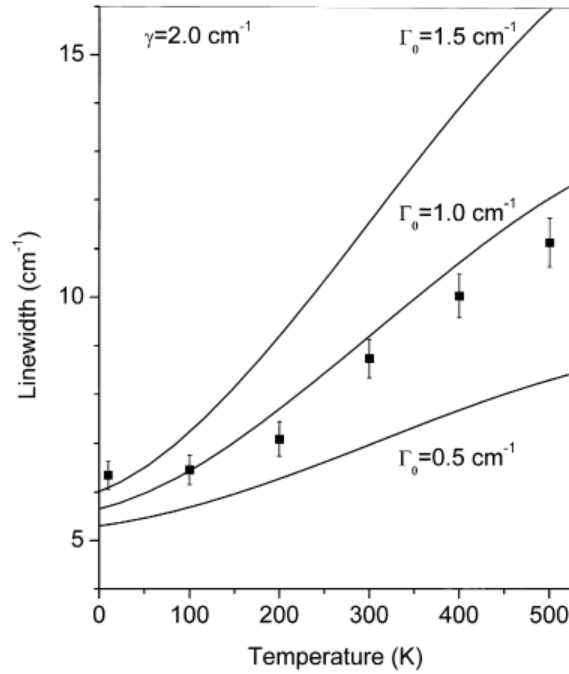


Figure 4.4: Experimental points and calculated curves showing the temperature dependence of the linewidth of the  $167 \text{ cm}^{-1}$  band for a SWNT bundle. The band is simulated as consisting of four close-lying Lorentzian components with  $\Gamma_0 = 0.5, 1.0,$  and  $1.5 \text{ cm}^{-1}$  [67].

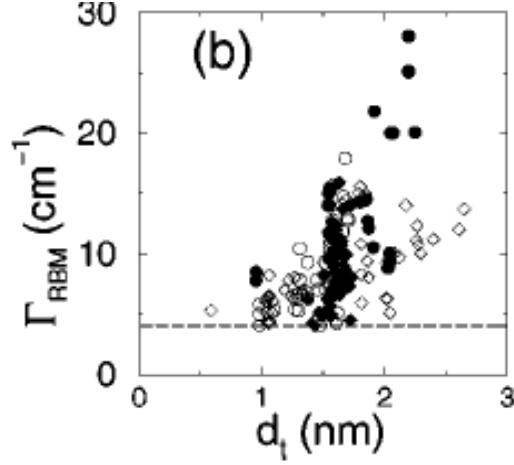


Figure 4.5: Linewidth of the RBM ( $\Gamma_{\text{RBM}}$ ) vs nanotube diameter ( $d_t$ ) for 81 metallic (solid symbols) and 89 semiconducting (open symbols) isolated SWNTs [68].

Over the last few years, researchers have been focusing on the growth and characterization of isolated, or individual SWNTs [69]. Nanotubes have a strong tendency to form bundles because of strong attractive Van der Waals forces between them. The bundles are not very useful for practical applications, and one has to find various methods to de-bundle the SWNTs. O’Connell described one such method which involved the centrifugation of nanotube bundles with a surfactant [70]. The surfactant aids in breaking up the bundle but at the same time forms a micelle-like coating the nanotubes. Hence, these surfactant-coated nanotubes might not be very useful for practical device-oriented applications. Another approach is to grow individual SWNTs directly on substrates, which could be then be directly used for devices such as field effect transistors, gas sensors, [71, 72]. However, due to the tube-substrate interaction, the intrinsic properties of the SWNTs could be modified in an undesirable fashion. For example, optical characterization of the intrinsic properties of these individual

nanotubes is not possible due to the tube-substrate interactions. More recently, researchers have begun focusing their attention to nanotubes suspended over trenches or pillars so that the intrinsic properties of the nanotubes can be probed and understood. Huang *et al.* [69] first reported the synthesis of long individual SWNTs over trenches in silicon substrates using their “rapid heating” chemical vapor deposition method. Other researchers have used lithographic methods to etch away pillars in silicon trenches. They then deposit catalyst particles on top of the pillars and have managed to grow single-walled nanotubes between the pillars as shown in Fig. 4.6 below [73, 74]. In addition to optical characterization, gas and fluid adsorption studies [75] as well as use in electronic and nanoelectromechanical (NEMS) experiments [76, 77] can be performed on the suspended nanotubes without worrying about nanotube-substrate interactions.

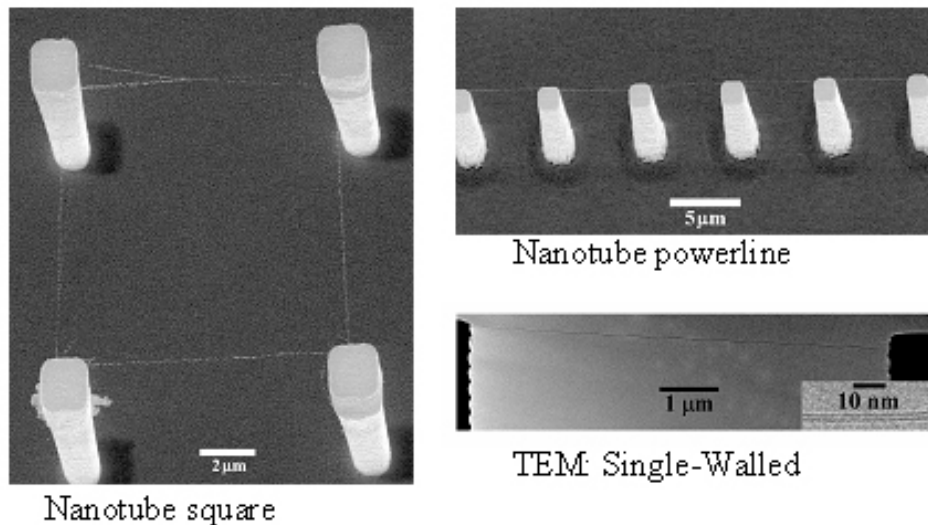


Figure 4.6: Individual single-walled nanotubes grown between pre-fabricated pillars on silicon substrates [73].

Raman spectra of the suspended SWNTs show enhanced intensities. Kobayashi *et al.* [78] grew individual SWNTs between pillars as well as over the flat regions of silicon substrates and noticed a large increase in intensity of the Raman spectrum of the suspended SWNTs compared to the nanotubes on the substrates. The suspended SWNTs showed an increase in the RBM, G band, and D band intensities. In addition to the increased intensities, linewidth narrowing has also been observed in the suspended SWNTs. Son *et al.* reported radial breathing mode linewidths of  $3.5 \text{ cm}^{-1}$  (Fig. 4.7) for suspended nanotubes as opposed to  $> 5 \text{ cm}^{-1}$  for nanotubes on substrates. Nanotubes are bound to substrates via Van der Waals forces, which causes greater broadening of the Raman peaks compared to suspended SWNTs. The linewidth value reported by Son *et al.* for a suspended SWNT, though less than the value reported for isolated SWNTs on a substrate, is still not as low as the linewidth values reported by *et al.* [11] in their STM study.

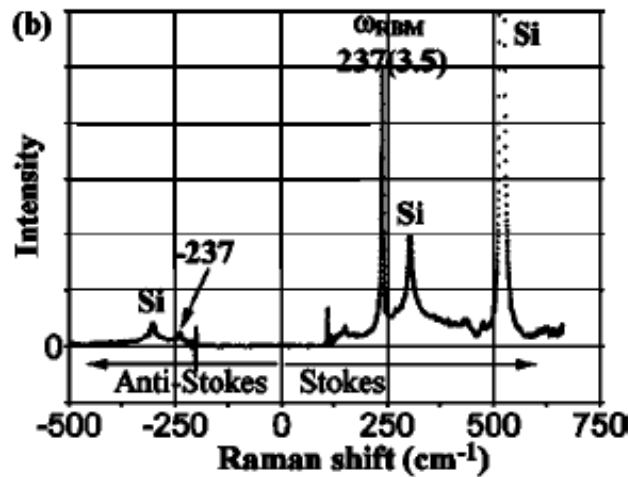


Figure 4.7: Stokes and anti-Stokes Raman spectra from an individual suspended SWNT on a silicon substrate with  $\omega_{\text{RBM}}$  at  $237 \text{ cm}^{-1}$  [79].

The above discussion points to the inherent instrumental broadening being a big factor in the observed linewidths for both nanotubes on substrates and suspended nanotubes. Jorio *et al.* [68] used a Raman instrument with a highest resolution of  $2\text{ cm}^{-1}$ , which is common in most Raman spectrometers. Moreover, the Raman spectra are typically fitted to Lorentzian functions, without deconvoluting the Gaussian instrumental function (described below). Hence this instrumental line broadening in standard Raman instrumentation makes it impossible to measure intrinsic linewidths of  $10^{-4}\text{ cm}^{-1}$  as was reported by LeRoy *et al.* in their STM study and described in chapter 1 [11]. It must be noted that the long lifetimes corresponding to narrow linewidths are easy to measure in the time domain, and recent experiments detecting the coherent vibrations of RBM modes in micelle-encapsulated SWNTs are consistent with a Raman FWHM of  $3\text{ cm}^{-1}$  [80]. Therefore, the discrepancy of more than three-orders of magnitude between the tunneling and optical experiments is real, and suggests that the standard theoretical framework for analyzing anharmonic processes needs revision in the case of one dimensional carbon nanotubes.

### Nanotube Synthesis

Suspended SWNTs were prepared via a chemical vapor deposition (CVD) method (shown schematically in Fig. 4.8) on etched silicon substrates. Trenches measuring  $5\text{ }\mu\text{m}$  wide,  $10\text{ }\mu\text{m}$  in length and  $3\text{-}5\text{ }\mu\text{m}$  in depth were etched in silicon substrates using focused ion beam microscopy. Individual suspended SWNTs were then grown across these trenches using the “rapid-heating” method [81].

Briefly, the silicon substrates with etched trenches were dipped into a solution containing ~1mg of iron nitrate dissolved in 10-50 ml of ethanol, followed by baking in an oven at 200 °C. The substrates were placed outside the hot zone of the CVD stabilized at 900 °C under a constant flow of argon (~400 sccm) and hydrogen (~100 sccm). Then CO gas (50-150 sccm) was introduced and the substrates were quickly moved into the central hot zone of the reactor. Typical run times were 15 minutes. After the reaction, the silicon substrates were removed carefully and characterized via electron microscopy (SEM) and Raman spectroscopy.

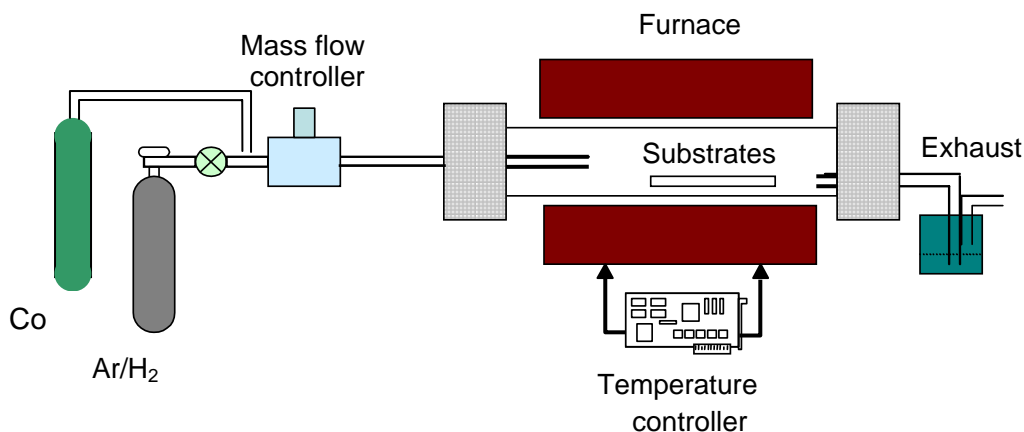


Figure 4.8: Schematic of the chemical vapor deposition method used to synthesize suspended SWNTs.

### Electron Microscopy of Suspended SWNTs

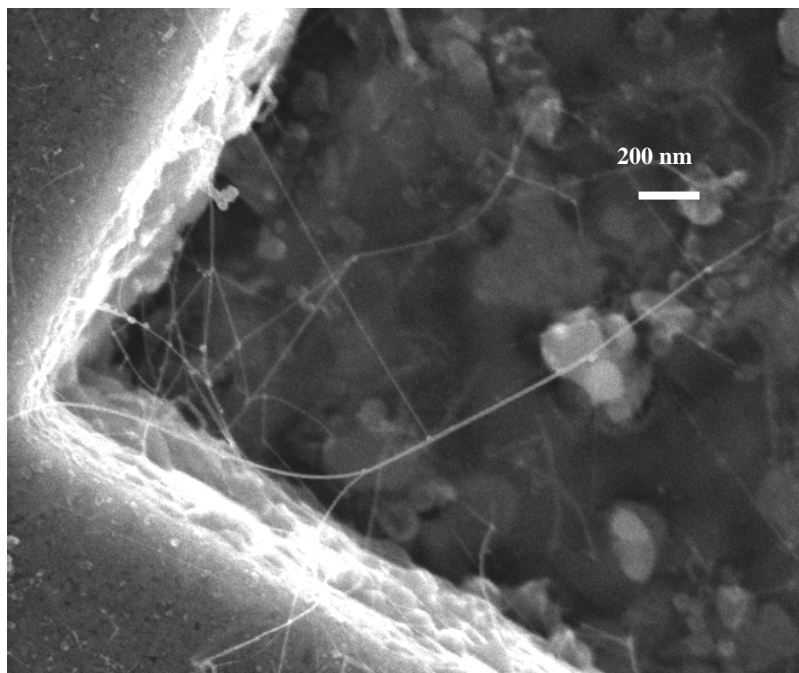


Figure 4.9: SEM image showing several suspended SWNTs across the corners of a trench etched into the silicon substrate. The clusters appearing at the bottom of the trench are catalyst particles and do not interfere with the Raman spectra since they do not lie in the focal plane of the focus beam of the exciting laser.

Several suspended SWNTs crossing over the corner of a trench in the Si substrate is shown in Fig. 4.9. The clusters appearing at the bottom of the trench in Fig. 4.9 did not affect the Raman spectra due to the 3-5  $\mu\text{m}$  depth of the trench. For the Raman study, electron microscopy study was essential for two reasons: (1) to confirm successful synthesis of suspended SWNTs, and, (2) to identify regions in the substrates that contained either single or multiple SWNTs. Subsequent Raman analysis (described below) also proved the existence of many nanotubes within the trench. Maps of trenches were made and regions containing

individual nanotubes within the area of the Raman-microscope spot ( $\sim 2 \mu\text{m}$  diameter) were identified for Raman analysis.

### Raman Analysis of the Suspended SWNTs

Room temperature micro-Raman spectra were obtained from individual SWNTs using the 647.1 nm line of a Kr ion laser. Suspended SWNTs were focused with a 50 $\times$  objective and back-scattered spectra were collected using the TRIAX 550 spectrometer equipped with a liquid nitrogen CCD described in chapter 2. The 647.1 nm excitation was chosen because it offers a higher resolution compared to lower wavelengths. A spectral resolution of below  $1 \text{ cm}^{-1}$  was achieved with a slit size of  $50 \mu\text{m}$  and a 2400 grooves/mm diffraction grating. After data collection, all spectra were fitted to Lorentzian and Voigt functions to get the exact values of peak position and linewidth. Spectral lines can be characterized by a mathematical function called the Lorentzian function. This function is widely used for fitting peaks that arise due to electromagnetic scattering in processes such as x-ray, Raman and infrared scattering. The Lorentzian function is defined as follows:

$$I(\omega) = \frac{A}{(\omega - \omega_0)^2 + \Gamma^2} \quad (4.5)$$

where A is the amplitude,  $\Gamma$  is the half width at half maximum of the peak, and  $\omega_0$  is the peak position. The linewidth, or full width at half maximum (FWHM), is



therefore,  $2\Gamma$ . High resolution linewidth measurements are typically tough to measure experimentally. The instrumental resolution determines the limit to which one can measure the Lorentzian linewidth of a Raman peak. The laser excitation source emits light that has a Gaussian distribution of energies. The experimentally measured Raman peak is a convolution of the intrinsic Lorentzian lineshape and the Gaussian and hence the true Lorentzian linewidth can be determined by deconvoluting the experimental peak. This can be done by using a Voigt lineshape, which is a superposition of a Lorentzian and a Gaussian function [82, 83]. The Gaussian spectral resolution can be reduced by controlling the spectrometer slit width but at the cost of reduced intensity of scattered radiation. In this study, slit widths of 5-10  $\mu\text{m}$  yielded the highest resolution (better than 1  $\text{cm}^{-1}$ ). All spectra were also plotted and fitted with Lorentzian and Voigt functions using the plotting software IGOR Pro. Following each set of experiments, the laser line was fitted to a Gaussian function first in order to get the Gaussian linewidth. This value was used for the Voigt fit to obtain the Lorentzian linewidth of the RBM modes.

Figure 4.10 shows representative Raman spectra collected from individual semiconducting (left) and metallic (right) SWNTs. Both spectra have been fitted with Voigt lineshapes (solid lines) and have been plotted over the raw data (open circles). The Lorentzian linewidths are listed in brackets next to the labels for peak positions. In general, among the various suspended SWNTs measured in our study, the linewidths were found to be about 3 times smaller than any of the previously reported values. In addition, the narrow lineshape of the peaks

indicates that these nanotubes are individual SWNTs rather than bundles, consistent with our electron microscopy study. Raman spectra were also collected from regions on the trenches that contained multiple individual SWNTs within the Raman spot. As can be seen in Fig. 4.11, there are three distinct peaks centered at  $196\text{ cm}^{-1}$ ,  $250\text{ cm}^{-1}$ , and  $303\text{ cm}^{-1}$ . The peak  $250\text{ cm}^{-1}$  appears to be a lot sharper and narrower than the other two peaks indicating that the SWNT whose RBM corresponds to  $250\text{ cm}^{-1}$  is strongly in resonance with the excitation energy. The  $250\text{ cm}^{-1}$  peak also appears to have a broad tail on the low frequency side, which is indicative of the presence of other SWNTs adjacent to the one which exhibits the  $150\text{ cm}^{-1}$  peak.

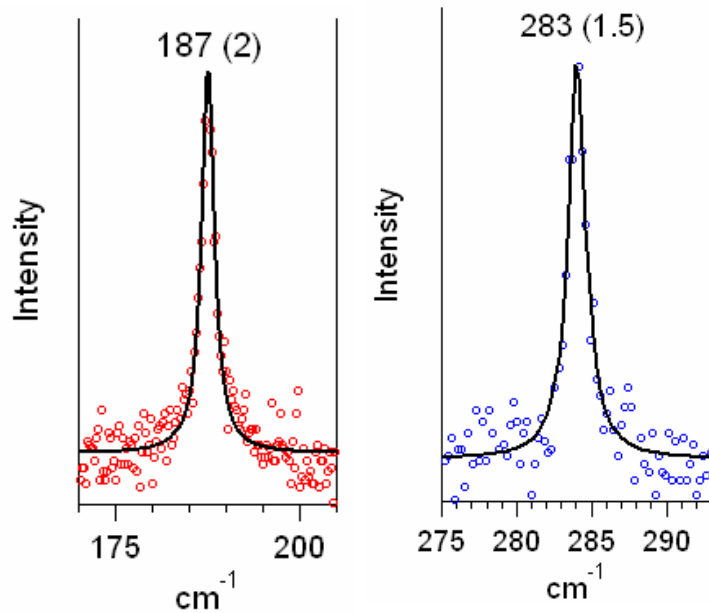


Figure 4.10: Micro-Raman spectra from an individual suspended semiconducting SWNT (left) and a metallic SWNT (right). The peak position (linewidth) are indicated in the graphs.

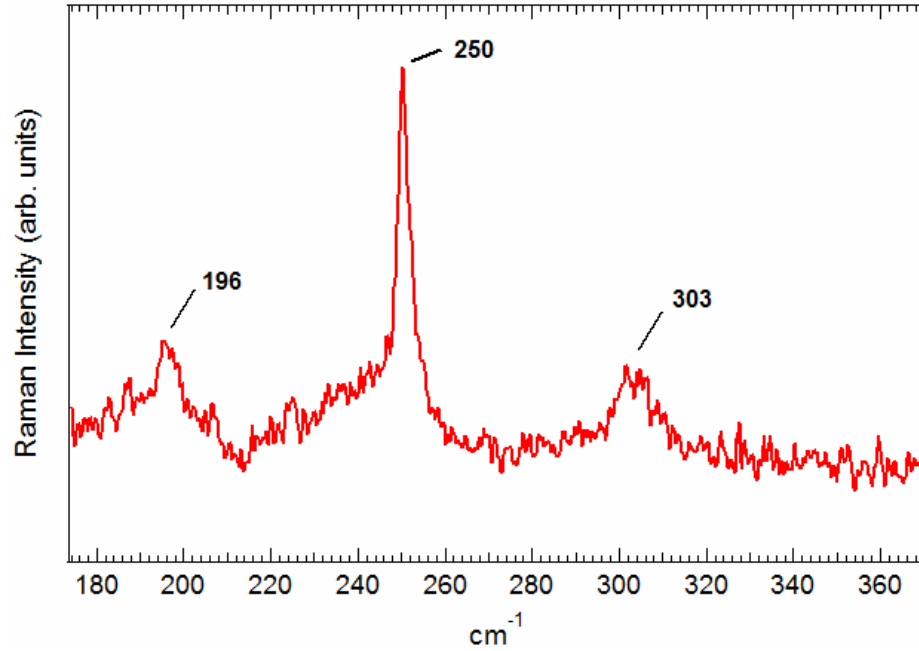


Figure 4.11: Micro-Raman spectra in the RBM range from a region on a trench containing multiple suspended SWNTs.

The reason why the two nanotubes shown in Fig. 4.10 can be identified as semiconducting or metallic is due to the unique lineshape of their tangential  $G$  bands. As can be seen in Fig. 4.12, the  $G$  band from a semiconducting SWNT (top trace) whose RBM appears at  $216\text{ cm}^{-1}$  is centered at  $1591\text{ cm}^{-1}$  ( $G^+$  peak) and the  $G^-$  peak can be seen as a shoulder at  $\sim 1570\text{ cm}^{-1}$ . The lineshape of the  $G$  band for a metallic nanotube whose RBM appears at  $283\text{ cm}^{-1}$ , on the other hand does not follow a Lorentzian lineshape. Due to electron-phonon coupling, the  $G^-$  peak in metallic nanotubes increases in intensity, and changes from a Lorentzian to a Breit-Wigner-Fano (BWF) lineshape [62, 84]. The mode at  $\sim 1590\text{ cm}^{-1}$  ( $G^+$  band) still remains Lorentzian. The fact that both semiconducting and metallic nanotubes could be analyzed in this study can be seen from the “Kataura plot” shown in Fig. 4.13. Such a graph was first described by Kataura *et al.*, [85] who

measured Raman spectra from various nanotubes at various laser excitation wavelengths and plotted the nanotube diameter against the laser energy. The data follows bands which are due to optical transitions between the van Hove singularities in metallic and semiconducting nanotubes (c.f. Fig. 4.1). As an example, RBM modes ranging from  $120 \text{ cm}^{-1}$  ( $d_t = 2.06 \text{ nm}$ ) to  $296 \text{ cm}^{-1}$  ( $d_t = 0.83 \text{ nm}$ ) were observed and are plotted as vertical lines in Fig. 4.13. Also, the  $E_{11}$  and  $E_{22}$  transition bands for semiconducting (labeled S) and metallic nanotubes (labeled M) are indicated in the figure in addition to a horizontal line corresponding to the 647.1 nm laser excitation. As can be seen from the figure, the horizontal laser excitation line intersects the  $E_{22}$  and  $E_{33}$  semiconducting transition band and the  $E_{11}$  metallic transition band implying that both semiconducting and metallic nanotubes can resonantly couple to the 647.1 nm Raman excitation energy.

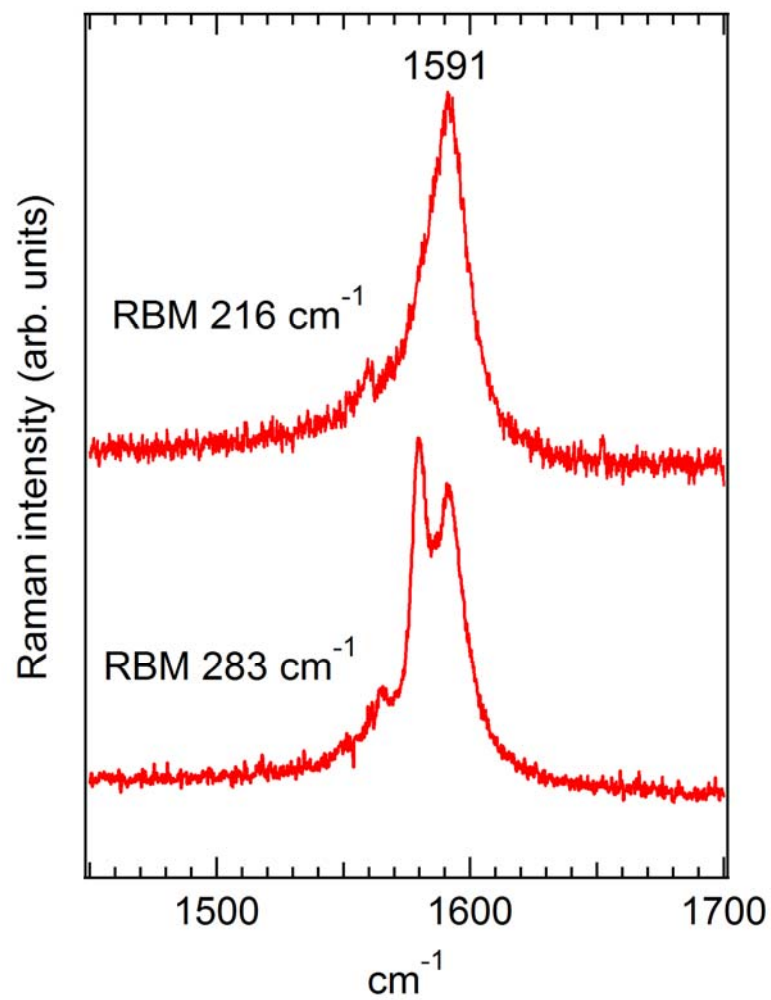


Figure 4.12: The tangential bands for a semiconducting (top) and a metallic (bottom) suspended SWNT.

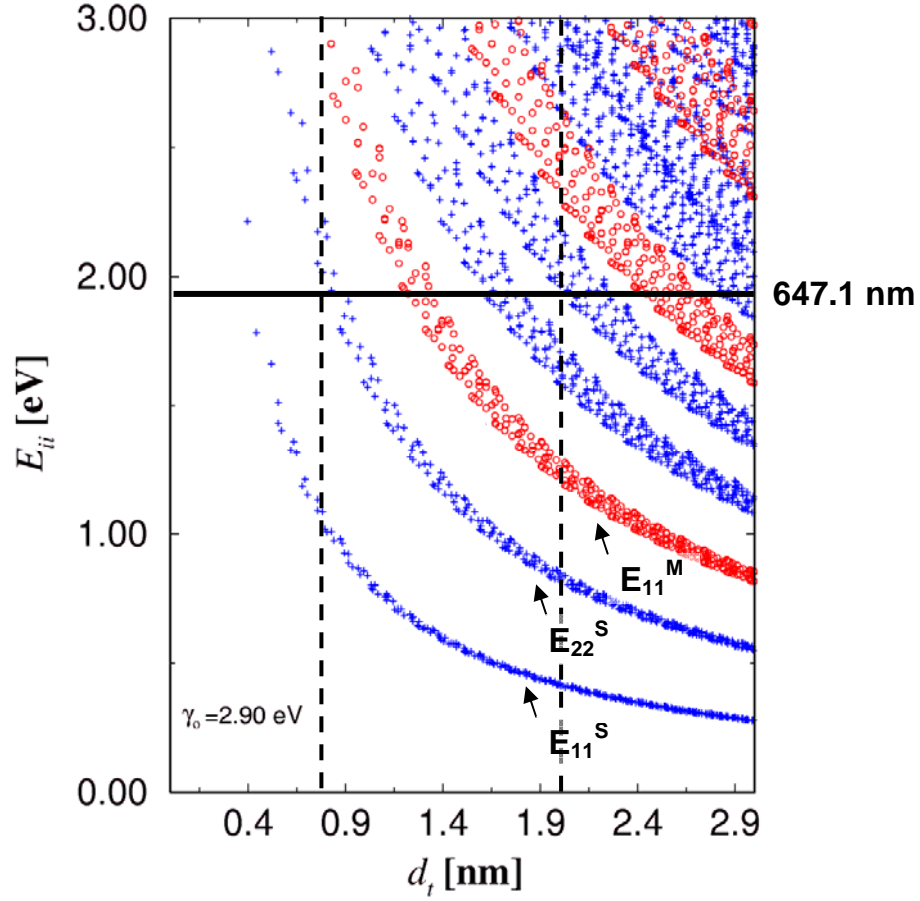


Figure 4.13: Kataura plot between nanotube diameter and incident laser excitation energy ( $E_L$ ). The vertical lines indicate the diameter distribution of the suspended SWNTs analyzed in the present study.

Fig. 4.14 shows a plot of the Lorentzian linewidth of the radial breathing mode against RBM peak frequency for several semiconducting and metallic SWNTs. As can be seen from the figure, most of the SWNT linewidths lie below  $2 \text{ cm}^{-1}$ , which is less than the values reported in the literature. No clear relationship between linewidth and diameter can be seen from the plot, whereas Jorio *et al.* reported an increase in linewidth with tube diameter (see Fig. 4.5). The reason could be the fewer number of suspended SWNTs analyzed in the present study.

Furthermore, no difference was found between the RBM linewidth values of metallic and semiconducting nanotubes and the SWNT diameter.

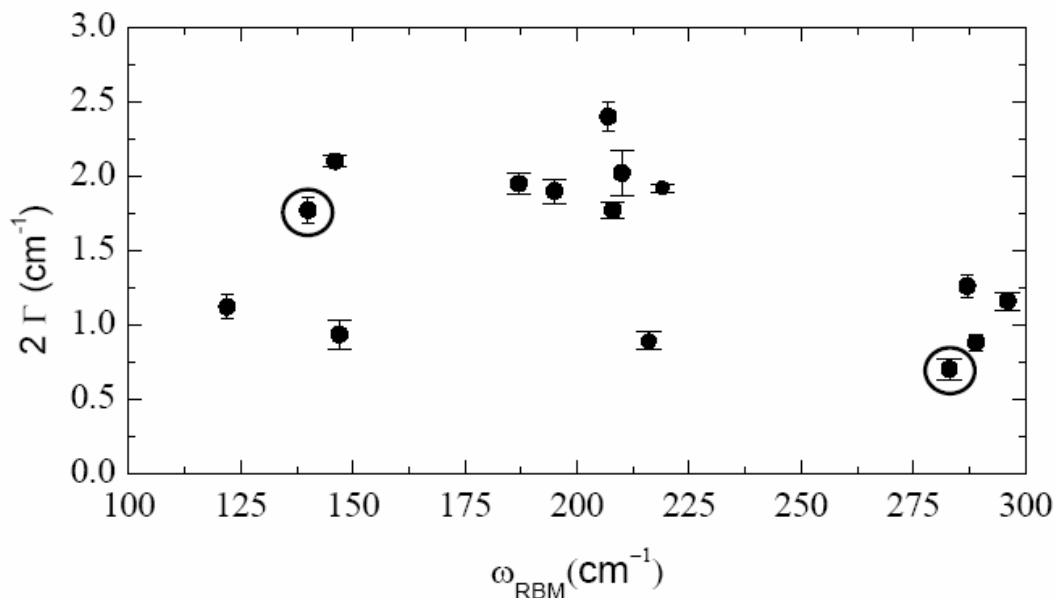


Figure 4.14: Deconvoluted  $2\Gamma$  (Lorentzian FWHM) values for several suspended SWNTs plotted versus  $\omega_{\text{RBM}}$ . The circled data points represent metallic SWNTs while the rest are semiconducting SWNTs. Error bars from the linewidth fit are also plotted.

The smallest linewidth measured in the present study is  $0.7 \text{ cm}^{-1}$  (c.f. eq. 4.3), which still corresponds to a picosecond phonon lifetime. Hence, due to the remaining large discrepancy in the phonon lifetimes determined from tunneling [11] and Raman studies, it is important to ascertain to what extent the experimental linewidths are intrinsic. As discussed in the Klemens model, the main contribution to the intrinsic anharmonic broadening of optical phonons is usually a down-conversion decay process of the form [86]

$$\Gamma(T) = \sum_{k\sigma\sigma'} \Gamma_{k\sigma\sigma'} \left[ 1 + n(\omega_{k\sigma}) + n(\omega_{-k\sigma'}) \right] \delta(\omega_{\text{RBM}} - \omega_{k\sigma} - \omega_{-k\sigma'}) \quad (4.6)$$

This mechanism involves the decay of the RBM mode of frequency  $\omega_{\text{RBM}}$  into pairs of phonons  $(\omega_{k\sigma}, \omega_{-k\sigma'})$  from branches  $\sigma$  and  $\sigma'$  that satisfy the energy and crystal momentum conservation rules. The functions  $n(\omega)$  are the standard Bose-Einstein thermal occupation factors (c.f., eq. 4.4), and the coefficients  $\Gamma_{k\sigma\sigma'}$  are proportional to the square of the anharmonic interaction matrix elements. The presence of a delta function in eq. (4.6) implies that the linewidth is extremely sensitive to the details of the phonon DOS whenever this density is highly structured, as in the case of SWNTs (Fig. 4.15). Thus there may now be a smooth dependence of the linewidths on diameter (or equivalently, on the RBM frequency), and Fig 4.14 is consistent with this analysis.

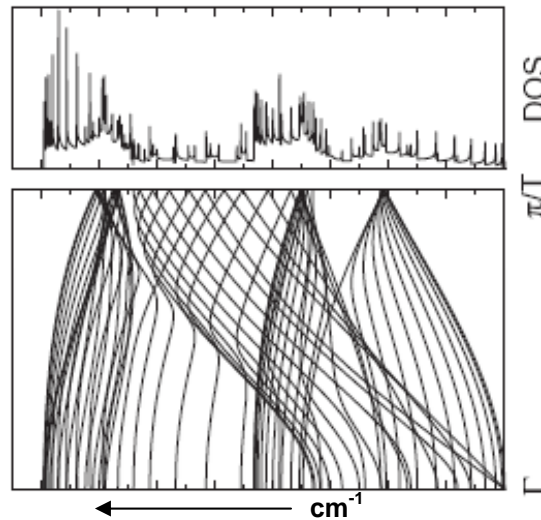


Figure 4.15: The calculated phonon dispersion relations of a carbon nanotube (bottom), and the corresponding phonon density of states (top).



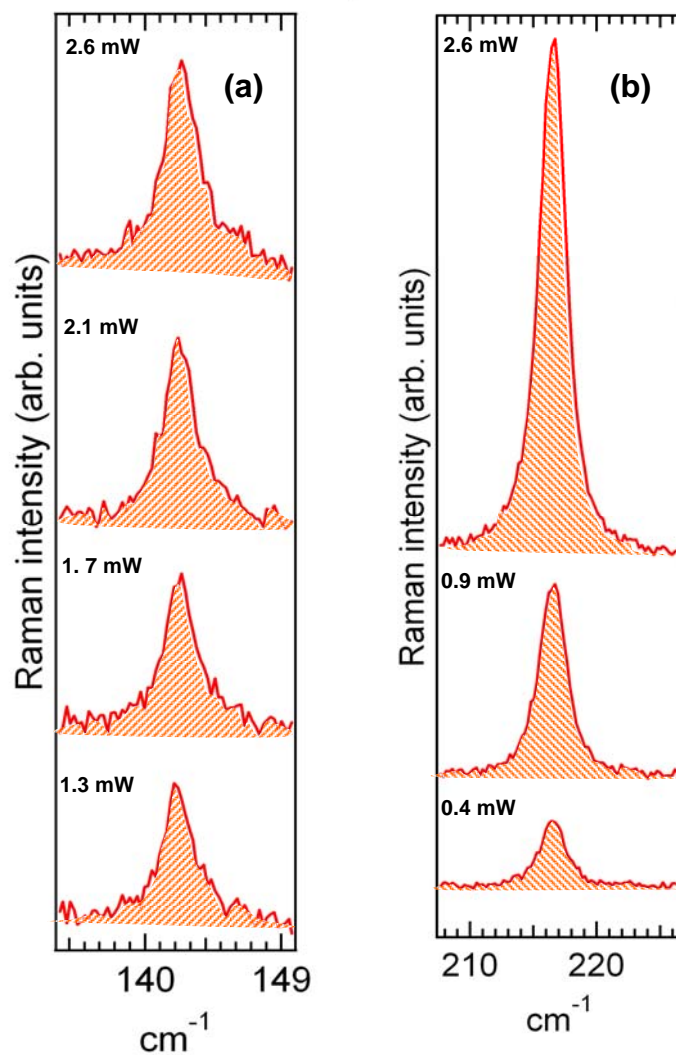


Figure 4.16: Raman spectra around the radial breathing mode frequency for two representative suspended SWNTs collected for different incident laser powers. From the lineshape of the tangential band present at  $\sim 1590 \text{ cm}^{-1}$  the spectra in panels (a) and (b) are assigned to a metallic and semiconducting nanotubes, respectively.

A second crucial implication from eq. (4.6) is that the observed linewidth should depend on temperature. *Conversely, if the true anharmonic linewidth was closer to  $10^{-4} \text{ cm}^{-1}$ , the temperature dependence would not be detectable.* To decide this critical issue we decided to analyze the temperature dependence of the linewidth of the suspended SWNTs. The most basic way to measure temperature dependence is by varying the laser power. The  $\omega_{\text{RBM}}$  values for several SWNTs as a function of the incident laser power for a metallic and semiconducting SWNT are shown in Fig. 4.16. An increase in the laser power resulted in both broadening of the peak and an increase in the peak intensity. This proves that the linewidth is indeed an increasing function of power, as expected for intrinsic anharmonic linewidths. Since the nanotubes are suspended over trenches it is very difficult to measure the exact temperature of a nanotube. However, a qualitative estimate of temperatures is possible by computing the ratio of the Stokes and anti-Stokes peaks in the Raman spectrum of the silicon substrate.

The Stokes and anti-Stokes lines correspond, respectively, to the absorption and emission of an optical phonon, the ratio of their intensities  $I_A$  and  $I_S$  are given by

$$\frac{I_A}{I_S} = \frac{(\omega + \omega_0)^4}{(\omega - \omega_0)^4} \frac{n}{n+1} \quad (4.7)$$

where  $n$  is the equilibrium occupation number of the  $q = 0$  (zone-center) phonon of frequency  $\omega$ . Eq. 4.7 is a direct consequence of Rayleigh's law, which states that the intensity of scattered light is proportional to  $k^4$  (or  $\omega^4$ ) [87]. Since

$$n = \left[ \exp\left(\frac{\hbar\omega_0}{k_b T}\right) - 1 \right]^{-1} \quad (4.8)$$

the ratio of the Stokes and anti-Stokes intensity simplifies to

$$\frac{I_A}{I_S} = \frac{(\omega + \omega_0)^4}{(\omega - \omega_0)^4} \exp\left(-\frac{\hbar\omega_0}{k_b T}\right) \quad (4.9)$$

Thus knowing the intensities of the Stokes and anti-Stokes peaks along with the peak frequency, one can estimate the temperature of the silicon substrate. However, this approach does not work with the Stokes and anti-Stokes spectra for suspended SWNTs since the resonance conditions are different in the case of Stokes and anti-Stokes Raman scattering [88].

Since it is difficult to determine the temperature of the nanotube, we chose to monitor the linewidth of the suspended nanotubes as a function of the incident laser power. We want to compute the linewidth as a function of the power. Assuming that

$$\frac{d\Gamma}{dP} = \frac{d\Gamma}{dT} \frac{dT}{dP} \quad (4.10)$$

The derivative of the linewidth with respect to  $T$  is approximately  $\Gamma$  over  $T$  in the high temperature down-conversion limit (regardless of whether there is Klemens decay or not). The power absorbed per unit length ( $x$ ) on the nanotube of diameter  $d_t$  for TEM<sub>00</sub> illumination by the laser is given by [64]

$$P(x) = \beta_0 \frac{\ln 2 d_t P_0}{\pi r_0^2} e^{-\frac{\ln 2 x^2}{r_0^2}} \quad (4.11)$$

where  $\beta_0 = 0.38$  (explained below),  $r_0$  is the nanotube radius and  $P_0$  is the total incident power. In our experiments, the incident power was kept at  $\sim 1$  mW. This results in the temperature as a function of power:

$$T = T_0 + kP, \quad (4.12)$$

where  $k$  is a constant given by [89]

$$k = \frac{\beta_0}{2b\kappa\pi^{3/2}} \int_{\sqrt{\ln 2x}/r_0}^{\sqrt{\ln 2L}/2r_0} \text{erf}(v) dv \quad (4.13)$$

where  $L$  is the length of the suspended portion of the nanotube and  $b = 0.34$  nm is the tube wall thickness. The above relation was obtained by solving the second order differential joule heat conduction equation [89]. The coefficient  $\beta$  is the fraction of light energy incident on the nanotube that is converted to thermal energy. The above equation can be combined with the heat transport model of Pop *et al.* [64], adapted to the case of illumination with a laser beam of total power  $P$ . Assuming that the maximum of the laser ( $\text{TEM}_{00}$ ) power profile with FWHM  $2r_0$  lies at the center of the suspended tube, and setting the nanotube thermal conductivity  $\kappa$  as  $3600 \text{ W m}^{-1} \text{ K}^{-1}$ , we get

$$\frac{d\Gamma}{dP} = \frac{\Gamma}{T} k = \frac{k\Gamma}{T_0 + kP} \quad (4.14)$$

or

$$\frac{d\Gamma}{\Gamma} = \frac{k dP}{T_0 + kP} \quad (4.15)$$

Integrating the above equation leads to

$$\Gamma(P) = \Gamma(P_0) \frac{T_0 + kP}{T_0 + kP_0} \quad (4.16)$$

Here  $T_0$  is the boundary value temperature at the points  $(-L/2, L/2)$ , where the tube contacts the substrate,  $P_0$  is the total incident power on the nanotube power. Thus

if we normalize to  $\Gamma(P_0)$ , all linewidths versus power should fall on the same curve for the same nanotube length. In this study, all linewidths were normalized to a laser power of 1 mW, and  $T_0$  was taken as the temperature of the substrate which was calculated using eq. (4.9).

The value of  $\beta_0$  was taken as 0.38, which results from assuming that the reflectivity of the nanotubes is roughly the same as that of graphite, and that the absorbance is as measured by Islam *et al.* [90], but corrected by a factor (300/16) to account for the fact that the results of Ref. [70] correspond to an ensemble of nanotubes. The observed optical transition width for SWNT bundles is  $\sim 300$  meV, whereas the corresponding width for an individual SWNT (as measured by resonance Raman scattering) is closer to 16 meV [91]. Recent near-field scanning optical microscopy results suggest  $\beta_0 = 0.58$ , close to our selected value [92]. The above calculation assumes that all the absorbed light is converted to heat, which should be a good approximation for metals and less so for semiconducting tubes with short radiation lifetimes. However, given the large uncertainties in the computation of  $\beta_0$  no distinction is made between semiconducting and metallic SWNTs. Figure 4.18 shows the measured linewidths versus laser power as a function of nanotube length. The dotted lines correspond to eq. 4.16 for SWNT suspended lengths of  $L = 2\text{-}5\ \mu\text{m}$ . As can be seen in the figure, most of the FWHM values agree well with the fitted curves corresponding to SWNT lengths ranging between 2-5  $\mu\text{m}$  over the trenches. The good agreement between the observed and calculated power dependences shown in Fig. 4.17 strongly suggests that the measured Raman linewidths represent the intrinsic anharmonic

broadening for the RBM. In addition, the length dependence of the RBM linewidth also matches the boundary condition that the temperature at the ends of a nanotube is equal to the temperature of the silicon substrate. Hence the heat from the laser spot that is focused at the center of the suspended portion of a SWNT takes longer to dissipate to the ends for a longer nanotube, thereby causing greater broadening of the RBM peak.

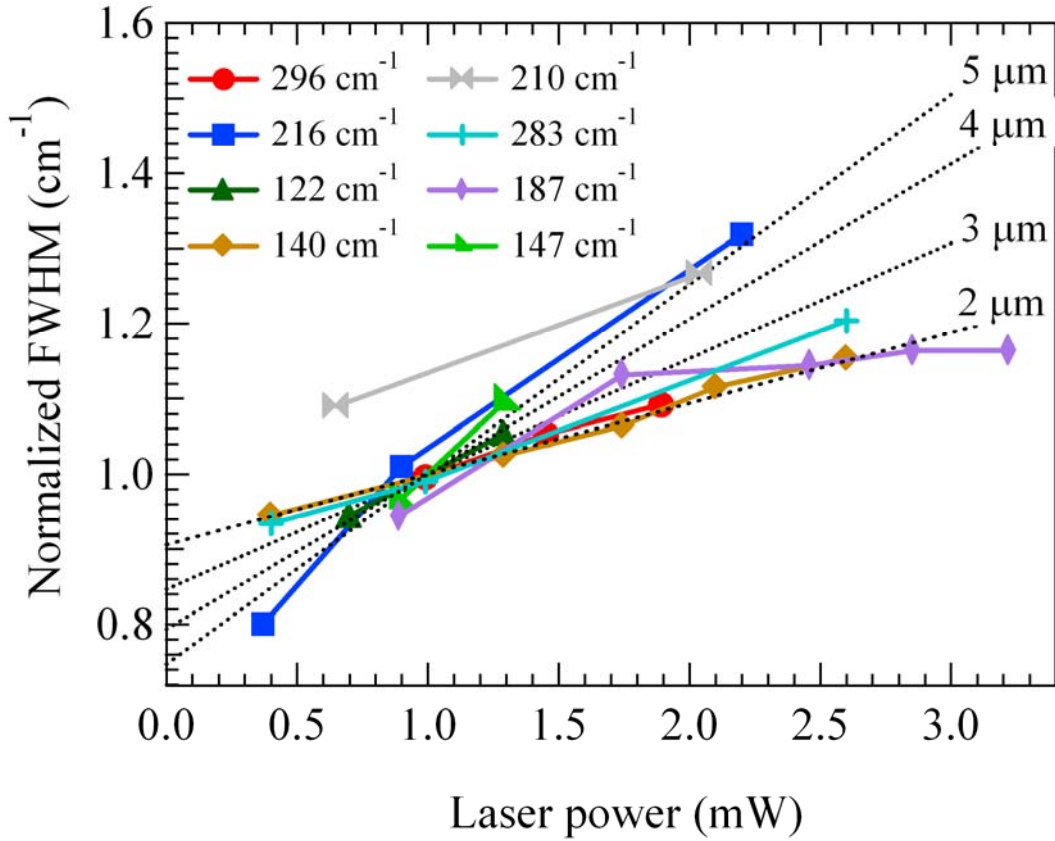


Figure 4.17: Normalized linewidth versus incident total laser power  $P$  (The normalized linewidth is defined as the Lorentzian FWHM at  $P$  divided by the FWHM at  $P_0 = 1\text{mW}$ ). The lines correspond to fits with eq. (4.16), in which the only adjustable parameter is the suspended length  $L$ .

The fact that smallest measurable room temperature Raman linewidths are on the order of  $1 \text{ cm}^{-1}$  (5.3 ps) calls for an explanation of the puzzling observation of mode lifetimes of  $\sim 10 \text{ ns}$  in the tunneling experiments performed by *et al.* [11]. The key to understanding this discrepancy lies in the one-dimensional nature of the phonon dispersion curves in carbon nanotubes (see Fig. 4.15). The standard perturbative approach for the analysis of Raman linewidths assumes that the secondary phonons, *i.e.*, the products of the Raman phonon decay, are in thermal equilibrium. This is justified in three dimensional crystals because these phonons occupy a significant reciprocal space volume, [53] so that deviations from equilibrium for each individual mode are negligible. This condition is not met in suspended SWNTs, where the phase space for decay products is reduced to a few discrete points.

In order to explain the discrepancy between the Raman and tunneling results, we have run numerical simulations of phonon decay that take into account the presence of non-equilibrium secondary phonons. In the simulation, the Raman process creates an excess population  $\delta n_0$  of primary phonons of frequency  $\omega_0$  (in this case  $\omega_0 = \omega_{\text{RBM}}$ ) which decays into pairs of phonons of frequency  $\omega_1 = \omega_0/2$ . (The assumption of equal frequency for the two secondary phonons is not critical but simplifies the math). This decay process creates an out-of-equilibrium population  $\delta n_1$  of secondary phonons, which further decays into pairs of tertiary phonons of frequency  $\omega_2 = \omega_1/2$ . The tertiary phonons are assumed to be in thermal equilibrium. The transition rates for the decay of primary phonons to



secondary and tertiary phonons can be derived using Fermi's golden rule, which can be stated as [93]

$$w_{i \rightarrow n} = \frac{2\pi}{\hbar} \left| \bar{V}_{ni} \right|^2 \delta(E_n - E_i), \quad (4.17)$$

where  $w$  is the transition rate between a state  $i$  to state  $n$ , and  $V_{ni}$  is the potential

Applying eq. 4.17 to the third-order lattice anharmonic Hamiltonian, we obtain the set of coupled equations

$$\begin{aligned} \frac{d(\delta n_0)}{dt} &= -\frac{1}{\tau_{01}} (1 + 2n_1) \delta n_0 + \frac{2}{\tau_{01}} (n_1 - n_0) \delta n_1 \\ \frac{d(\delta n_1)}{dt} &= \frac{1}{p\tau_{01}} (1 + 2n_1) \delta n_0 - \left[ \frac{1}{\tau_{12}} (1 + 2n_2) + \frac{1}{p\tau_{01}} (n_1 - n_0) \right] \delta n_1 \end{aligned}, \quad (4.18)$$

where terms that are non-linear in  $\delta n_0$ ,  $\delta n_1$  have been neglected [94]. Here  $\tau_{01}$  is the decay rate for primary into secondary phonons and  $\tau_{12}$  is the decay rate for secondary into tertiary phonons. Such a model was applied by Jursenas *et al.* [94] to study phonon decay processes in highly photoexcited CdS. The parameter  $p$  counts the number of pairs of secondary phonons that satisfy the energy and crystal momentum conservation rules. If we consider a  $\mathbf{k} = 0$  phonon in a three-dimensional crystal decaying into two equal-frequency acoustic phonons with

linear dispersion, the possible wave vectors of the decay phonons form a spherical shell in  $\mathbf{k}$ -space. By contrast, for the same conditions in a one-dimensional crystal the wavevectors of the decay products are reduced to a single  $(\mathbf{k}, -\mathbf{k})$  pair. Thus in three dimensional solids we usually have  $p \gg 1$ , whereas for one-dimensional systems  $p \sim 1$ . If we set  $\delta n_1 = 0$ , eq. (4.18) is equivalent to eq. (4.6), with  $2\Gamma = 1/\tau_{01}$ . Figure 4.19 (a) shows calculations of  $\delta n_0$  for  $\tau_{12} = 500 \tau_{01}$ , a reasonable choice if the secondary phonons are acoustic phonons with lifetimes much longer than the optical phonon lifetime [95]. For the solid line, the initial condition is  $\delta n_0 = 0.1$ ,  $\delta n_1 = 0$  and  $p = 2$ . We notice that there is a fast initial decay, determined by  $\tau_{01}$ , followed by a much slower decay that is dominated by  $\tau_{12}$ . This is caused by the long-lived secondary phonons recombining and generating new primary phonons. The reason why the lifetime of the secondary decay products comes to determine the lifetime of the primary phonons is the decay bottleneck induced by the low value chosen for the parameter  $p$ . If we increase this value, as done for the dotted line in Fig. 4.19(a), the effect of the secondary phonons vanishes and the decay is completely determined by the shorter lifetime  $\tau_{01}$  of the primary phonons.

The scenario just depicted offers a natural interpretation for the discrepancy between the Raman and tunneling measurements. In Fig. 4.18(b) we show the calculated Raman lineshape corresponding to the solid-line decay pattern in Fig. 4.18(a). It has a very sharp central maximum, corresponding to the long lifetime  $\tau_{12}$ , and much broader tails corresponding to the short lifetime  $\tau_{01}$ . However, the *observed* Raman spectrum is a convolution of the intrinsic lineshape

with the instrument's resolution function, and this is depicted in Fig 4.18(c). Here the central spike has essentially vanished, and if we fit the convoluted lineshape with a standard Voigt profile, we obtain for the Lorentzian FWHM  $2\Gamma = 0.98/\tau_{01}$ . In other words a Raman spectrum under these conditions would measure the short lifetime  $\tau_{01}$ , whereas a time-domain study, such as the tunneling experiments performed by *et al.* [11], would see the much longer lifetime  $\tau_{12}$ . The apparent discrepancy between the two types of measurements is further enhanced if we consider the fact that in a tunneling experiment—as opposed to a Raman process—there is no strong selection rule restricting the phonons that can be activated. Therefore, if the tunneling event generates primary *and* secondary phonons, the presence of these secondary phonons may contribute to a further reduction of the decay of the primary phonon. This effect is simulated by the dash-dotted line in Fig. 4.19(a), which was computed with initial conditions  $\delta n_0 = 0.1$ ,  $\delta n_1 = 0.5$ .

In summary, we have presented strong evidence for the measurement of intrinsic Raman linewidths in suspended carbon nanotubes, and we have identified a phonon decay bottleneck as an important decay characteristic of one-dimensional solids that explains the large apparent discrepancy between lifetimes measured in the frequency and time domains.

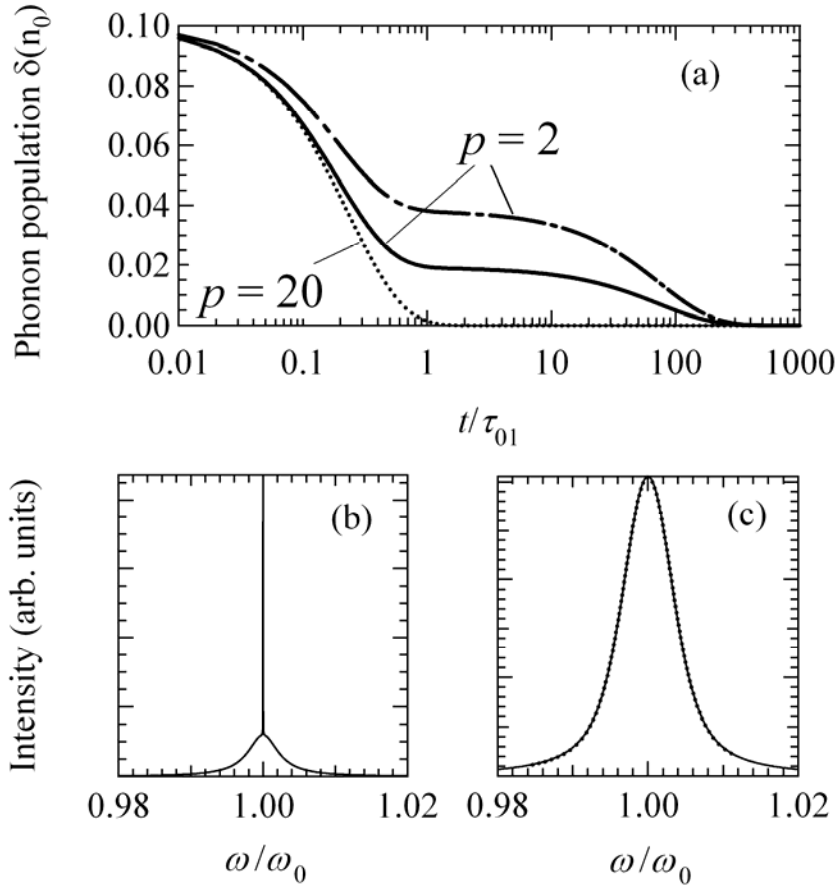


Figure 4.18:(a) *Solid line*: Raman phonon population decay under conditions that create a decay bottleneck ( $p \sim 2$ ); *Dotted line*: Raman phonon population decay under conditions in which the decay bottleneck is negligible ( $p \gg 1$ ). *Dashed-dotted line*: Raman phonon population decay when the secondary phonons are also created by the external perturbation like tunneling (b) Predicted Raman spectrum corresponding to the solid line in panel (a).; (c) *Solid line*: Modeled observed Raman spectrum obtained from convoluting the spectrum in panel (b) with a Gaussian function, *Dotted line*: Fit of the solid line using a Voigt profile.

## CHAPTER FIVE SUMMARY

### Conclusions

The work described in this dissertation focused on two quasi-1D systems which provide evidence for the effects of anharmonicity through Raman scattering measurements. In the first system, we observed upshifts of peaks in the Raman spectra for  $\beta$ -Ga<sub>2</sub>O<sub>3</sub> nanowires grown along the [110] growth direction compared to the Raman spectrum for bulk  $\beta$ -Ga<sub>2</sub>O<sub>3</sub>. A comparison with other studies in the literature showed that downshifts in the Raman spectra for  $\beta$ -Ga<sub>2</sub>O<sub>3</sub> nanowires (having different growth directions) compared to bulk  $\beta$ -Ga<sub>2</sub>O<sub>3</sub> have also been observed. Such frequency shifts between the Raman spectra of a nanomaterial compared to the corresponding bulk Raman spectrum have been attributed to phonon confinement. However, due to the relatively large diameters of the  $\beta$ -Ga<sub>2</sub>O<sub>3</sub> nanowires ( $\sim 30$  nm) probed in this study we dismissed phonon confinement as the likely source of the Raman shifts. Instead, we attributed these Raman shifts to growth direction-induced lattice strains in the nanowires and discussed a LDA model to support our hypothesis. Due to the complexity of the Ga<sub>2</sub>O<sub>3</sub> system we did not model the vibrational frequencies in the strained nanowires using an anharmonic potential; instead a quasi-harmonic LDA model was sufficient to confirm the experimentally observed Raman shifts in our nanowires. However, such a model may not be sufficient to understand other

aspects such as the temperature dependence of the Raman peaks of  $\beta$ -Ga<sub>2</sub>O<sub>3</sub> nanowires, and a complete first-principles anharmonic description would be required. The second system studied was the single-walled carbon nanotube. Our study was motivated by a tunneling study reported by *et al.* [11] in which they electrically excited radial breathing mode phonons in a suspended SWNT. According to their study the lifetime of the radial breathing mode phonon is in the nanosecond regime. In contrast, optical techniques such as Raman spectroscopy have shown the RBM lifetime to be in the picosecond regime. We investigated this interesting puzzle via high-resolution micro-Raman experiments on suspended SWNTs and observed RBM linewidths lower than previously reported in the literature. However, our study also showed the RBM lifetime to be in the picosecond regime, and we sought to explain this discrepancy with LeRoy's measurements [11] by invoking an anharmonic model for phonon decay in carbon nanotubes. Compared to the  $\beta$ -Ga<sub>2</sub>O<sub>3</sub> system, a SWNT is an all-carbon system and hence it is relatively simpler to model. We were able to apply anharmonicity theory to phonon decay in carbon nanotubes and discovered a phonon bottleneck mechanism which explains the discrepancy in RBM lifetimes seen between the Raman spectroscopy and tunneling studies. Understanding the nature of phonon decay and lifetimes in 1D systems such as carbon nanotubes could have a big impact on their thermal conductance properties.

### Future Work

Strains in nanowires can be determined by a variety of methods. In this dissertation we reported differences between the Raman spectra of  $\beta$ -Ga<sub>2</sub>O<sub>3</sub> nanowires and bulk  $\beta$ -Ga<sub>2</sub>O<sub>3</sub>, and presented a theoretical model as evidence for inherent growth direction-induced strains in  $\beta$ -Ga<sub>2</sub>O<sub>3</sub> nanowires. Another method to study strains could be to induce strains in un-strained  $\beta$ -Ga<sub>2</sub>O<sub>3</sub> nanowires (whose Raman spectra are similar to that of bulk  $\beta$ -Ga<sub>2</sub>O<sub>3</sub>) externally by using a diamond anvil cell and then study the high-pressure Raman spectra of the nanowires. Such studies have been performed on other materials such as carbon nanotubes [96] and provide useful information on their deformation behavior. In addition to the spectroscopy techniques discussed in this dissertation, fluorescence spectroscopy can also be used to probe strains in nanomaterials. The electronic structure, and hence the bandgap of a material is affected by strain, and shifts in the emission peak caused by the change in the bandgap in the strained nanowires can be directly correlated to the amount of strain induced in the material. In addition, electron diffraction analysis can also be performed on strained and unstrained nanowires to confirm the changes in the lattice parameters due to strains along certain axes of the unit cell.

Suspended SWNTs provide us with an excellent platform for a variety of Raman studies that probe the intrinsic vibrational properties of individual nanotubes. As was discussed in chapter 4, the linewidth of the RBM is significantly different for a suspended SWNT and an isolated nanotube on a substrate. We can perform such an experiment in our lab by focusing on a long

SWNT where a part of the nanotube is on the substrate and a part of it is suspended. By accurately measuring the change in the RBM linewidth between the trench and the suspended part of the nanotube we could estimate the magnitude of the Van der Waals force between the SWNT and the substrate. In addition, it would be interesting to study the linewidths of suspended and isolated SWNTs that are heated via other techniques such as an electrically heated cell. Such a temperature cell provides a controlled environment so in which trace amounts of adsorbed gases on the SWNT walls can be detected via changes in the RBM linewidth.



## APPENDIX

### Glossary of acronyms used in this dissertation

BWF – Breit-Wigner-Fano

CCD – Charge-coupled device

CVD- Chemical vapor deposition

DFT – Density functional theory

DOS – Density of states

DTGS – Deuterated triglycine sulfate

FTIR – Fourier transform infrared

FWHM – Full-width half maximum

GGA – Generalized gradient approximation

HRTEM – High resolution transmission electron microscope

LA – Longitudinal acoustic

LDA – Linear density approximation

NEMS – Nanoelectromechanical

RBM – Radial breathing mode

SAD – Selected area diffraction

SEM – Scanning electron microscope

STM – Scanning tunneling microscope

SWNT – Single-walled carbon nanotube

USPP – Ultra-soft pseudopotentials

TA – Transverse acoustic

VASP – Vienna ab-initio simulation package

vHS – Van Hove singularities

## REFERENCES

- [1] J. A. Reissland, *The physics of phonons* (Wiley, London, New York,, 1973), pp. xi.
- [2] C. Kittel, *Introduction to solid state physics* (Wiley, New York, 1976), pp. xiv.
- [3] N. S. Shiren, Phys. Rev. Lett. **11**, 3 (1963).
- [4] A. Q. R. Baron *et al.*, Physical Review B **75** (2007).
- [5] P. G. Klemens, Phys. Rev. **148**, 845 (1966).
- [6] T. May, W. Muller, and D. Strauch, Physical Review B **57**, 5758 (1998).
- [7] M. J. Scepanovic *et al.*, Appl. Phys. A **86**, 365 (2007).
- [8] P. S. Peercy, Phys. Rev. B **8**, 6018 (1973).
- [9] Y. H. Gao *et al.*, App. Phys. Lett. **81**, 2267 (2002).
- [10] Y. C. Choi *et al.*, Adv. Mat. **12**, 746 (2000).
- [11] B. J. Leroy *et al.*, Nature **432**, 371 (2004).
- [12] R. Pfeiffer *et al.*, Phys. Rev. Lett. **90**, 225501 (2003).
- [13] C. V. Raman, and K. S. Krishnan, Nature **121**, 711 (1928).
- [14] K. W. F. Kohlrausch, *Der Smekal-Raman Effekt* (Springer, Berlin, 1931).
- [15] D. A. Long, *Raman Spectroscopy* (McGraw-Hill Inc., Great Britain, 1977).
- [16] M. Ogita *et al.*, Appl. Surf. Sci. **175-176**, 721 (2001).
- [17] M. Fleischer *et al.*, Sens. Act. B **69**, 205 (2000).
- [18] A. L. Petre *et al.*, Thermochim. Acta **379**, 177 (2001).
- [19] T. Miyata, T. Nakatani, and T. Minami, J. Lumin. **87-89**, 1183 (2000).
- [20] G. Gundiah, A. Govindaraj, and C. N. R. Rao, Chem. Phys. Lett. **351**, 189 (2002).

- [21] C. H. Liang *et al.*, Appl. Phys. Lett. **78**, 3202 (2001).
- [22] Z. R. Dai, Z. W. Pan, and Z. L. Wang, J. Phys. Chem. B **106**, 902 (2002).
- [23] H. Z. Zhang *et al.*, Sol. St. Comm. **109**, 677 (1999).
- [24] W. Q. Han *et al.*, Sol. St. Comm. **115**, 527 (2000).
- [25] S. Sharma, and M. K. Sunkara, J. Am. Chem. Soc. **124**, 12288 (2002).
- [26] R. Rao *et al.*, Journal of Electronic Materials **35**, 941 (2006).
- [27] R. Rao *et al.*, Journal of Applied Physics **98** (2005).
- [28] X. Duan, and C. M. Lieber, Adv. Mater. **12**, 298 (2000).
- [29] S. Sharma, and M. K. Sunkara, Nanotechnology **15**, 130 (2004).
- [30] J. A. Creighton, and R. Whitnall, Chem. Phys. Lett. **326**, 311 (2000).
- [31] D. Dohy, G. Lucazeau, and A. Revcolevschi, J. Sol. St. Chem. **45**, 180 (1982).
- [32] Y. Tomm *et al.*, Sol. Ener. Mater. Sol Cells **66**, 369 (2001).
- [33] S. Geller, J. Chem. Phys. **33**, 676 (1960).
- [34] A. M. Rao *et al.*, Science **275**, 187 (1997).
- [35] K. Adu *et al.*, Appl. Phys. A **85**, 287 (2006).
- [36] A. G. Milekhin *et al.*, Nanotechnology **13**, 55 (2002).
- [37] K. McGuire *et al.*, J. Nanosci. Nanotech. **2**, 1 (2002).
- [38] F. Fukumi, and S. Sakka, Phys. Chem. Glasses **29**, 1 (1988).
- [39] S.-L. Zhang *et al.*, Sol. St. Comm. **111**, 647 (1999).
- [40] L. Dai *et al.*, J. App. Phys. **92**, 1062 (2002).
- [41] N. Colthup, L. H. Daly, and S. E. Wiberley, *Introduction to Infrared and Raman Spectroscopy* (Academic Press Inc., New York, 1975).
- [42] H. Richter, Z. P. Wang, and L. Ley, Sol. St. Comm. **39**, 625 (1981).
- [43] I. H. Campbell, and P. M. Fauchet, Sol. St. Comm. **58**, 739 (1986).
- [44] R. M. Martin, Phys. Rev. Lett. **21**, 536 (1968).
- [45] J. Maultzsch *et al.*, Phys. Rev. Lett. **92**, 075501 (2004).

- [46] A. C. Ferrari *et al.*, Phys. Rev. Lett. **97**, 187401 (2006).
- [47] D. Graf *et al.*, Cond. Mater. **21**, 1 (2006).
- [48] R. G. Parr, and W. Yang, *Density-Functional Theory of Atoms and Molecules* (Oxford University Press, New York, 1988).
- [49] J. J. Dong, and O. Sankey, *SiC power materials: Devices and Applications* (Springer-Verlag, Berlin, 2004).
- [50] D. Vanderbilt, Phys. Rev. B **41**, 7892 (1990).
- [51] H. J. Monkhorst, and J. D. Pack, Phys. Rev. B **13**, 5188 (1997).
- [52] H. W. Seo *et al.*, J. Chem. Phys. **116**, 9492 (2003).
- [53] A. Debernadi, S. Baroni, and E. Molinari, Phys. Rev. Lett. **75**, 1819 (1995).
- [54] R. Saito, G. Dresselhaus, and M. S. Dresselhaus, *Physical Properties of Carbon Nanotubes* (Imperial College Press, London, 1998).
- [55] A. Jorio *et al.*, Phys. Rev. Lett. **86**, 1118 (2001).
- [56] A. Jorio *et al.*, New Journal of Physics **5** (2003).
- [57] M. S. Dresselhaus *et al.*, Phys. Rep. **409**, 47 (2005).
- [58] M. S. Dresselhaus, and P. C. Eklund, Adv. Phys. **49**, 705 (2000).
- [59] S. Reich, in *Physics* (Technical University of Berlin, Berlin, 2001).
- [60] M. S. Dresselhaus *et al.*, J. Nanosci. Nanotech. **3**, 19 (2003).
- [61] M. S. Dresselhaus, and G. Dresselhaus, Adv. Phys. **30**, 139 (1981).
- [62] M. A. Pimenta *et al.*, Phys. Rev. B **58**, R16016 (1998).
- [63] A. M. Rao *et al.*, Nature **388**, 257 (1997).
- [64] E. Pop *et al.*, Phys. Rev. Lett. **95**, 155505 (2005).
- [65] P. G. Klemens, *Solid State Physics* (Academic Press Inc., New York, 1958), Vol. 7.
- [66] A. Debernardi, S. Baroni, and E. Molinari, Phys. Rev. Lett. **75**, 1819 (1995).
- [67] M. N. Iliev *et al.*, Chem. Phys. Lett. **316**, 217 (2000).
- [68] A. Jorio *et al.*, Phys. Rev. B **66**, 115411 (2002).

- [69] S. Huang *et al.*, Nano Lett. **4**, 1025 (2004).
- [70] M. J. O'connel *et al.*, Science **297**, 593 (2002).
- [71] R. Martel *et al.*, Appl. Phys. Lett. **73**, 2447 (1998).
- [72] P. G. Collins *et al.*, Science **287**, 1801 (2000).
- [73] A. Cassell *et al.*, J. Am. Ceram. Soc. **121**, 7975 (1999).
- [74] Y. J. Jung *et al.*, J. Phys. Chem. B **107**, 6859 (2003).
- [75] J. Lefebvre, P. Finnie, and Y. Homma, Phys. Rev. B **70**, 045419 (2004).
- [76] N. Franklin *et al.*, Appl. Phys. Lett. **81**, 913 (2002).
- [77] H. Ustunel, D. Roundy, and T. A. Arias, Nano Lett. **5**, 523 (2005).
- [78] Y. Kobayashi *et al.*, Phys. E **24**, 26 (2004).
- [79] H. Son *et al.*, Appl. Phys. Lett. **85**, 4744 (2004).
- [80] Y. S. L. e. al., Cond. Mater., 0606396 (2006).
- [81] S. Huang, X. Cai, and J. Liu, J. Am. Chem. Soc. **125**, 5636 (2003).
- [82] J. H. Kielkopf, J. Opt. Soc. Am. **63**, 987 (1973).
- [83] J. Serrano *et al.*, Phys. Rev. Lett. **90**, 055510 (2003).
- [84] S. M. Bose, S. Gayen, and S. N. Behera, Phys. Rev. B **72**, 153402 (2005).
- [85] H. Kataura *et al.*, Synth. Met. **103**, 2555 (1999).
- [86] R. F. Wallis, and M. Balkanski, *Many body aspects of solid state spectroscopy* (North Holland, Amsterdam, 1986).
- [87] J. D. Jackson, (Wiley, 1998), p. 457.
- [88] A. G. S. Filho *et al.*, Phys. Rev. B **69**, 115428 (2004).
- [89] E. Pop *et al.*, accepted, J. Appl. Phys. (2007).
- [90] M. F. Islam *et al.*, Phys. Rev. Lett. **93**, 037404 (2004).
- [91] A. Jorio *et al.*, Phys. Rev. B **63**, 245416 (2001).
- [92] W. Zhang *et al.*, Scanning **26**, I21 (2004).

- [93] J. J. Sakurai, in *Modern quantum mechanics*, edited by S. F. Tuan (Pearson education, 1994).
- [94] S. Jursenas, A. Zukauskas, and R. Baltramiejunas, J. Phys. Cond. Matter **4**, 9987 (1992).
- [95] A. Berke, A. P. Mayer, and R. K. Wehner, J. Phys. C: Sol. St. Phys. **21**, 2305 (1988).
- [96] U. Venkateswaran *et al.*, Phys. Stat. Sol. **223**, 225 (2001).